ornl

ORNL/TM-1999/95

OAK RIDGE
NATIONAL
LABORATORY

LOCKHEED MARTIN

Heavy Vehicle Propulsion System Materials Program Semiannual Progress Report for October 1998 Through March 1999

Prepared for
U.S. Department of Energy
Assistant Secretary for
Energy Efficiency and Renewable Energy
Office of Transportation Technologies

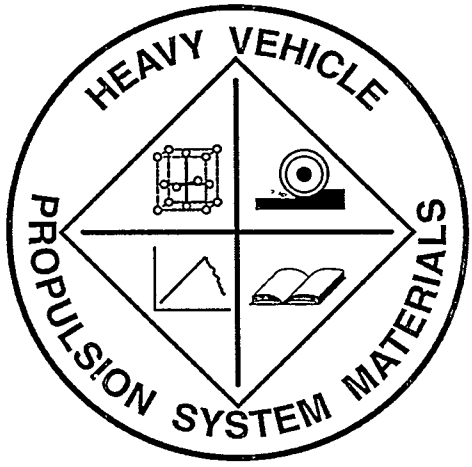

MANAGED AND OPERATED BY
LOCKHEED MARTIN ENERGY RESEARCH CORPORATION
FOR THE UNITED STATES
DEPARTMENT OF ENERGY

ORNL-27 (3-96)

DISCLAIMER

Portions of this document may be illegible in electronic image products. Images are produced from the best available original document.

ORNL/TM-1999/95

Metals and Ceramics Division

HEAVY VEHICLE PROPULSION SYSTEM MATERIALS PROGRAM SEMIANNUAL PROGRESS REPORT FOR OCTOBER 1998 THROUGH MARCH 1999

D. R. Johnson
Program Manager

Date Published: June 1999

Prepared for
U.S. Department of Energy
Assistant Secretary for Energy Efficiency and Renewable Energy
Office of Transportation Technologies
EE 04 02 000

Prepared by the
OAK RIDGE NATIONAL LABORATORY
Oak Ridge, Tennessee 37831-6285
managed by
LOCKHEED MARTIN ENERGY RESEARCH CORP.
for the
U.S. DEPARTMENT OF ENERGY
under Contract DE-AC05-96OR22464

REPORTS PREVIOUSLY ISSUED

ORNL/TM-9325	Period March 1983-September 1983
ORNL/TM-9466	Period October 1983-March 1984
ORNL/TM-9497	Period April 1984-September 1984
ORNL/TM-9673	Period October 1984-March 1985
ORNL/IM-9947	Period April 1985-September 1985
ORNL/TM-10079	Period October 1985-March 1986
ORNL/TM-10308	Period April 1986-September 1986
ORNL/TM-10469	Period October 1986-March 1987
ORNL/TM-10705	Period April 1987-September 1987
ORNL/TM-10838	Period October 1987-March 1988
ORNL/TM-11116	Period April 1988-September 1988
ORNL/TM-11239	Period October 1988-March 1989
ORNL/TM-11489	Period April 1989-September 1989
ORNL/TM-11586	Period October 1989-March 1990
ORNL/TM-11719	Period April 1990-September 1990
ORNL/TM-11859	Period October 1990-March 1991
ORNL/TM-11984	Period April 1991-September 1991
ORNL/TM-12133	Period October 1991-March 1992
ORNL/TM-12363	Period April 1992-September 1992
ORNL/TM-12428	Period October 1992-March 1993
ORNL/TM-12674	Period April 1993-September 1993
ORNL/TM-12778	Period October 1993-March 1994
ORNL/TM-12924	Period April 1994-September 1994
ORNL/TM-13046	Period October 1994-March 1995
ORNL/TM-13219	Period April 1995-September 1995
ORNL/TM-13262	Period October 1995-March 1996
ORNL/TM-13395	Period April 1996-September 1996
ORNL/TM-13467	Period October 1996-March 1997
ORNL/TM-13562	Period April 1997-September 1997
ORNL/TM-13648	Period October 1997-March 1998
ORNL/TM-13735	Period April 1998-September 1998

Research sponsored by the U.S. Department of Energy, Assistant Secretary for Energy Efficiency and Renewable Energy, Office of Transportation Technologies, as part of the Heavy Vehicle Propulsion System Materials Program, under contract DE-AC05-96OR22464 with Lockheed Martin Energy Research Corporation.

CONTENTS

HEAVY VEHICLE PROPULSION SYSTEM MATERIALS PROGRAM
SEMIANNUAL PROGRESS REPORT
FOR OCTOBER 1998 THROUGH MARCH 1999

SUMMARY AND INTRODUCTION

The purpose of the Heavy Vehicle Propulsion System Materials Program is the development of materials: ceramics, intermetallics, metal alloys, and metal and ceramic coatings, to support the dieselization of class 1-3 trucks to realize a 35% fuel-economy improvement over current gasoline-fueled trucks and to support commercialization of fuel-flexible LE-55 low-emissions, high-efficiency diesel engines for class 7-8 trucks.

The Office of Transportation Technologies, Office of Heavy Vehicle Technologies (OTT OHVT) has an active program to develop the technology for advanced LE-55 diesel engines with 55% efficiency and low emissions levels of 2.0 g/bhp-h NOx and 0.05 g/bhp-h particulates. The goal is also for the LE-55 engine to run on natural gas with efficiency approaching that of diesel fuel. The LE-55 program is being completed in FY 1997 and, after approximately 10 years of effort, has largely met the program goals of 55% efficiency and low emissions. However, the commercialization of the LE-55 technology requires more durable materials than those that have been used to demonstrate the goals. Heavy Vehicle Propulsion System Materials will, in concert with the heavy duty diesel engine companies, develop the durable materials required to commercialize the LE-55 technologies.

OTT OHVT also recognizes a significant opportunity for reduction in petroleum consumption by dieselization of pickup trucks, vans, and sport utility vehicles. Application of the diesel engine to class 1, 2, and 3 trucks is expected to yield a 35% increase in fuel economy per vehicle. The foremost barrier to diesel use in this market is emission control. Once an engine is made certifiable, subsequent challenges will be in cost; noise, vibration, and harshness (NVH); and performance.

The design of advanced components for high-efficiency diesel engines has, in some cases, pushed the performance envelope for materials of construction past the point of reliable operation. Higher mechanical and tribological stresses and higher temperatures of advanced designs limit the engine designer; advanced materials allow the design of components that may operate reliably at higher stresses and temperatures, thus enabling more efficient engine designs. Advanced materials also offer the opportunity to improve the emissions, NVH, and performance of diesel engines for pickup trucks, vans, and sport utility vehicles.

The principal areas of research are:

Cost Effective High Performance Materials and Processing
Advanced Manufacturing Technology
Testing and Characterization
Materials and Testing Standards

COST EFFECTIVE HIGH PERFORMANCE MATERIALS AND PROCESSING

Cost-Effective Smart Materials for Diesel Engine Applications

J. O. Kiggans, Jr., T. N. Tiegs,
F. C. Montgomery, L. C. Maxey, and C. C. Davisson
Oak Ridge National Laboratory
Oak Ridge, TN 37831

Objective / Scope

There are two objectives for this project. The first is to evaluate the cost-effectiveness and maturity of various "Smart Materials Technologies," which are under consideration for diesel engine applications, such as fuel injection systems. The second is to develop "Smart Materials," to be incorporated into working actuators and sensors.

Poling of Lead Zirconate Titanate (PZT)

PZT-4 is a candidate material for high frequency actuator applications, due to its high Quality (Q) factor and high Curie temperature. In the previous bimonthly, we reported on the use of an alternative sintering configuration, designated the inverted crucible arrangement, which has given us better control of PZT sintering. The present report will discuss the development of methods used for poling of PZT-4 materials.

Experimental Procedures

Several types of PZT-4 test samples were used for the poling studies: 1,2) Sintered, die pressed and gelcast PZT-4 samples (25 mm diameter by 1.2 mm thick); 3) unpoled PZT-4 discs, which were purchased in the as-sintered condition from American Piezo Ceramics (APC), Inc.(15 mm by 1 mm thick); and 4) sintered, poled, electroded samples from American Piezo Ceramics, Inc. (25 mm by 0.5 to 1.5 mm thickness). The samples were then polished using a Struers RotoForce-4 sample head on a RotoPol-22 cabinet for 1 to 2 minute at 5 to 10 N pressure using Struers 1200 and then 4000 grit SiC paper with flowing water for lubrication. Polished samples were cleaned with acetone, and gold electrodes were applied to both sides of the polished discs using a Technics gold sputter coater.

Figure 1 shows the poling device used for the poling study. The poling device is a brass fixture which allows the loading of samples of different thickness between a stationary and a spring loaded electrode. Initial poling studies were conducted from several sources including published literature[1,2]. Poling experiments were conducted in a Lauda circulating oil bath at either 100°C or 120°C at 2,3, or 4 kV for times ranging from 10 to 60 minutes. Following poling, the d_{33} piezoelectric charge constant was measured using a Pennebaker Model 8000 Piezo d_{33} Tester, commonly referred to as a Berlincourt tester. The d_{33} constant (the mechanical strain of a materiel experienced per unit electric field applied) is a good indicator of poling effectiveness.

Results

Initial tests to determine poling conditions were performed using the unpoled discs purchased from APC. The first set of poling experiments was to determine a suitable poling temperature. Figure 2 show the results of this study comparing poling at 100 and 120°C with 2 kV/mm (kV of poling voltage per mm thickness of sample) poling voltage for 30, 60, or 90 minutes with the APC unpoled discs. The 120°C poling was more effective than 100°C poling at both 30 and 60 minutes. The d_{33} value increased slightly for poling at 100°C with small increases for the 60 and 90 minute times. However, the d_{33} for the 120°C poling did not increase for the longer 60 minute poling time.

The next poling test was to determine the most suitable poling voltage at the 120°C temperature. Tests were performed with poling at 2, 3, or 4 kV/mm. for either 30 or 60 minutes with the APC unpoled samples. Figure 3 is a graph summarizing the results. The d_{33} values indicate that 3 and 4 kV/mm were clearly more effective poling voltage for both 30 and 60 minute poling. On a few instances, there was a voltage breakdown at the edges of samples poled at 4 kV/mm, so the 3 kV/mm was chosen as the most appropriate poling voltage.

The next set of poling experiments were conducted to narrow the required poling times. The previous data in Figure 3 showed that there was no change in the d_{33} values for the 30 and 60 minute samples at 3 kV/mm, so shorter time periods for poling were tested. Figure 4 shows d_{33} values obtained for poling experiments with two different APC discs at 120°C at 3 kV/mm for 10 and 20 minutes. There are only small differences for the 10 and 20 minute poling times, so 10 minutes was chosen as a sufficient poling time.

The next poling tests were performed at optimized poling conditions with die pressed and gelcast materials that were fabricated at ORNL. Figure 5 shows d_{33} values for materials sintered at 1200 and 1275°C +/-10°C. The d_{33} measurements were made about 1 minute after poling, before the onset of aging of the PZT materials. The data clearly shows the increase in d_{33} with the higher sintering temperature. The gelcast materials had slightly higher d_{33} values.

The final data collected was aging data for the d_{33} values of APC material poled at Oak Ridge, APC material poled at APC, and for the die pressed and gelcast materials sintered and poled at Oak Ridge. Figure 6 shows the rapid aging that occurs in these PZT materials over the first 24 h after poling, with the logarithmic slow down of aging after 24 h. This is a well-known phenomena that occurs in all poled ferroelectric materials. This plot shows that the as received, sintered, unpoled APC materials had higher d_{33} values (after poling in-house) than the ORNL fabricated die pressed and gelcast materials. This indicates that maximum sintering conditions have not yet been found for the in house materials. An interesting piece of data not shown is that as received material, that was poled by APC Inc., had a d_{33} of 352 $x10^{-12}$ m/V. This compares very well with materials sintered and poled in-house.

A Comparison of PZT-4 Materials Prepared by Different Forming Methods

It is generally accepted that the reliability of PZT materials is strongly affected by the quality of the green PZT preforms. Studies were initiated to compare the properties of PZT materials prepared by die press, tape cast, and gelcast forming methods. In this report we compare the sintering characteristics of the preforms, and the electrical properties of the sintered PZT materials.

Experimental Procedures

A commercial PZT powder, APC 840 (APC Ceramics Inc.), also designated by the generic industrial designation PZT-4, was used in this study. This powder is manufactured as a spray dried powder with polyvinyl alcohol as a binder. Methods for preparation of die pressed and gelcast test discs were discussed in previous reports.

Tape cast materials were fabricated using a Mistler Co. TTC-1000 tape casting machine using basic procedures described in several publications.[3,4] The tape slurries consisted of 78.3 wt. % PZT-4, 7.5 wt. % xylene, 7.5 wt. % anhydrous. ethanol, 1.0 wt. % menhaden fish oil (Tape Cast Warehouse), 1.6 wt. % butyl benzyl phthalate (Tape Cast Warehouse), 1.6 wt. % polyethylene glycol 400, and 2.5 wt. % polyvinyl butyral (Butvar-98, Monsanto Chemical Co.). Tapes were cast onto a mylar film moving at 20 cm/min using a 7.6 cm wide doctor blade adjusted to a thickness of 0.88 mm. The thickness of the dried tapes was ~0.45 mm. Laminated tape cast samples were fabricated by uniaxial pressing 5 to 6 stacked, 25 mm diameter discs (which were cut from the cast tapes) in a 25.4 mm diameter die at 80°C under a pressure of 25 MPa for 5 min.

The green densities of test samples were measured prior to the binder burn-out process. A TGA-DTA analyses (TA Instruments) were performed to help design an acceptable heating schedule for each sample type. Samples were placed on tabular alumina powder in an alumina crucible, and binder burn-out conducted in a box furnace with flowing air. The die pressed and gelcast samples were heated at 1 °C/min to 300°C with a 1 h dwell, followed by a 1 °C/min to 550 - 600°C with a 2 h hold (total heating time of 13 h). Binder burn-out of tape cast was performed using a 25 h heating program involving multiple temperature ramps and dwells.
In preparation for sintering, PZT samples were placed in alumina setter crucibles, each of which was covered by a second alumina crucible. A thin powder bed of 90 wt. % $PbZrO_3$-10 wt % ZrO_2 powder was placed around the outer sealing surface of the top cover crucibles to provide atmosphere control. The sample packages were then heated in an alumina tube furnace in flowing air at 10°C/min to final temperatures of 1200°, 1275°, or 1300 °C+/-10°C, with a 3 h dwell at the sintering temperature, followed by cooling to room temperature at 10°C/min. Densities of sintered samples were measured by the Archimedes immersion method in absolute ethanol.

Samples were polished using a RotoPol grinding/polishing machine (Struers Inc.) for 30 sec. to 1 min. at 5 to 10 N pressure using 500, 1200, and then 4000 grit SiC paper, with water lubrication. Polished samples were cleaned with acetone, and gold electrodes were applied to both sides of the polished discs using a Technics gold sputter coater. Samples were poled at 120°C at 3 kV for 10 min in a Lauda circulating oil bath. The piezoelectric charge constant, d_{33}, was measured 24 h after poling using a Pennebaker Model 8000 Piezo d_{33} Tester (APC Inc.), commonly referred to as a Berlincourt tester. In addition, the relative dielectric constant, K^T_{33}, at 1000 Hz, and the electromechanical coupling coefficient, k_p were measured using a Hewlett Packard 4194a Impedance/Gain Phase Analyzer with a HP 16034E test fixture.

After electrical measurements, some poled PZT-4 samples were ground using a RotoPol grinding/polishing machine (Struers Inc.) with 500, 1200, and 4000 grit SiC paper,. The samples were polished with 3 micron diamond and then 0.05 micron silica solution (Struers OP-S Suspension). The polished samples were etched for 15 min. in a 18.5 wt. % hydrochloric acid solution, and coated with a thin layer of gold for SEM examination of the sintered microstructures.

Results

Table 1 shows the green densities and binder burn-out weight losses for the gelcast, tape cast, and die pressed PZT preforms. The green densities were similar at around 56 -58 % of theoretical density (TD). The data show that the die pressed samples had the smallest amount of binder, 0.8 wt. %; followed by the gelcast samples, 3.3 wt. %; and the tape cast, 6.1 wt.%. Higher than expected weight losses were observed in both the gelcast and tape cast preforms during binder burn-out. This was probably due to the incomplete drying of water from the gelcast preforms or xylene and ethanol from the tape cast preforms. Figure 7 shows the results of TGA of the three types of preforms. The most prominent feature is the sharp weight loss for the tape cast material. The gelcast material shows a broader burn-out profile, allowing the binders to be removed at a relatively rapid rate (13 h), compared to 25 h cycle required to remove the binder from the tape cast material. Other studies have reported 30 to 60 h. furnace times to de-binder tape cast material.[5]

Figure 8 shows data for densification and weight changes during sintering of the three PZT types at 1200°, 1275°, or 1300° C for 3 h. Figure 8a shows that the sintered density of the gelcast material is higher than that of the die pressed material at 1200 °C, and comparable at 1275° and 1300° C. The tape cast materials had lower densities at all temperatures. These differences in sintered properties are probably due to small differences in the green densities, or due to differences in the green microstructures of the three sample types. The fact that the tape cast samples were fabricated by lamination of 5 to 6 tape discs may have affected the sintering behavior and resulted in the lower densities. Figure 8b shows the weight changes of the three materials at the three sintering temperatures. A slight weight gain is apparent in all three of the materials sintered at 1275 and 1300 °C. This weight gain

is thought not be due to increased incorporation of PbO into the sintered PZT materials from the $PbZrO_3$-ZrO_2 packing powder at the higher sintering temperatures.

The graphs in Figure 9 show (a) the piezoelectric charge constants, d_{33}; (b) the electromechananical coupling coefficients, k_p; and (c) the free relative dielectric constants, K^T_{33} (measured at 1000 Hz) of gelcast, tape cast and die pressed sintered PZT-4 materials. The results are average values from duplicate experiments. Figure 9a shows that the gelcast material has the highest d_{33} of the three sample types at sintered 1200 °C. The d_{33} values of the gelcast and die pressed samples increased with the sintering temperature, but the d_{33} value for the tape cast material deceased at 1300 °C. Two manufacturer's specifications for the d_{33} value of PZT-4 is 290 to 300 x 10^{-12} m/v.[6,7] Figure 9b shows the electromechanical coupling coefficients, k_p, of the samples sintered at the three temperatures. The die press and gelcast materials have similar values, but the tape cast values are consistently lower. Manufacturer's sources report a normal k_p of 0.58 to 0.62.[6,7] Figure 9c shows the relative dielectric constant, K^T_{33}, for the three materials. The K^T_{33} values of the die press and gelcast materials were similar for all three sintering temperatures, but were within the manufacturer's reported range (1250-1300),[6,7] for the 1275 °C materials. The tape cast material had lower K^T_{33} values at all sintering temperatures, but showed the same trend, with sintering at 1275 °C giving the highest value.

Figures 10, 11, and 12, respectively, show SEM photographs of uniaxially, die pressed, tape cast, and gelcast materials sintered at 1200 or 1300 °C. The average grain size is about 1.5 - 2 microns for all materials sintered at 1200 °C and is approximately 3 - 5 microns for materials sintered at 1300 °C. SEM microstructures of the die pressed, tape cast, and gelcast samples sintered at 1200° are very comparable. The same is true for all materials sintered at 1300 °C. This indicates that the forming method has little effect on the grain growth during the sintering process. The similarities in the microstructures do not explain the differences in electrical properties observed for different sample types sintered at the same temperature. However, the observed microstructures lend support to the idea that the higher d_{33} values observed in samples sintered at 1300°C are probably due to the larger grains in these samples, as compared to samples sintered at 1200°C.

Discussion

PZT-4 preforms were fabricated using gelcasting, tape casting, and die pressing methods. The gelcast materials, which were made using water-based slurries, showed very comparable piezoelectric properties to those fabricated by die pressing, and were superior to those fabricated by tape casting. The lower sintered densities and piezoelectric properties of the tape cast parts were possibly due to inferior microstructures of the green parts or due to flaws introduced into the parts during the lamination process. The binder burn-out of gelcast parts can be performed at the same rates as low-binder, die pressed parts, which is a big advantage over tape cast materials, which require much longer burn-out schedules.

Gelcast PZT Parts for Capability Demonstration

As mentioned in previous reports, an important feature of the work during the last year has been the comparison of forming techniques for PZT materials. Functional applications of PZT materials might require very simple disc shaped parts that could be formed via a die press method. In other instances such as multilayered PZT actuators, the application might require very thin, laminated PZT-metal preforms, that can most easily be formed via tape cast methods. Finally, the application might require strong machineable PZT green preforms, or PZT parts of complex shape, both of which can be made by gelcast methods.

To demonstrate gelcast forming, powders were gelcast using previously described techniques into plate and cylindrical shaped samples. Figure 13 is a photograph of several simple gelcast plates, discs, and rods, showing the ability to form gelcast parts of various sizes using appropriate molds.

Chemical Additions for Sintering PZTs at Lower Temperatures

This effort concentrate on the development of new processing methods and PZT compositions that allow the fabrication of PZT materials that can be co-sintered with silver palladium electrode materials (70 to 30 weight ratio) at temperatures below 1150°C, the melting point of the electrode material[8]. A literature search revealed several promising sintering additives, that might be combined with commercial PZT powders, to lower the sintering temperatures to below 1150°C.[9-16] The goal of the present effort is to determine if these sintering additives, when combined with a commercial PZT-4 powder (APC Ceramics Inc), will lower the sintering temperature below 1150°C.

Powders batches, A-E, were prepared by milling 50 g amounts of PZT-4 powder (APC Ceramics Inc.) with 1.0 g of one of the following: A) no additive (control), B) lead oxide, C) bismuth oxide (Bi_2O_3), D) niobium oxide (Nb_2O_3), or E) silver carbonate (Ag_2CO_3). In an attempt to gauge the effect of binder additives on the final product, either 1 wt.% of polyvinylpyrrolidone (PVP K-15) or Carbowax 8000 was added to each powder mix. Each powder was ball milled overnight in water using 1.25 cm diameter zirconia media. The powder batches were then dried at 65 °C in plastic pans. The dried powders were dry ball milled overnight. Since large agglomerates remained in the dry milled powders, powders were further processed to break up the aglomerates by Spex milling for 60 minutes in a 100 cc nylon jar with 5 zirconia balls), or by hand grinding using an alumina mortar and pestle.

Approximately 5.2 g of each powder mix was pressed into pellets (28.5 diameter by 1.5 mm thickness)using a steel die at 41 MPa. Binders were removed from the pellets by heating the pellets in air at 1 °C per minute to 300°C with a 1 h dwell, followed by heating at 1 °C per minute to 600 °C with a 2 h dwell and then a rapid cooldown. Pellets

were placed in alumina crucibles on top of TZ-O zirconia powder (Tosoh Inc). The sample crucibles were covered by an alumina lids, and to provide additional atmosphere protection, two sample crucibles were placed into a rectangular alumina tray, which was covered by platinum foil. Samples were sintered at one of the following conditions: 1120 °C for 3 h, 1120 °C for 24 h, 1150 °C for 48 h, or 1285 °C for 3 h. Samples were weighed before and after binder burn-out and sintering for weight change and green density determinations. Sintered densities were measured in absolute ethanol by the Archimedes immersion technique.

Results and Discussion

Figure 14 shows the densities obtained for the PZT samples sintered under the various sintering conditions. Note that the PZT-4 control sample, which did not have any additive, did not completely sinter after 3 h at 1120° C, but did sintered completely after 24 h at 1120° C. The density of this sample type decreased for the higher temperatures, probably due to the loss of PbO via volatilization. PZT-4 samples with added PbO, Nb_2O_3, or Ag_2CO_3 all sintered to greater than 97 % T. D.after 3 h at:
1120 °C, indicating their possible use as low temperature sintering additives.

Figure 15 shows the weight changes that occurred in samples of the five types during the sintering runs. All samples except group E, containing the Ag_2CO_3 additive, had the highest weight losses for the 1150 °C for the 48 h treatment. Group E had the greatest weight losses at 1287°C, probably due to the higher vapor pressure of silver at this temperature.

Work is underway in analyzing the electrical properties of the sintered samples.

Travel

23RD Annual Cocoa Beach Conference, Jan 24-29, 1999, Cocoa Beach, FL.

Publications

J. O. Kiggans, Jr., T. N. Tiegs, F. C. Montgomery, L. C. Maxey, and H. T. Lin, "Gelcast Forming of PZT Materials," to be published in the proceeding s of the 23RD Annual Cocoa Beach Conference, Jan 24-29, 1999.

Problems Encountered

None

References

1. B. Jaffe, W. R. Cook and H. Jaffe, Piezoelectric Ceramics, Academic press, 1971.
2. P. Bryant, "Optimisation of Poling Conditions for Piezoelectric Ceramics," in Ceramic Developments, eds. C. C. Sorrell and B. Ben-Nissan, Vol., 34-36, pp. 285-289. 1988.
3. R. E. Mistler, Engineered Materials Handbook, Vol. 4: Ceramics and Glasses, ASM International, pp. 161-165, 1991.
4. E. M. Anderson, R. A. Marra, and R. E. Mistler, Amer. Soc. Bull., Vol. 76 (7), pp. 45-50, 1997.
5. G. O. Dayton, et al, Forming of Ceramics, Eds. J. A. Mangels and G. L. Messing, Advances in Ceramics, Vol. 9. pp. 115-139, 1983.
6. American Piezo Ceramics, Inc. brochure.
7. Morgan Matroc, Inc. bulletin TP-226.
8. H. Hellebrand, Materials Science and Technology, eds. R. W. Cahn, P. Haasen, and E. J. Kramer, Vol. 17A, pp. 190-265, 1996.
9. S. Winzer, N. Shankar, and A. Ritter, "Designing Cofired Multilayered Electrostrictive Actuators for Reliability," J. Am. Ceram. Soc., 72, (12) pp. 2246 - 2257, 1989.
10. Wersing, W., Wahl, and Schnoller, " PZT-based multilayer Piezoelectric Ceramics with AgPd-Internal Electrodes," *Ferroelectrics*, Vol. 87, pp. 271-294, 1988.
11. Hwang, H., Watari, K., sando, M., and Toriyama, M., "Low-Temperature Sintering and High -Stenght $Pb(Zr,Ti)O_3$-Matrix Composites Incorporating Siver Particles," J. Am. Ceram. Soc., Vol. 80,, pp. 791-93, 1997.
12. Atkins, R. P., Holman, R. L., and Fulrath, R. M., "Substitution of Bi and Nb ions in Lead Zirconate Titanate," ," J. Am. Ceram. Soc., Vol. 54,, pp. 113-15, 1971.
13. Wittmer, D. E., and Buchanan, "low Temperature Densification of Lead Zirconate Titanate with Vanadium Pentoxide Additions," J. Am. Ceram. Soc., Vol. 64, pp. 486-90 1981.
14. Lucuta, P. Gr., Constantinescu, Fl., and barb, D., "Structural Dependance on Sintering Temperature of Lead Zirconate Titanate Solid Solutions, J. Am. Ceram. Soc., Vol. 68, pp. 533-37, 1981.
15. Akbas, M. A., McCoy, M. A., and Lee, W. E., " Microstructural Evolution during Pressureless Sintering of Lead Lanthanum Zirconate Titanate Ceramics with Excess Lead (II) Oxide, J. Am. Ceram. Soc., Vol. 78, pp. 2417-24, 1995.
16. Kingon, A. I. and Clark, J. B., Sintering of PZT Ceramics: II, Effect of PbO Content on Densification Kinetics," J. Am. Ceram. Soc., Vol. 66, pp. 256-260, 1982.

Table 1. Weight Loss data for gelcast, tape cast, and die pressed preforms.

Sample Type	Green Density (% TD)	Expected Wt. Loss (%) During Binder Burn-Out*	Wt. Loss (%)
Gelcast	55.9 - 56.4	3.3	4.9 - 7.5
Tape-Cast Laminated	56.0 – 58.0	6.1	8.0 - 8.4
Die Pressed	56.1 - 56.5	**	0.8 - 0.84

*Based on non-volatile additives in the formulation
**Binder added by APC Ceramics, Inc.

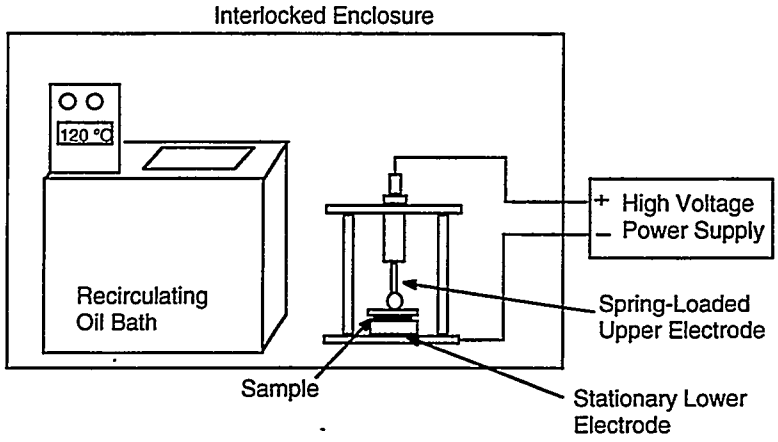

Figure 1. Drawing of poling apparatus

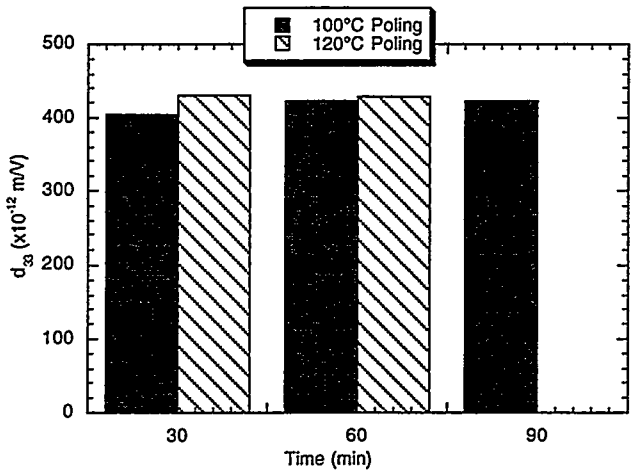

Figure 2. Piezoelectric charge constant (d_{33}) for APC discs poled at ORNL at 2kV/mm at 100 and 120 °C.

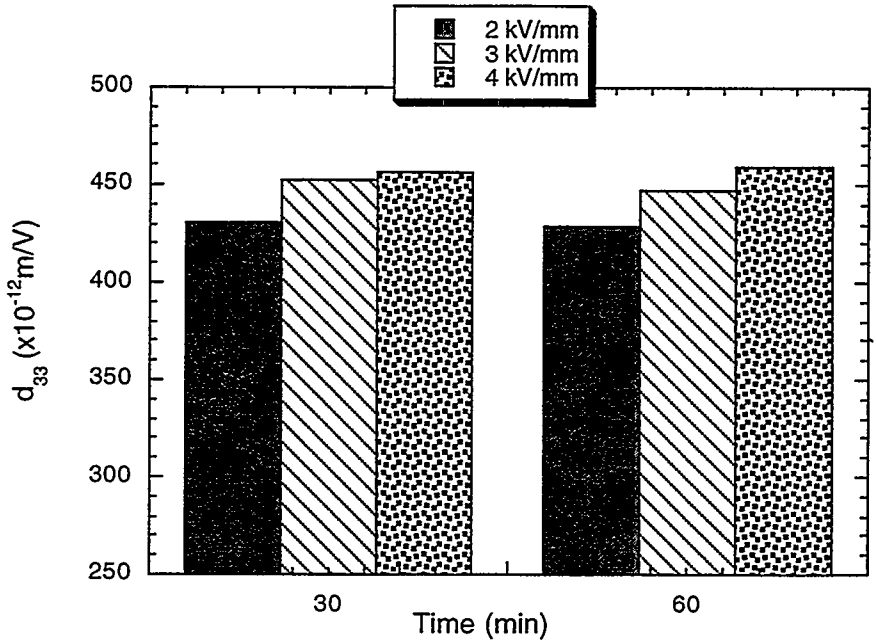

Figure 3. Piezoelectric charge constant (d_{33}) for APC discs poled at ORL with 2,3,or 4 kV/mm at 120 °C.

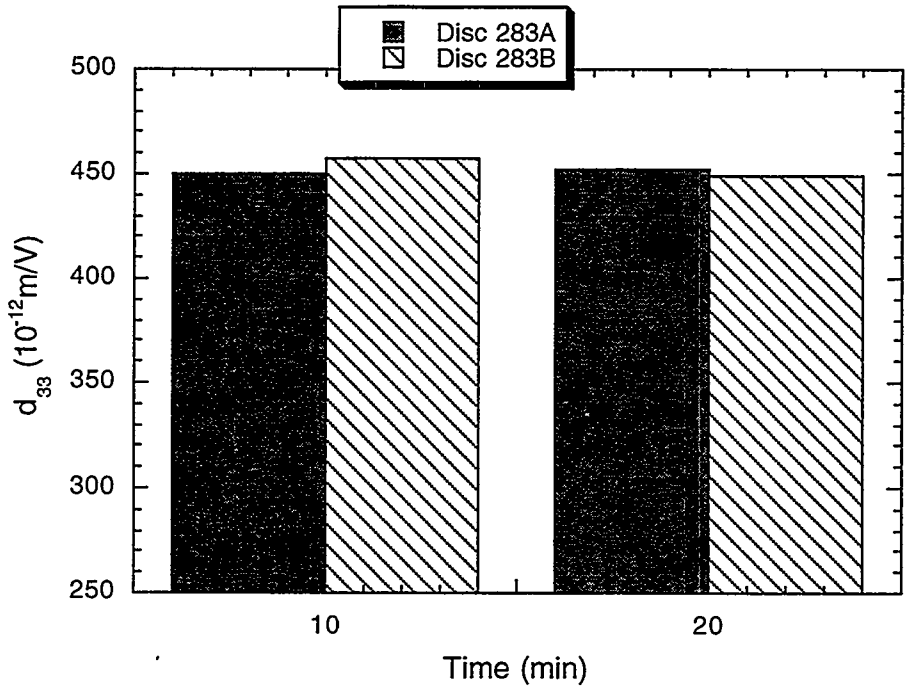

Figure 4. Piezoelectric charge constant (d_{33}) for two APC discs poled at ORNL at 120 °C and 3 kV for 10 or 20 min..

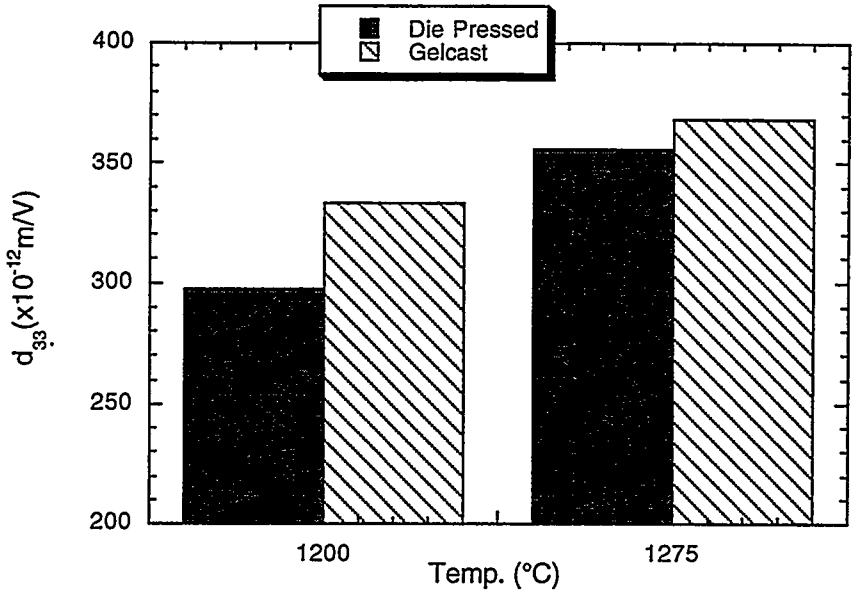

Figure 5. Piezoelectric charge constant (d_{33}) for ORNL fabricated, die pressed and gelcast PZT materials sintered at 1200 or 1275 °C.

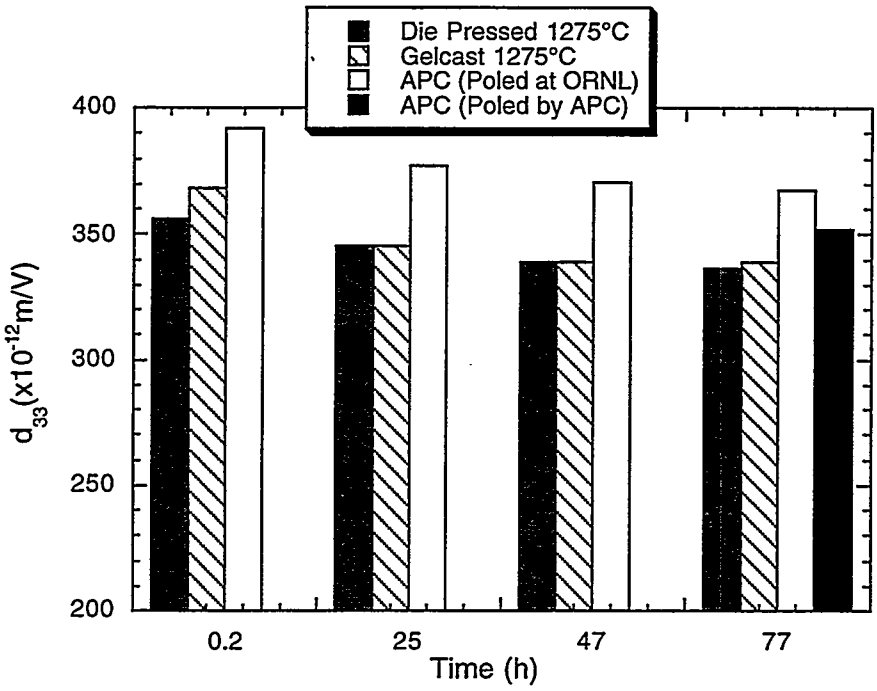

Figure 6. Piezoelectric charge constant values (d_{33}) showing aging behavior for various purchased or ORNL, fabricated PZT materials.
Note. the as purchased APC discs were aged for an unknown period of time prior to measurements.

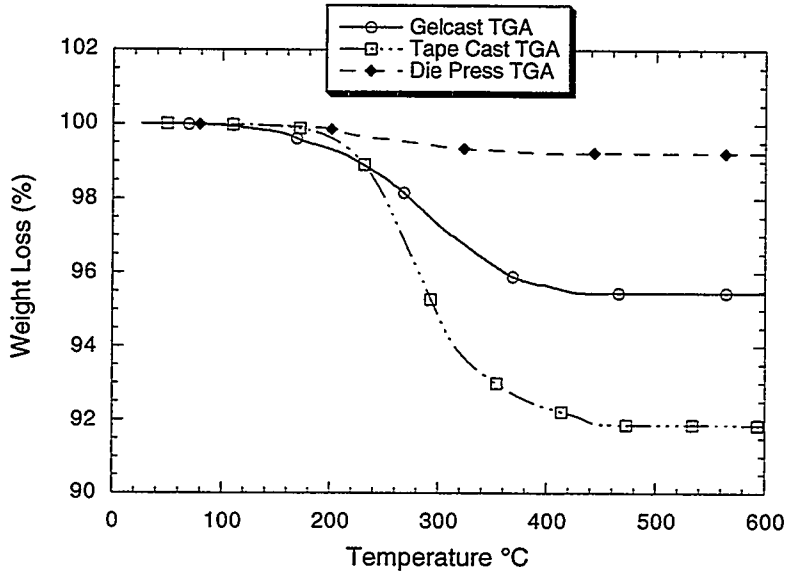

Figure 7. Graph of TGA results for gelcast, tape cast, and die press preforms.

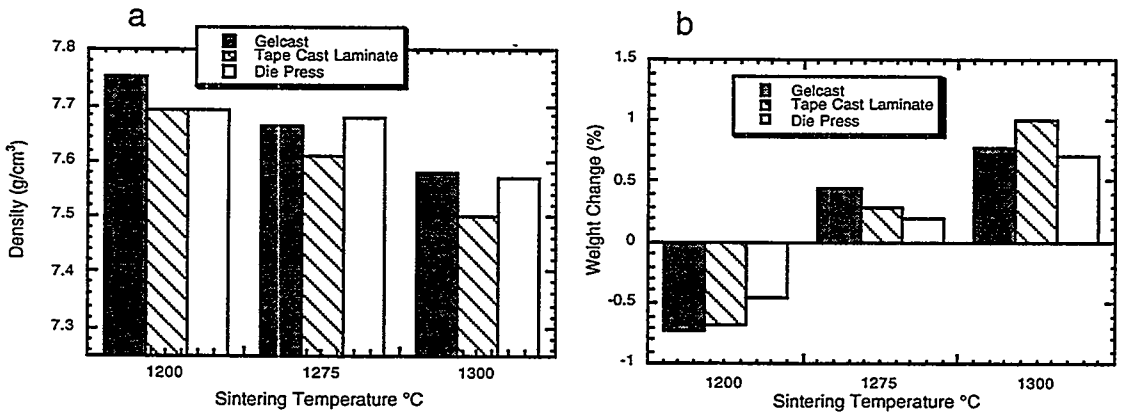

Figure 8. a) Final density and b) weight change for PZT-4 materials sintered at 1200°, 1275°, or 1300 °C for 3 h.

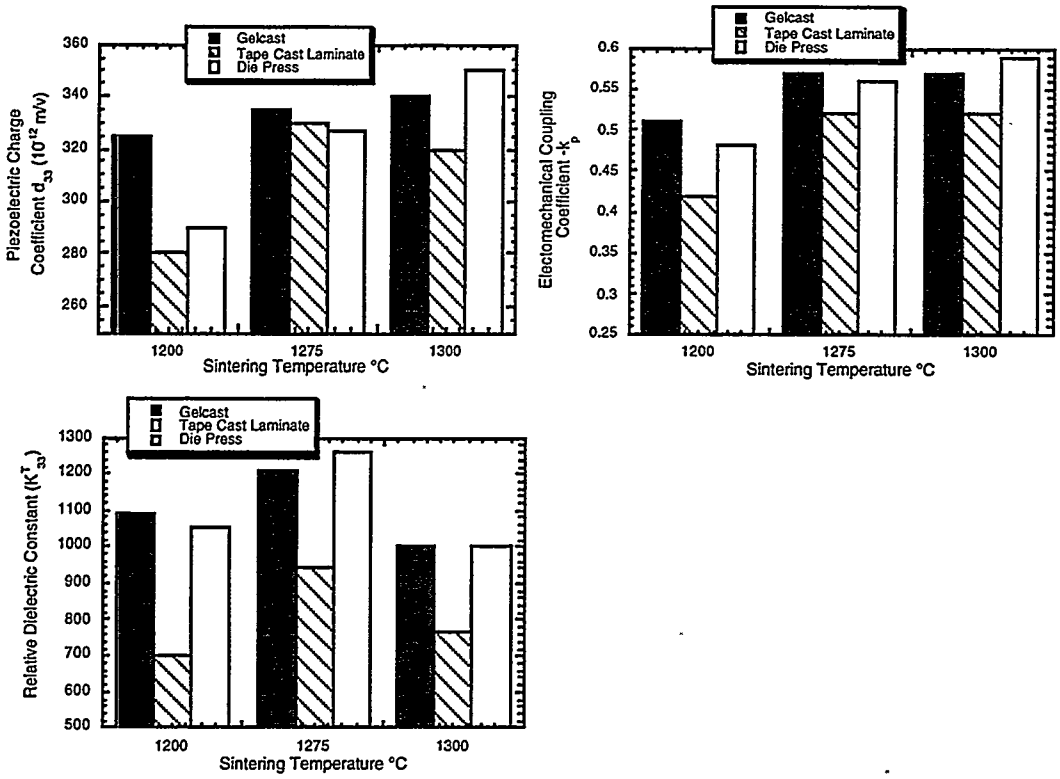

Figure 9. Selected piezoelectric properties (a) piezoelectric charge coefficient, d_{33}, (b) electromechanical coupling coefficient, k_p, and (c) free relative dielectric constant, K^T_{33}, (at 1000 Hz) of sintered gelcast, die pressed, and tape cast materials as a function of sintering temperature.

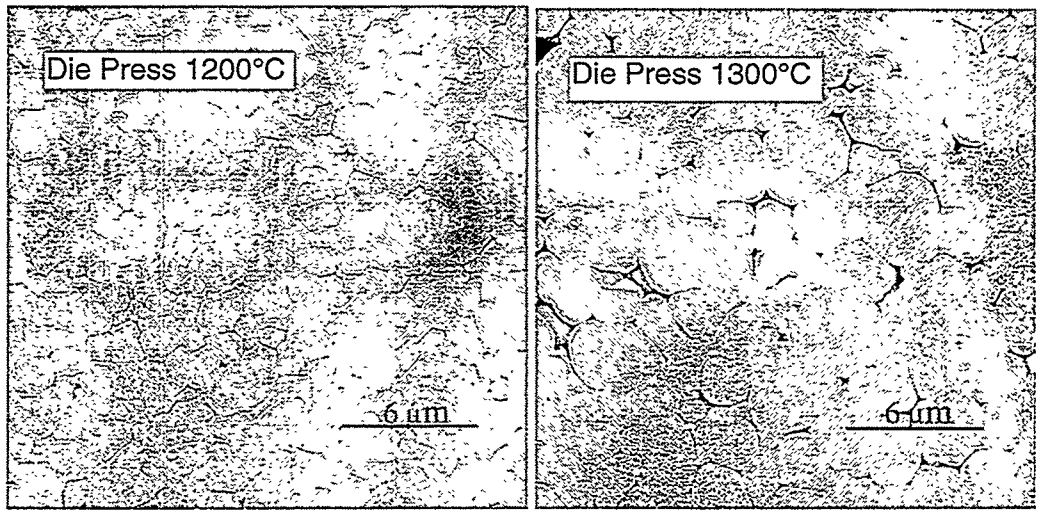

Figure 10. SEM photographs of PZT-4 die pressed material sintered to 1200 or 1300°C.

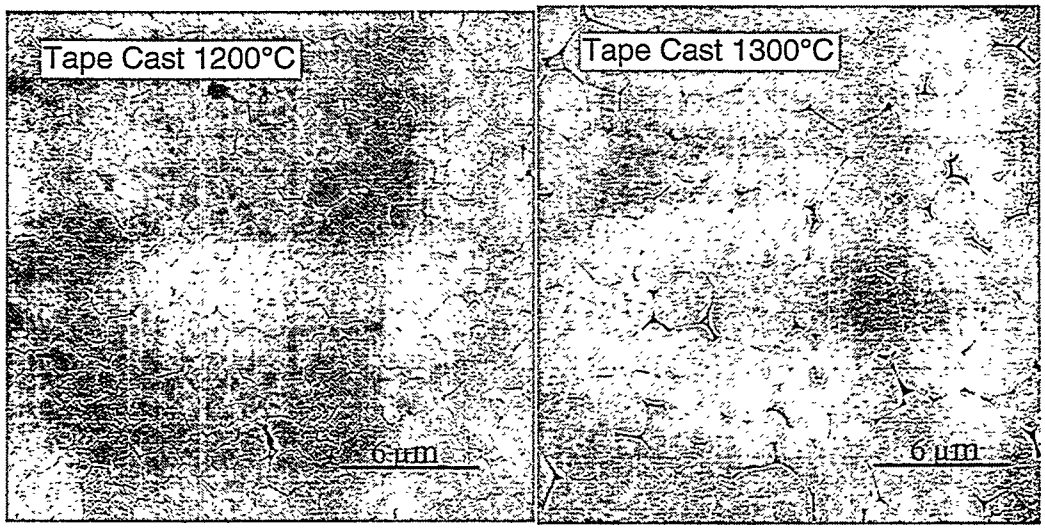

Figure 11. SEM photographs of PZT-4 tape cast material sintered to 1200 or 1300°C.

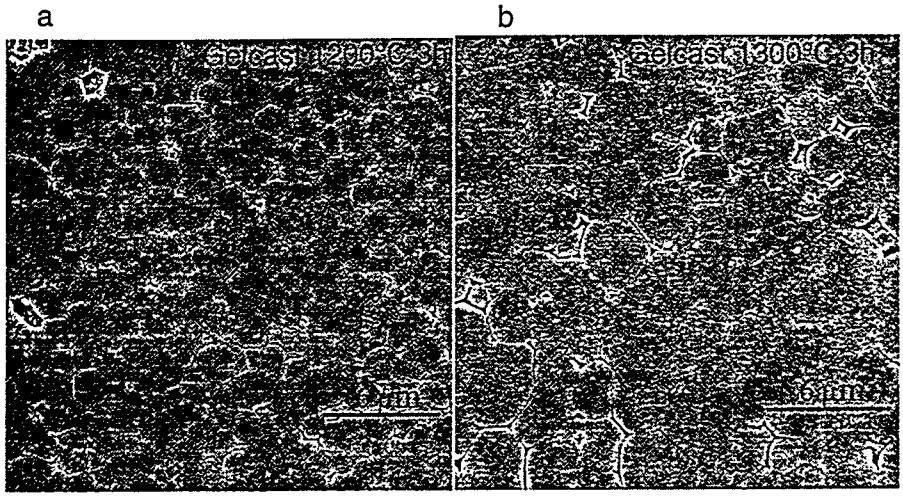

Figure 12. SEM photographs of gelcast ,sintered, PZT-4 materials to (a)1200 or (b) 1300 °C.

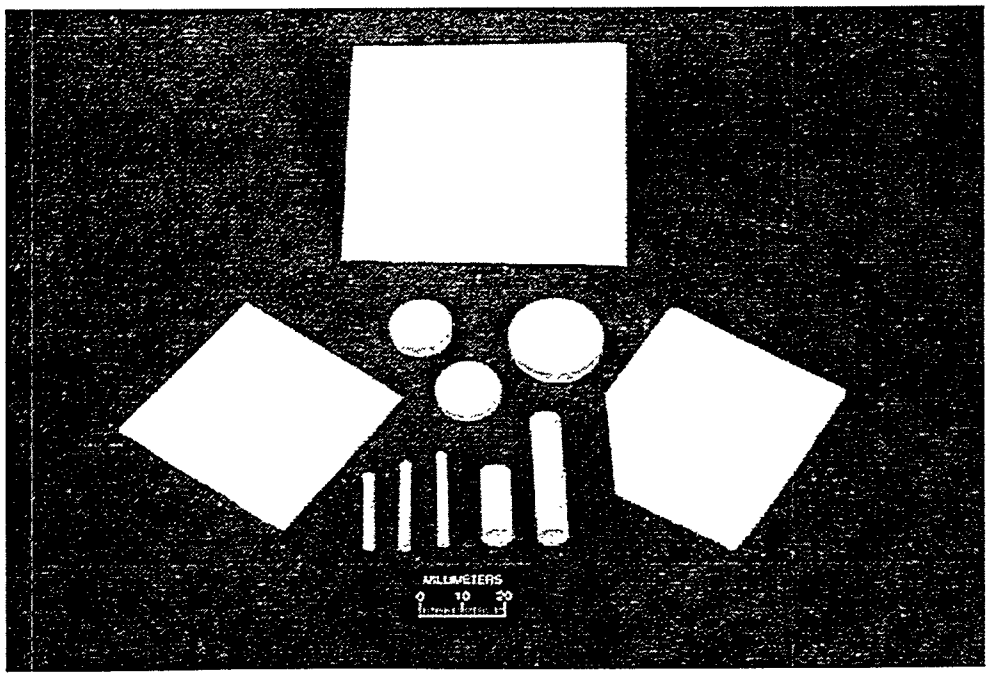

Figure 13. Photo of PZT gelcast demonstration parts.

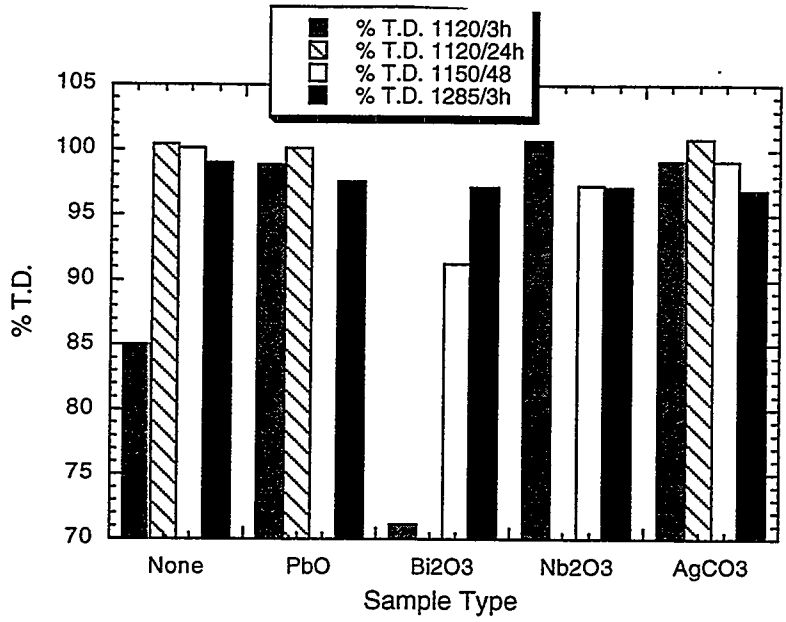

Figure 14. Densities of PZT-4, with and without sintering additives, under noted sintering conditions.

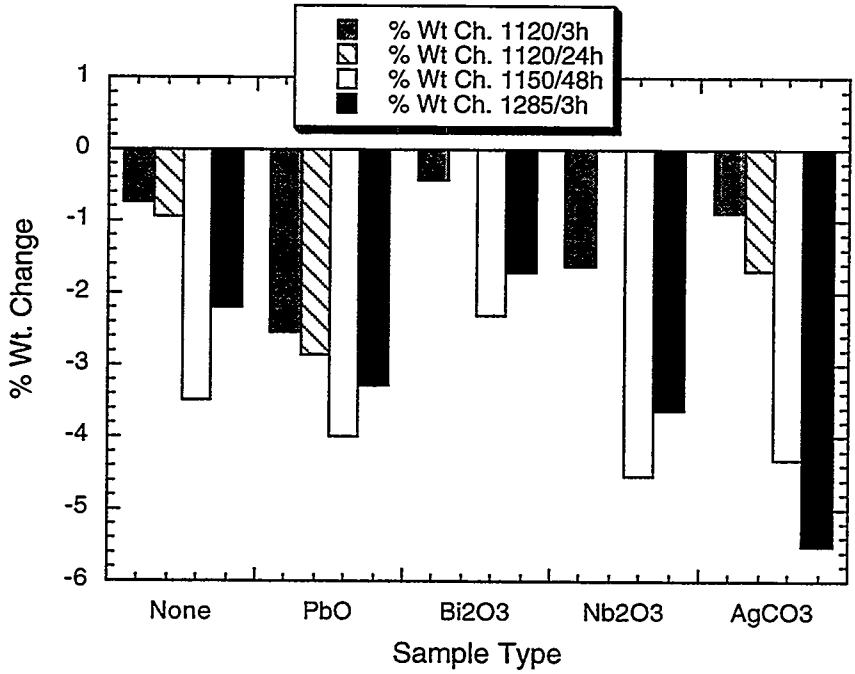

Figure 15. Weight changes for PZT-4 with and without sintering additives, under noted sintering conditions.

LOW COST-HIGH TOUGHNESS CERAMICS

T. N. Tiegs, F. C. Montgomery, J. L. Schroeder, M. R. Snyder, and D. L. Barker
Oak Ridge National Laboratory
Oak Ridge, TN 37831

Objective/Scope

Significant improvement in the reliability of structural ceramics for advanced diesel engine applications could be attained if the critical fracture toughness (K_{Ic}) were increased without strength degradation. Early results from ORNL research showed that significant increases in fracture toughness could be achieved by manipulating the microstructure to promote toughening mechanisms such as crack bridging. Excellent properties were obtained in this manner for the alumina and mullite matrix systems reinforced with SiC whiskers. In silicon nitride, mechanical property improvements were achieved by promoting acicular or elongated grain growth and these provided significant toughening on the same order as the whisker reinforced materials. Currently, the project is initiating studies on toughening of ceramics by two methods: microstructure development in oxide-based ceramics, and incorporation of ductile intermetallic phases.

Technical Highlights

In-Situ Toughening of Oxide-Based Ceramics by Microstructure Development

Microstructure manipulation has been used to increase the fracture toughness of ceramics for many years. Mainly, this has been done in the silicon nitride-based systems where growth of acicular grains has been encouraged. Recently, oxide-based ceramics have been studied to achieve the same type of results observed with silicon nitride. Thus, because of the large potential, a study was initiated to develop in-situ toughened oxide-based ceramics.

Prior results have shown that anisotropic grain growth readily occurs in several alumina and mullite compositions. The results on the densification behavior and microstructure characterization have been reported previously.

The fracture toughness of selected samples from both the mullite and alumina systems was measured by indentation and the results are summarized in Table 1. While the toughness values are not close to those for silicon nitrides, if one examines the toughness differences between the materials exhibiting anisotropic grains and those that do not, some improvement is apparent. For example, with the mullite specimens, toughness for the equiaxed grain samples was in the range of 2.0-2.3 MPa$\sqrt{m}$, which is normal for mullite. Where anisotropic grains were observed, the toughnesses were from 2.4 MPa$\sqrt{m}$ to as high as 3.7 MPa$\sqrt{m}$. In the alumina system, the toughness differences were not as significant. For equiaxed grains, the toughnesses averaged ~3.1 MPa$\sqrt{m}$, which is expected for alumina. The materials exhibiting anisotropic grains were only slightly higher at 3.5 to 3.6 MPa$\sqrt{m}$. The high value for the Na_2O doped materials is questionable because of the low density. Thus it can be seen that the anisotropic grains account for at least a modest increase in fracture toughness.

Polished and etched specimens revealed the anisotropic nature of the grains. However, as shown previously, crack growth from a Vickers indentation on a Fe_2O_3-doped mullite shows that the majority of crack propagation was transgranular. The same behavior was evident in the alumina-based materials. Consequently, toughening mechanisms did not operate effectively and the measured fracture toughness values were relatively low. To

increase toughening, debonding between the anisotropic grains and the intergranular phases must be promoted.

From these studies it can be concluded that anisotropic grain growth in both mullite- and alumina-based systems can be enhanced by several dopant additions. For mullite these include SrO, MnO, NiO, Fe_2O_3 or Y_2O_3. For alumina these are $\geq$ 5% Na_2O; 5% Na_2O-5% SiO_2; 4.5% Na_2O-0.5% Na_3AlF_6; and 5% La_2O_3. In both cases, interlocking grain microstructures can be produced. However, the bonding between the grains and the intergranular phases is apparently very strong. The result is that during fracture and crack propagation, little to no debonding occurs between these different phases and the crack planes are relatively flat. Consequently, toughening mechanisms, such as crack bridging and deflection are not operable and there is only minor improvements in fracture toughness. It should also be noted that the addition of the dopants to the mullite and alumina matrices inhibited densification and higher temperatures were required to obtain densities comparable to the monolithic material. While the fracture toughness may not have been increased significantly by the anisotropic grains, other properties, such as high temperature creep resistance, may be improved.

The present technology of adding dopants to encourage anisotropic grain growth, in general, does show some improvement in fracture toughness compared to the monolithic materials. It remains to be seen if the improvements are adequate for structural applications in diesel engine environments. In the case of mullite with Mn additions, there was an encouraging result with a fracture toughness of K_{Ic}=3.7 MPa$\sqrt{m}$. This is significantly higher than monolithic mullite, however, it needs to be confirmed with additional testing.

The final conclusion of this study is that, indeed, acicular grains can be grown in oxide-based matrices and modest improvements in toughness can be achieved. However, strong bonding between grains prevents toughening mechanisms to operate and significantly increase fracture toughness. Therefore, if any improvements in toughness are to be realized in oxides, there is a need, and thus an opportunity, to engineer grain boundaries so that debonding occurs. This aspect will be the thrust of future work.

At the present time, samples are being fabricated that will test various methods to promote debonding at ceramic interfaces. Two methods will be initially investigated. These are: (1) modification of the matrix-intergranular phase chemistry, and (2) utilization of differences in thermal expansion between phases.

Aluminide-Bonded Ceramics

Previous studies have shown that the properties of the aluminide-bonded ceramics (ABC) are attractive for diesel engine applications and consequently, development of these materials was started. Issues to be studied include the fabrication of parts using cost-effective processing, effect of alloying elements on the properties and fabrication of near-net-shape parts for testing. Initially, a study was done to examine the sintering behavior of the aluminide-bonded ceramics at high binder contents. Most of the previous work on ABC's was done at binder contents of 10-30 vol. %. However, higher binder contents on the order of 30-50 vol. % are necessary for these composites to match the thermal expansion of steel.

TiC-Ni_3Al composites were prepared by two different methods: (1) sintering with pre-alloyed gas-atomized Ni_3Al powders, or (2) reaction sintering with fine elemental powders to form Ni_3Al in-situ. The results on the densification behavior and microstructure characterization have been reported previously.

During the present reporting period, the mechanical properties were determined. A summary of the flexural strength results is shown in Fig. 3. As indicated, the strength generally increased with increasing Ni_3Al content. This is most likely due to the slight improvement in densification with the higher binder contents. The results also show a significant difference between the composites made with prealloyed powders and those made by reaction sintering of elemental powders. The reason for the poor strengths of the reaction sintered materials is being determined. Previous results on TiC-40 vol. % Ni_3Al composites fabricated by reaction sintering showed strengths of approximately 1150 MPa, which is more similar to those on the materials made with prealloyed powders in the present results.[1]

Like the strength, the fracture toughness generally increased with increasing Ni_3Al volume content as shown in Fig. 4. That was anticipated. Also like the strength results, the composites made with prealloyed powders exhibited higher toughness that those fabricated by reaction sintering. In all cases, the fracture toughness was $K_{Ic} > 10$ MPa$\sqrt{m}$ and for the composite with 50 vol. % Ni_3Al and fabricated with prealloyed Ni_3Al powders was > 25 MPa$\sqrt{m}$. These values are exceptional and were the basis for the choice of these types of composites for development for diesel engine applications in this project.

The indent hardness was measured on several specimens sintered at different temperatures and is summarized in Fig. 5. As shown, the hardness decreased with increasing Ni_3Al content with the samples fabricated with prealloyed powders having slightly higher values. The effect of temperature and Ni_3Al content on the final grain size is shown in Fig. 6. As expected, larger grain sizes were noted at higher sintering temperatures and larger Ni_3Al contents. The reaction sintered materials had smaller grain sizes than the composites fabricated with prealloyed powders.

Earlier work showed that the alloying additives affect the sintering behavior and properties of the aluminide bonded ceramics. Consequently, a series of samples was fabricated to determine the effect of alloying additives on the sintering behavior and properties of the aluminide-bonded TiC as indicated in Table 2. The results on the densification behavior have been reported.

The hardness and fracture toughness as measured on polished sections of the specimens are shown in Figs. 7 and 8, respectively. As indicated, the hardness was generally in the range of 7 to 10 GPa. In instances where the hardness was lower, this was most likely a result of the densities also being lower. For most compositions, the hardness was highest for the materials sintered at 1450°C. Higher temperatures would result in larger grain sizes and decreased hardness is thus expected. When examining the effect of the additive type, the highest hardness values were associated with the additions of Mo, W and Co.

The fracture toughness was highest for the compositions containing Fe at various contents. Substantial toughness improvements were associated with the addition of Fe (Composition DC-25, $Ni_{1.50}Fe_{2.00}Al_{0.50}$). The toughness values were generally >10 MPa$\sqrt{m}$ with the exception for the Co containing composite. These results excellent resistance to crack growth for these types of composites.

Status of Milestones

On schedule.

Communications/Visits/Travel

Travel by T. N. Tiegs to attend the American Ceramic Society Electronics Division Meeting in San Diego, CA, November 1-4.

Travel by T. N. Tiegs to Orlando, FL, November 17-18, 1998 to attend a Program Coordination Meeting for the Metal Powder Industries Federation 1999 International Conference on Powder Metallurgy and Particulate Materials.

Travel by T. N. Tiegs to present a paper at the American Ceramic Society Engineering Ceramics Division Meeting in Cocoa Beach, FL, January 25-28, 1999.

Problems Encountered

None.

Publications

T. N. Tiegs, M. R. Snyder, F. C. Montgomery, J. L. Schroeder and D. W. Coffey, "Effect of Dopants on Anisotropic Grain Growth in Oxide-Matrix Materials," to be published in Ceram. Eng. Sci. Proc., (1999).

References

1. K. P. Plucknett, T. N. Tiegs, P. F. Becher, S. B. Waters and P. A. Menchhofer, "Ductile Intermetallic Toughened Carbide Matrix Composites," Ceram. Eng. Sci. Proc., 17 [3] 314-321 (1996).

Table 1. Summary of fracture toughness results on anisotropic grain mullite and alumina.

Composition	Sintering Conditions (°C/h)	Density (% T.D.)	Anisotropic Grain Growth Observed	Fracture Toughness K_{Ic} (MPa$\sqrt{m}$)
Mullite- ITM-Fe-1	1600/3	95.1	Yes	2.4±0.7
Mullite- ITM-La-1	1600/3	97.6	No	2.3±0.5
Mullite- ITM-Co-1	1600/3	95.5	No	2.0±0.2
Mullite- ITM-Mn-1	1600/3	96.1	Yes	3.7±0.2
Mullite- ITM-Ni-1	1500/3	94.5	Yes	2.6±0.4
Alumina-5% Na_2O	1650/1	88.2	Yes	3.7
Alumina-5% SrO	1650/1	95.4	Yes	3.6
Alumina-5% MgO	1650/1	97.5	No	3.1
Alumina-0.5% Na_2O	1650/1	98.7	No	3.2
Alumina-0.5% SrO	1650/1	99.2	No	3.4
Alumina-0.5% MgO	1650/1	99.5	No	2.9
Alumina-0.5% Li_2O	1650/1	96.2	No	3.2
Alumina-5% Fe_2O_3	1650/2	100	No	3.0
Alumina-5% Y_2O_3	1650/2	100	No	3.0
Alumina-5% La_2O_3	1650/2	100	Yes	3.5

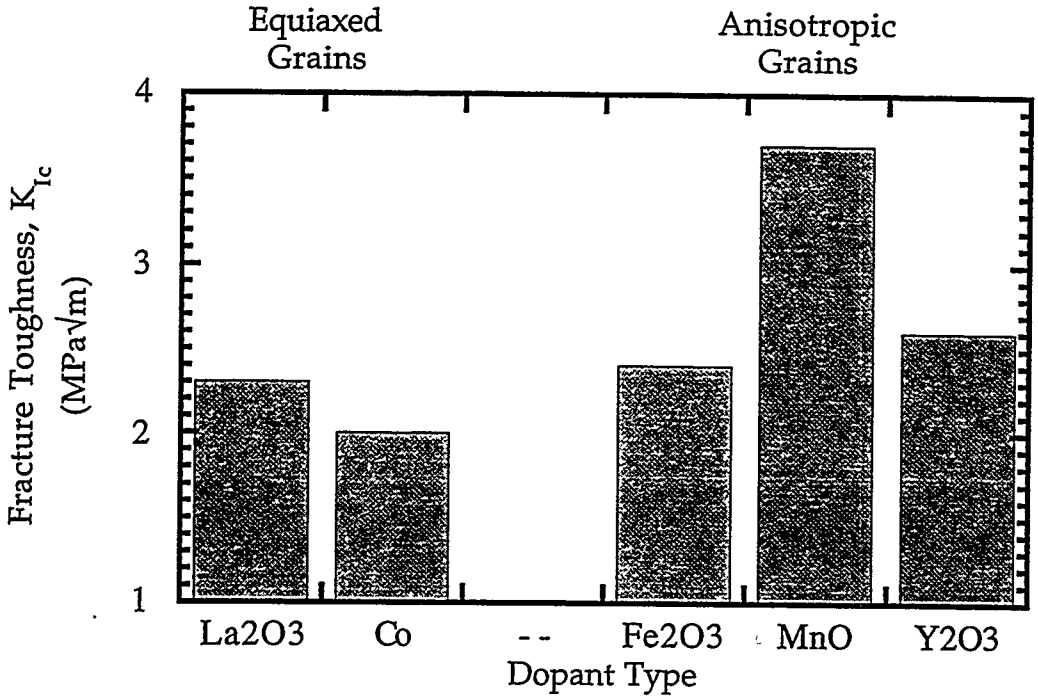

Fig. 1. Summary of fracture toughness results on mullite with various dopants. Modest improvements in toughness associated with anisotropic grain growth.

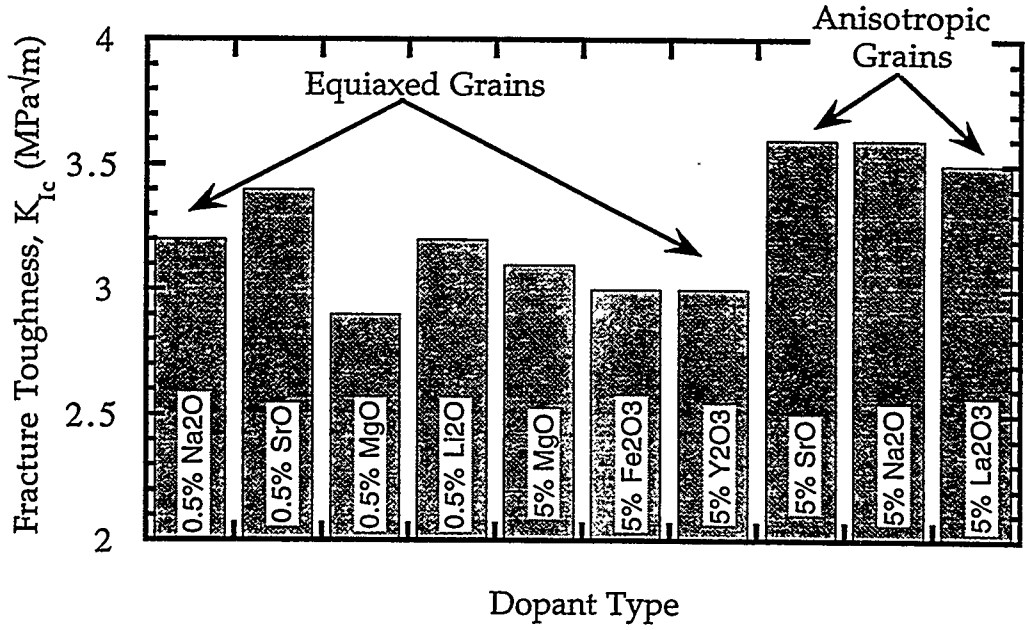

Fig. 2. Summary of fracture toughness results on alumina with various dopants. Modest improvements in toughness associated with anisotropic grain growth.

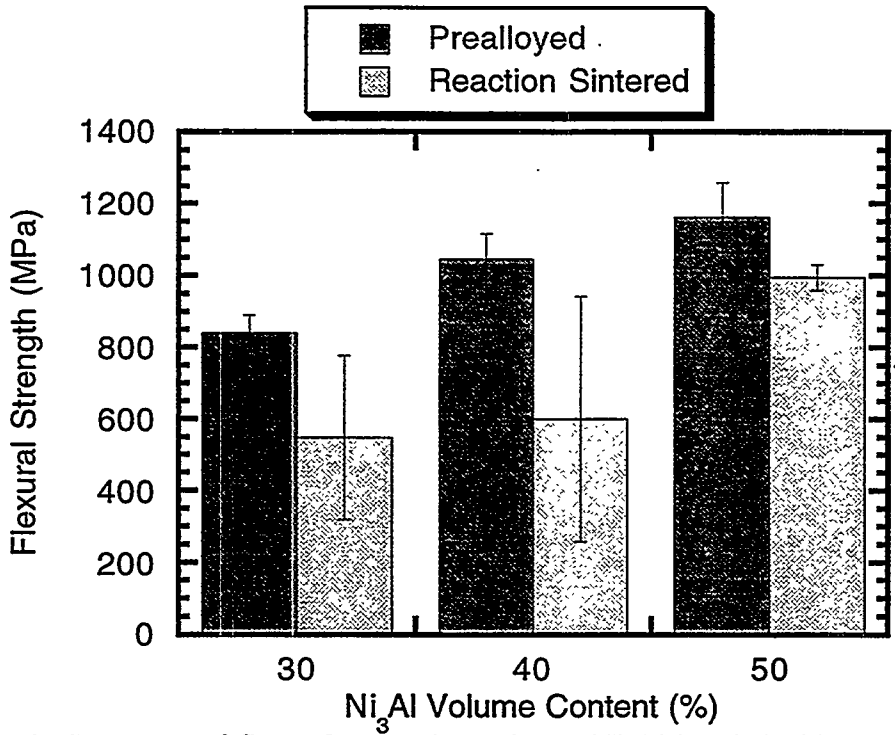

Fig. 3. Summary of flexural strength results on Ni_3Al-bonded TiC composites fabricated using either prealloyed Ni_3Al powders or reaction sintered with elemental powders. Sintering was done at 1450°C for 1 hour.

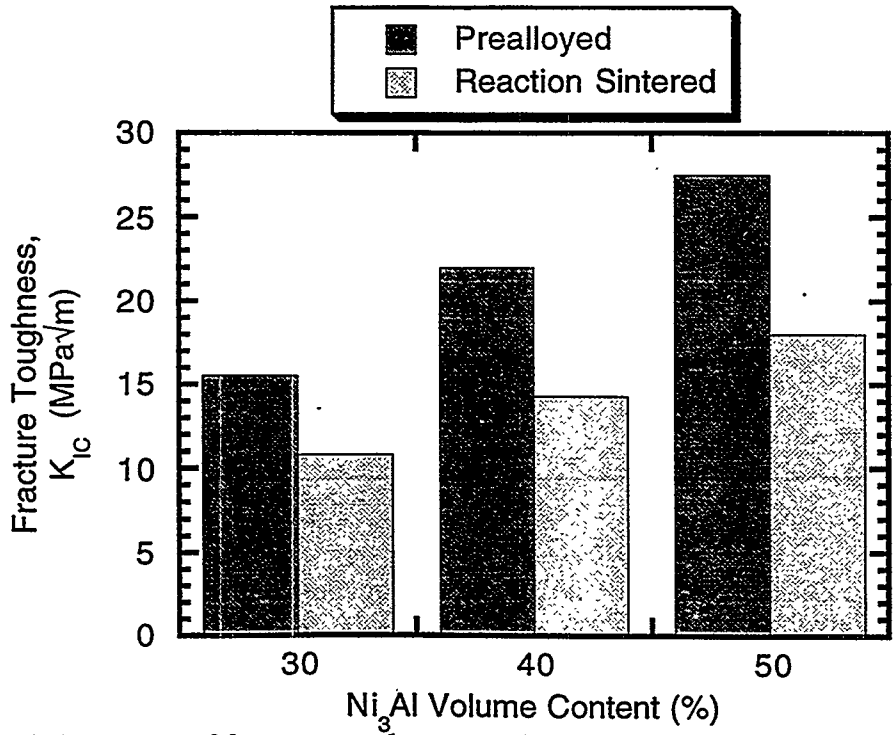

Fig. 4. Summary of fracture toughness results on Ni_3Al-bonded TiC composites fabricated using either prealloyed Ni_3Al powders or reaction sintered with elemental powders. Sintering was done at 1450°C for 1 hour.

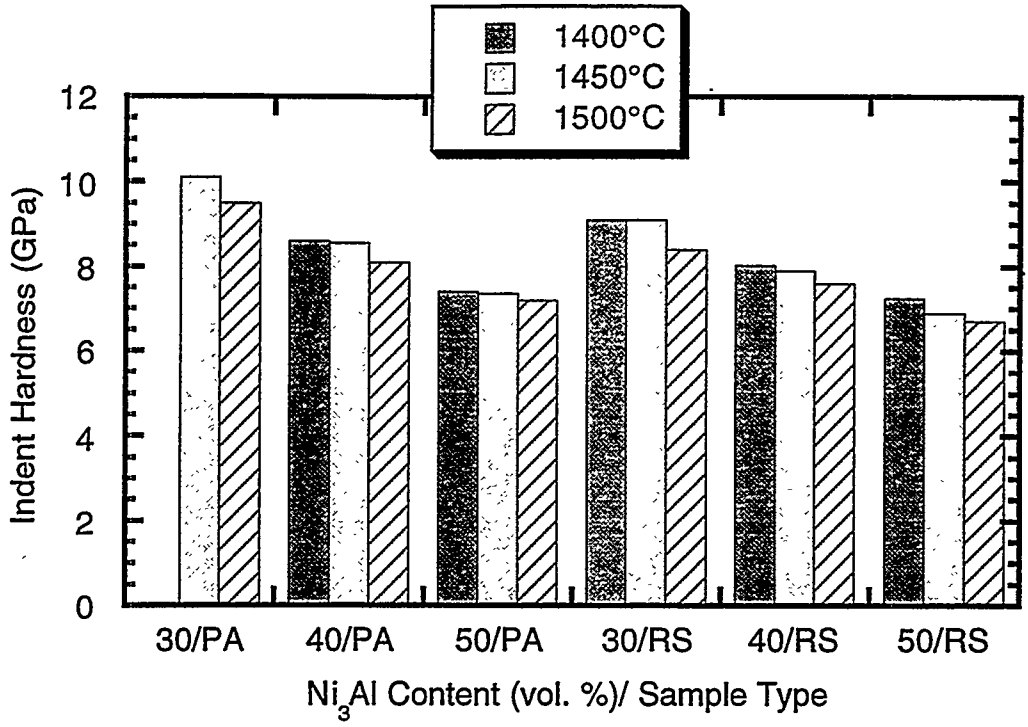

Fig. 5. Summary of indent hardness results on Ni_3Al-bonded TiC composites fabricated using either prealloyed Ni_3Al powders (PA) or reaction sintered with elemental powders (RS). Sintering was done at the specified temperature for 1 hour.

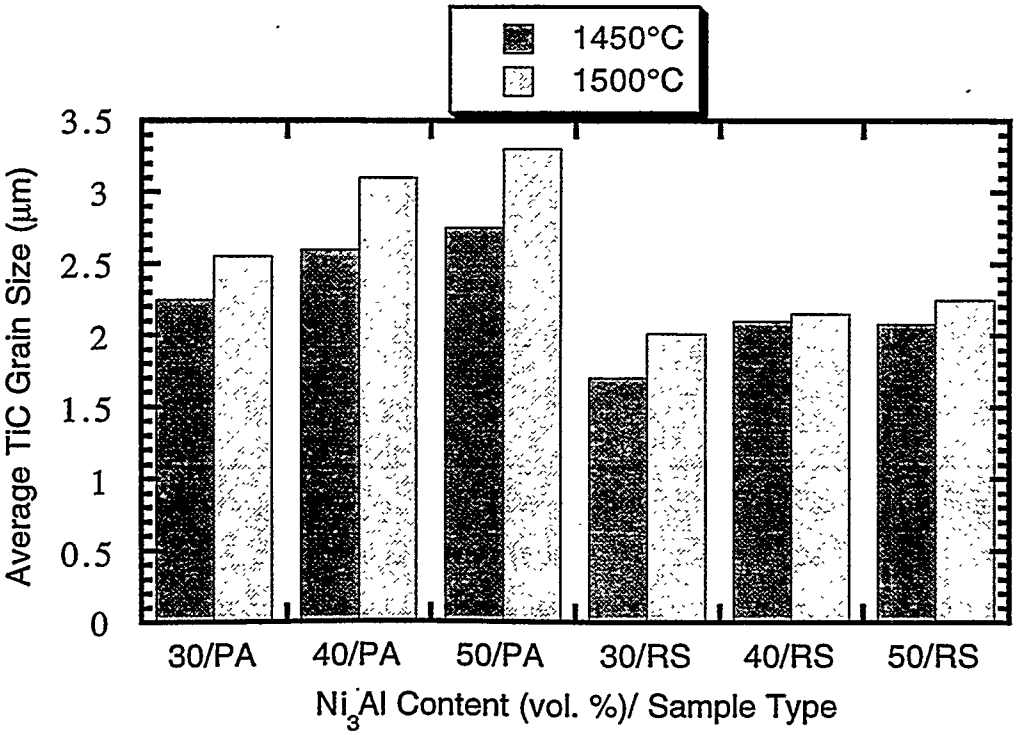

Fig. 6. Summary of average TiC grain size on Ni_3Al-bonded TiC composites fabricated using either prealloyed Ni_3Al powders (PA) or reaction sintered with elemental powders (RS). Sintering was done at the specified temperature for 1 hour.

Table 2. Samples of aluminide-bonded TiC ceramics fabricated to determine the effect of alloying additives on the sintering behavior and properties of the aluminide-bonded TiC. All samples fabricated with 30 vol. % of the Ni_3Al binder phase by reaction sintering of elemental powders.

Specimen No.	Binder Composition	Substitution Site of Alloying Element
DC-22	$Ni_{2.85}Fe_{0.15}Al_{1.00}$	Both Ni and Al
DC-23	$Ni_{2.85}Fe_{0.20}Al_{0.95}$	Both Ni and Al
DC-24	$Ni_{2.40}Fe_{0.80}Al_{0.80}$	Both Ni and Al
DC-25	$Ni_{1.50}Fe_{2.00}Al_{0.50}$	Both Ni and Al
DC-26	$Ni_{2.85}Cr_{0.20}Al_{0.95}$	Both Ni and Al
DC-27	$Ni_{2.40}Cr_{0.80}Al_{0.80}$	Both Ni and Al
DC-28	$Ni_{3.00}Si_{0.20}Al_{0.80}$	Al Sites
DC-29	$Ni_{3.00}Ti_{0.20}Al_{0.80}$	Al Sites
DC-30	$Ni_{3.00}Mo_{0.20}Al_{0.80}$	Al Sites
DC-31	$Ni_{3.00}W_{0.20}Al_{0.80}$	Al Sites
DC-32	$Ni_{2.40}Co_{0.60}Al_{1.00}$	Ni Sites
DC-33	$Ni_{3.00}Zr_{0.20}Al_{0.80}$	Al Sites

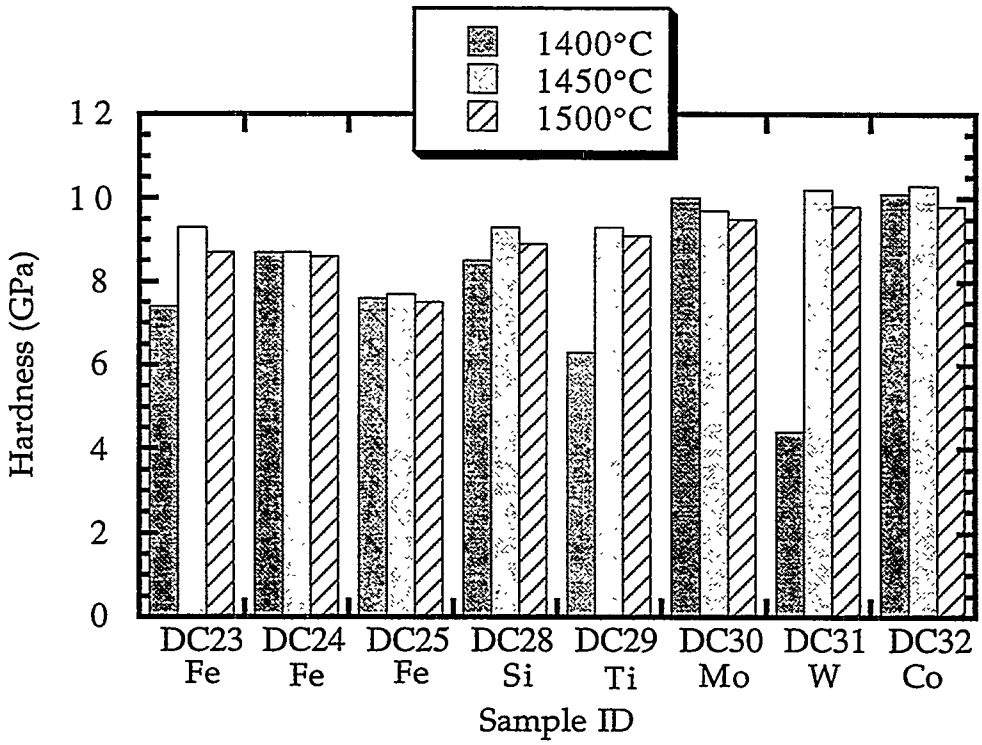

Fig. 7. Summary of results on the effect of alloying additives on the hardness of Ni_3Al-bonded TiC composites. The specimens were fabricated by reaction sintering with elemental powders (RS). Sintering was done at the specified temperature for 0.8 hour.

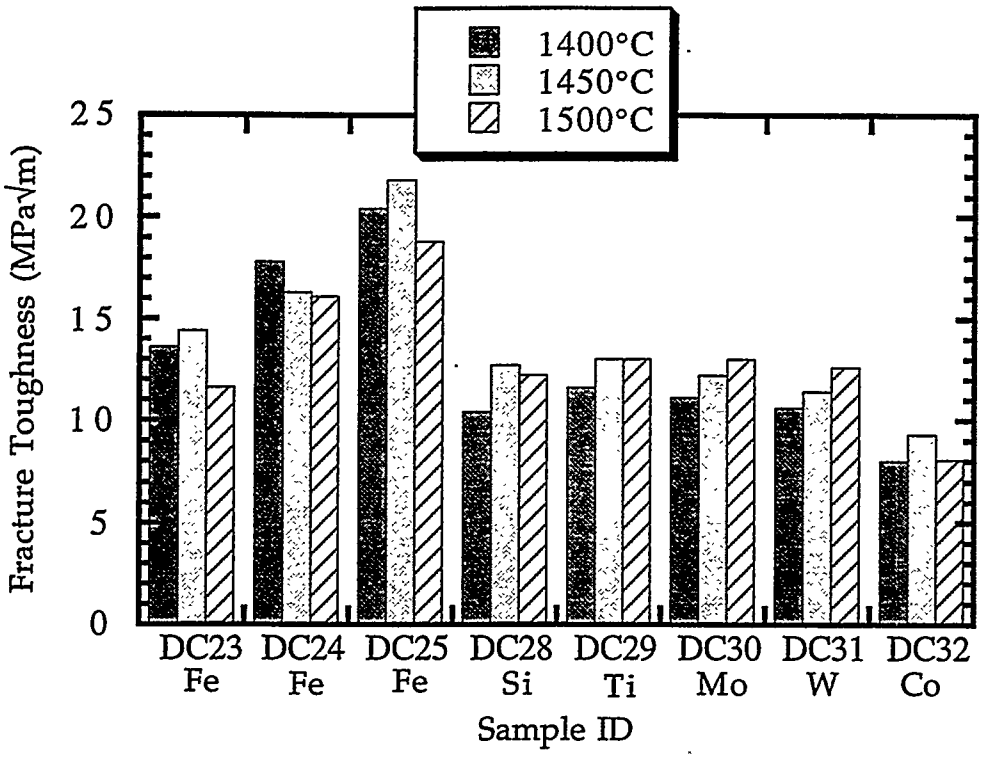

Fig. 8. Summary of results on the effect of alloying additives on the fracture toughness of Ni_3Al-bonded TiC composites. The specimens were fabricated by reaction sintering with elemental powders (RS). Sintering was done at the specified temperature for 0.8 hour.

Cost Effective Sintering of Silicon Nitride Ceramics (SIU-C)-
D. E. Wittmer, Southern Illinois University, Carbondale, IL 62901

Objective/Scope

The purpose of this work is to investigate the potential of cost effective sintering of Si_3N_4 through the development of continuous sintering techniques and the use of lower cost Si_3N_4 powders and sintering aids. The addition of a recent task has added the objective of investigating the cost effective sintering of advanced carbides and cermets.

Technical Highlights

Task 1. Refine Economic Model and Design for Chosen Furnace Configuration

This task was completed as reported in a previous semiannual report.

Task 2. Continue evaluation of sintering parameters on properties of selected Si_3N_4 compositions

Prototype Belt Furnace

During this reporting period, Centorr Vacuum Industries, Inc. has redesigned the graphite hot zone to provide better insulation and thermal uniformity. In the present system, there is too much heat being lost to the furnace interior chamber. This results in an overheating of the furnace top and ends. In addition, there has been a problem at low temperature in the thermal uniformity from the front to the back of the hot zone. This non-uniformity can cause density gradients in the parts being inter-metallic bonded carbides, carbides and nitrides being sintered. The new hot zone is presently being manufactured and will be installed and tested during the next reporting period.

1. Collaboration with Industrial Partners and Affiliates

Work continues according to plan to develop collaborations with industrial partners. Due to the proprietary/confidential relationships established, the results of these collaborations will be reported as part of their individual programs.

2. Silicon Nitride Valves for SAE Car

The Honda 600 cc engine, which is the prototype for the engine to be used in the SAE car competition, presently the engine has over 4,000 road test miles on the silicon

nitride valves and has been driven on an official race track. The performance data suggests that both mileage and horsepower have been improved by the addition of these valves, however further improvements can only be obtained through the addition of another camshaft.

4. Evaluation of Continuous Sintering of Silicon Nitride-Titanium Carbide

In this work, 4 lots of Ube silicon nitride containing 5 wt% TiC (3 of the lots used H. C. Starck high-purity grade TiC and 1 lot used the ultra-fine, high-purity TiC produce by Dr. Rasit Koc at SIUC) were processed in the A3Y9 composition for comparison with the baseline A3Y9 formulation. The physical properties obtained to date are given in Tables I and II.

As seen in these tables, none of the formulations achieved complete densification at the temperatures normally used to sinter the A3Y9 formulation. This was because the TiC converts to TiN at elevated temperatures, causing out-gassing of CO. At low sintering temperatures, moderately high densities were achieved. The strength and toughness values measured for the TC3 and TC4 are comparable to some commercial silicon nitride products. It would appear that the finer TiC from Dr. Koc produced marginally higher density, strength and fracture toughness for some of these sintering conditions. These values would be expected to improve with increase in density or the use of pressure. It should be noted that most compositions containing significant amounts of TiC are hot pressed or HIPed to achieve high density. Because of the TiC conversion to TiN, TiN substitution for TiC was also investigated.

To determine the effect of TiN additions, three lots of A3Y9 using Ube silicon nitride containing 5 wt% TiN (H. C. Starck high-purity grade) were processed. TN1 contained the as-received Starck TiN, while the TiC in TN2 was turbomilled for 24 hours and the TiN in TN3 was turbomilled for 32 hours, prior to batching and sintering. Following sintering, the billets were machined into type-B ASTM test bars by outside vendors. Table III gives the data generated to date for the formulation containing TiN.

As seen from the results, all of the formulations containing TiN achieved 100% or greater than the target density and achieved strengths of greater than 90% of the baseline formulation. It would appear that the turbomilling of the TiN has increased both the strength and fracture toughness, compared with the as-received TiN. Also, the addition of TiN appears to have had a significant effect on the fracture toughness, compared with the baseline formulation. Work is continuing of this task to determine the effect on other properties, such as thermal expansion and thermal shock resistance.

Task 3. Continue Evaluation of Low Cost Si_3N_4 Powders

Nothing to report this reporting period.

Task 4. Design and Construct Prototype Belt Furnace

This task has been completed.

Task 5. Continuous Sintering of Inter-metallic Bonded Carbides

During this reporting period, the 13 formulations of inter-metallic bonded carbides prepared by Terry Tiegs at ORNL were continuously sintered for about 30 min. at peak temperature in flowing Ar at 1450°C and 1500°C. Following sintering the density and weight change for each formulation was determined and then the specimens were returned to ORNL. The samples were cut in half and then half was returned to SIUC for evaluation, while ORNL kept the other half for evaluation. The physical properties and microstructures are presently being determined and compared with the same formulations that were batch sintered at ORNL under Ar pressure. The density results for the formulations sintered at SIU are compared with the densities obtained by ORNL in their pressure furnace in Tables IV and V.

Status of Milestones

1.	Refine Economic Model and Design for Chosen Furnace Configuration	Completed
2.	Continue Evaluation of Sintering Parameters on Properties of Selected Si_3N_4 Compositions	On Schedule
3.	Continue Evaluation of Low Cost Si_3N_4 Powders	On Schedule
4.	Design and construct prototype belt furnace	Completed
5.	Continuous sintering of inter-metallic bonded carbides	On Schedule

Problems Encountered

None

Publications and Presentations

J. Smith, M. Lee, D. Wittmer, A. Migone, Y. Jiang, and R. Koc, "Preparation and Properties of TiC/Silicon Nitride Composites for Synchrotron Analyses," Presented at the 9th APS User Meeting, Argonne National Laboratory, Advanced Photon Source, October 13-15, 1998.

D. E. Wittmer, F. Goranson, T. Tiegs, and J. Schroeder, "Aluminide-Bonded TiC Sintered by Two Methods," American Ceramic Society 101st Annual Meeting, April 29, 1999 in Indianapolis, IN.

J. Smith, D. E. Wittmer, M. Lee, and A. Migone, "Effect of TiC and TiN Additions on the Properties of Silicon Nitride Composites," American Ceramic Society 101st Annual Meeting, April 29, 1999 in Indianapolis, IN.

D. Wittmer, F. Goranson, T. Tiegs and J. Schroeder, "Comparison of Batch and Continuous Sintering of Aluminide-Bonded TiC," Abstract for PMTECH '99, Vancouver, BC, June 20-24, 1999.

Table I. Continuous Sintering Results for Baseline A3Y9 and A3Y9-TiC Using Commercial TiC

Designation	Sintering Conditions		% Theor. Density	4-Pt. Flexural Strength (MPa)	K_{IC} Fracture Toughness (MPa • $m^{1/2}$)
	Temperature (°C)	Time (min)			
Baseline A3Y9 Formulation	1790	120	100.0	953 +/- 52	6.49 +/- 0.02
	1775	120	100.0	1003 +/- 139	6.52 +/- 0.08
	1725	120	99.4	1018 +/- 41	**
TC1 95/5 As-received TiC† Granulated & CIP'ed	1815	90	90.2	421 +/- 79	6.06 +/- 0.05
	1790	120	88.8	440 +/- 72	5.31 +/- 0.97
	1750	120	93.0	526 +/- 25	5.92 +/- 0.10
	1725	120	93.8	464 +/- 31	5.78 +/- 0.04
	1700	120	94.6	482 +/- 43	5.25 +/- 0.08
TC2 95/5 Pre-milled TiC† Granulated & CIP'ed	1790	120	90.1	478 +/- 31	5.47 +/- 0.15
	1775	120	92.8	505 +/- 66	6.05 +/- 0.14
	1750	120	94.8	510 +/- 44	5.17 +/- 0.22
	1725	120	94.0	437 +/- 97	5.36 +/- 0.19
	1700	120	92.7	485 +/- 27	5.31 +/- 0.25
	1675	120	95.2	482 +/- 70	4.80 +/- 0.03

† Commercial TiC provided by H.C. Starck

** Data not completed

Table II. Continuous Sintering Results for A3Y9-TiC Using Commercial TiC and TiC from Koc

Designation	Sintering Conditions		% Theor. Density	4-Pt. Flexural Strength (MPa)	K_{IC} Fracture Toughness (MPa • $m^{1/2}$)
	Temperature (°C)	Time (min)			
TC3 95/5 Pre-milled TiC† Pressure Cast & CIP'ed	1775	120	92.0	699 +/- 112	5.72 +/- 0.03
	1750	120	94.7	504 +/- 26	**
	1725	120	94.5	784 +/- 50	5.60 +/- 0.01
	1725	90	89.9	378 +/-11	**
	1700	120	94.5	704 +/- 67	4.93 +/- 0.67
	1675	120	95.8	744 +/- 69	**
TC4 95/5 TiC†† from Koc Pressure Cast & CIP'ed	1775	120	93.6	677 +/-227	5.92 +/- 0.12
	1750	120	94.9	782 +/- 83	5.97 +/- 0.14
	1725	120	95.3	749 +/- 60	5.62 +/- 0.06
	1700	120	95.9	696 +/- 124	5.38 +/- 0.10

† Commercial TiC provided by H.C. Starck

†† Sample TiC produced and provided by Dr. Koc

** Data not completed

Table III. Continuous Sintering Results for Baseline A3Y9 and A3Y9-TiN Using Starck Commercial TiN

Designation	Sintering Conditions		% Theor. Density	4-Pt. Flexural Strength (MPa)	K_{IC} Fracture Toughness (MPa • $m^{1/2}$)
	Temperature (°C)	Time (min)			
Baseline	1790	120	100	953 +/- 52	6.49 +/- 0.02
A3Y9 Formulation	1775	120	100	1003 +/- 139	6.52 +/- 0.08
	1725	120	99.4	1018 +/- 41	**
TN1 95/5	1775	120	100	798 +/- 44	7.03 +/- 0.23
As-received TiN	1750	120	100	860 +/- 143	7.44 +/- 0.03
Pressure Cast & CIP'ed	1725	120	98.8	874 +/- 30	6.54 +/- 0.11
	1700	120	98.6	783 +/- 81	6.73 +/- 0.12
TN2 95/5	1775	120	100.9	992 +/- 45	**
TiN Turbomilled 24 h	1750	120	100.6	963 +/- 85	**
Pressure Cast & CIP'ed	1725	120	98.7	803 +/- 83	6.36 +/- 0.12
	1700	120	99.0	811 +/- 57	5.80 +/- 0.15
TN3 95/5	1775	120	101.0	923 +/- 34	**
TiN Turbomilled 32 h	1750	120	100.9	888 +/- 63	**

Table IV. Continuous Sintering Results for Inter-metallic bonded TiC Composites 1450°C/1 h

Sample ID	Matrix/% Binder Type	% Target Density SIU Continuous Furnace	% Target Density ORNL Pressure Furnace
DC-22G	$Ni_{2.85}\ Fe_{0.15}\ Al_{1.00}$	98.2	97.6
DC-23	$Ni_{2.85}\ Fe_{0.20}\ Al_{0.95}$	98.2	98.2
DC-24	$Ni_{2.85}\ Fe_{0.80}\ Al_{0.80}$	97.7	98.2
DC-25	$Ni_{1.50}\ Fe_{2.00}\ Al_{0.50}$	99.8	95.4
DC-26	$Ni_{2.85}\ Cr_{0.20}\ Al_{0.95}$	93.6	92.7
DC-27	$Ni_{2.40}\ Cr_{0.80}\ Al_{0.80}$	91.1	93.6
DC-28	$Ni_{3.00}\ Si_{0.20}\ Al_{0.80}$	99.5	98.2
DC-29	$Ni_{3.00}\ Ti_{0.20}\ Al_{0.80}$	99.9	98.9
DC-30	$Ni_{3.00}\ Mo_{0.20}\ Al_{0.80}$	99.6	99.1
DC-31	$Ni_{3.00}\ W_{0.20}\ Al_{0.80}$	93.9	98.7
DC-32	$Ni_{2.40}\ Co_{0.60}\ Al_{1.00}$	97.3	98.8
DC-33	$Ni_{3.00}\ Zr_{0.20}\ Al_{0.80}$	84.3	91.0

All binder additions were made by reaction sintering.

Table V. Continuous Sintering Results for Inter-metallic bonded TiC Composites 1500°C/1 h

Sample ID	Matrix/% Binder Type	% Target Density SIU Continuous Furnace	% Target Density ORNL Pressure Furnace
DC-22H	$Ni_{2.85}\ Fe_{0.15}\ Al_{1.00}$	98.8	98.8
DC-23	$Ni_{2.85}\ Fe_{0.20}\ Al_{0.95}$	99.2	98.7
DC-24	$Ni_{2.85}\ Fe_{0.80}\ Al_{0.80}$	98.7	99.0
DC-25	$Ni_{1.50}\ Fe_{2.00}\ Al_{0.50}$	99.1	99.0
DC-26	$Ni_{2.85}\ Cr_{0.20}\ Al_{0.95}$	95.1	97.2
DC-27	$Ni_{2.40}\ Cr_{0.80}\ Al_{0.80}$	94.9	98.6
DC-28	$Ni_{3.00}\ Si_{0.20}\ Al_{0.80}$	99.5	99.3
DC-29	$Ni_{3.00}\ Ti_{0.20}\ Al_{0.80}$	99.1	99.8
DC-30	$Ni_{3.00}\ Mo_{0.20}\ Al_{0.80}$	98.9	100.3
DC-31	$Ni_{3.00}\ W_{0.20}\ Al_{0.80}$	96.1	94.0
DC-32	$Ni_{2.40}\ Co_{0.60}\ Al_{1.00}$	97.5	106.1
DC-33	$Ni_{3.00}\ Zr_{0.20}\ Al_{0.80}$	86.7	95.8

All binder additions were made by reaction sintering.

ADVANCED MANUFACTURING TECHNOLOGY

Durability of Diesel Engine Component Materials

Peter J. Blau, R. L. Martin, and B. C. Dumont
Oak Ridge National Laboratory

Objective/Scope

The objective of this effort is to enable the development of more durable, low-friction moving parts in diesel engines for heavy vehicle propulsion systems by conducting friction, lubrication, and wear analyses of advanced materials, surface treatments, and coatings. The scope of materials and coatings is broad and includes any metallic alloy, intermetallic compound, ceramic, or composite material which is likely to be best-suited for the given application. Parts of current interest include valves, valve guides, and scuffing-critical components, like fuel injector plungers. Hot scuffing is a primary surface damage mode of interest. Bench-scale simulations of the rubbing conditions in diesel engine environments are used to study the accumulation of surface damage, and to correlate this behavior with the properties and compositions of the surface species. The effects of mechanical, thermal, and chemical factors on scuffing and reciprocating sliding wear are being determined, and the results will be used to refine material selection strategies for durability-critical engine components.

Technical Highlights

Investigation of Silicon Nitride Materials for Use in Valve Guides. Two types of test were evaluated for use in this effort: a twin-bar-on-valve-stem test, and a reciprocating ball-on-flat test. Due to inherent problems with specimen alignment, the former arrangement, described in previous reports, was discontinued in favor of the later configuration. The ball material was chosen to be stainless steel 316 because its micro-indentation hardness is similar to Cr-plated valve stems and it also has chromium oxide on its surface, like Cr-plating. The candidate guide materials were two silicon nitride-based ceramics: NT-451 (Norton Company) and a Si_3N_4 ceramic matrix composite (CMC) containing 10% SiC and 30% TiC , developed by Ford Motor Company. Two diesel oils, a commercial 30-weight composition obtained from Caterpillar, Inc. ('Oil #1') and a Ag-containing oil ('Oil #2'), were used in these tests. The second oil, provided by R. Spence, Lubricant Additives Research, Cleveland, Ohio, has a viscosity of about 10.3 cSt at 100°C (grade 15W30). Silver is suspended in the form of ultra-fine particles which are intended to become activated so as to form lubricating films during contact. These two lubricants were compared to determine whether the Ag would offer any advantages for lubricating ceramics over conventional diesel oil. Friction and wear data were obtained for the various materials combinations and lubricants at room temperature and 170°C. Tribological data were coupled with surface chemical analysis and electron microscopy to identify dominant wear mechanisms.

Tables 1 and 2 summarize the friction and wear results of these tests, respectively. Steady-state kinetic friction coefficients for both ceramics, in both oils, averaged approximately 0.12 at room temperature. At elevated temperature, they ranged from about 0.06 to 0.16, depending on the lubricant used. Lubricated wear rates of the ceramic materials tended to be lower for the CMC (3×10^{-8} mm^3/N-m) than for the NT-451 (1.5×10^{-7} mm^3/N-m). Likewise, the wear of the stainless steel was lower against the composite than against the NT-451 (1-5 x 10^{-7} mm^3/N-m, and 0.5-3 x 10^{-6} mm^3/N-m). These results suggest that silicon nitride materials can be made more compatible with metallic counterfaces in

reciprocating wear situations by the judicious selection of particulate additions. No clear or significant effects of Ag additives in the oil were observed.

Table 1. Friction Data

Flat Spec. Material	Lubricant	Temp.	Duration (m)	Initial μ*	Transition begins (min)	Final μ**
NT-451	Oil#1	room	1600	0.14	none (1 test)	0.12
	Oil#2	room	400-1600	0.14	15 (1/3 tests)	0.12
CMC	Oil#1	room	400 1600	0.155 0.13 0.13	none 120 50	0.14 0.08 0.1
	Oil#2	room	400-1600	0.12	none (3 tests)	0.12
NT-451	Oil#1	170°C	1200	0.16	none (1 test)	0.16
	Oil#1	170°C	1600	0.14	none (1 test)	0.17
	Oil#2	170°C	320	0.165	none	0.15
	Oil#2	170°C	1200	0.15 0.15	40 35	0.08 - 0.09 0.08 - 0.085
CMC	Oil#1	170°C	1200 1600	0.11 0.13	4 (1 test) 5 (1 test)	0.06 - 0.10 0.05 - 0.09
	Oil#2	170°C	200	0.142	none	0.148
	Oil#2	170°C	1200	0.13 0.14	20 35	0.08 0.085

* Measured after the rapid transient period of breaking-in which occurred within the first 2-3 minutes.
** Measured at the maximum indicated sliding distance.

Table 2. Wear Data

Material	Lubricant	Temp.	Duration (m)	316 St Steel Ball (x 10^{-6} mm/N-m)	Flat Specimen (x 10^{-6} mm/N-m)
NT-451	Oil#1	room	1600	0.52	0.15
	Oil#2	room	400	1.10	0.10
	Oil#2	room	800	0.80	0.08
	Oil#2	room	1600	0.55	0.08
CMC	Oil#1	room	400	1.8	0.09
	Oil#1	room	1600	0.52, 0.15*	0.02, 0.01*
	Oil#2	room	400	0.15	0.05
	Oil#2	room	800	0.65	0.05
	Oil#2	room	1600	0.64	0.03
NT-451	Oil#1	170°C	1200	2.60	0.10
	Oil#1	170°C	1600	2.81	0.13
	Oil#2	170°C	320	3.60	0.42
	Oil#2	170°C	1200	1.2 0.9	0.16 0.1
CMC	Oil#1	170°C	1200 1600	0.08 0.06	0.04 0.03
	Oil#2	170°C	200	2.3	0.17
	Oil#2	170°C	1200	0.48, 0.64*	0.03, 0.04*

* These tests were repeated.

High-Temperature Scuffing of Diesel Engine Components. An annotated bibliography on the characteristics and measurement of scuffing phenomena has been prepared. The information in this bibliography has been used to design a new, high-temperature scuffing test system. Cummins Engine Company is working with us to evaluate the proposed design and to determine how the ORNL system can best meet their needs for scuffing data. In approaching this effort, it was important to: (1) establish performance requirements for the testing system, (2) select a contact geometry that will permit cost-effective evaluation of a wide variety of candidate materials, including coatings, and (3) ensure that the type of scuffing data produced will be in a form useful to diesel engine designers.

After considering a variety of possibilities, the contact geometry has been established for the high-temperature scuffing system. Establishing the contact geometry is important because it determines both the form of materials that can be evaluated and the relevance of the results to specific applications.

The new apparatus subsystems will consist of: (1) a pivoting drive mechanism with variable speed and oscillation angle, (2) specimen fixtures, (3) a frictional torque sensing system, and (4) a furnace and fixture cooling system. Bearings and other drive system parts have been ordered, and others were drafted and sent out for machining. A variable speed, feedback-controlled motor-generator set has been obtained. Initial design strategies will be discussed with Cummins Engine Company.

Future Plans

a) An article that summarizes the friction and wear test results for stainless steel Type 316 sliding on NT-451 and a the silicon nitride-based composite, will be submitted to a technical journal within the next month. It was co-authored by B. Dumont, P. Blau, and G. Crosbie, Ford Motor Company,

b) Design work for the high-temperature, oscillatory scuffing rig will continue, with the coordination of Cummins Engine Company.

c) P. Blau and B. Dumont, ORNL, will present papers at the 1999 International Conference on Wear of Materials to be held April 25-29 in Atlanta. Blau's paper, co-authored with K. Budinski of Eastman Kodak Company, will be on the use of ASTM standard test methods to solve industrial wear problems, and Dumont's paper, co-authored with both ORNL and Caterpillar researchers, will discuss the wear mechanisms of ceramic valve guide materials.

Status of Milestones

On schedule

Communications/Visitors/Travel

None

Problems Encountered

None

Publications and Presentations

One in preparation

Development of an "Intelligent Grinding Wheel" for In-Process Monitoring of Ceramic Grinding

S. Malkin, R. Gao, C. Guo, B. Varghese, and S. Pathare
Department of Mechanical and Industrial Engineering
University of Massachusetts
Amherst, MA 01003-2210

U. S. Department of Energy
Identification Number : DE-FG05-96OR22524

Introduction

This is the fifth semi-annual report for the project "Development of an Intelligent Grinding Wheel for In-Process Monitoring of Ceramic Grinding." This report covers the period from September 1, 1998 to February 28, 1999.

The overall objective of this project is to develop sensor-integrated "intelligent" diamond wheels for the on-line monitoring of ceramic grinding. Such wheels will be "smart" enough to monitor and supervise both the wheel preparation and grinding processes without the need to instrument the machine tool. The intelligent wheels will utilize re-useable cores integrated with sensors to measure acoustic emission (AE) and grinding force. Signals from the sensors will be transmitted from the rotating wheels to a stationary receiver by telemetry. Wheels will be "trained" to recognize distinct characteristics associated with truing, dressing and grinding.

Technical Progress

This overall project is divided into six tasks as follows:

1. Development of miniaturized sensors and data transmission system,
2. Wheel design and sensor configuration,
3. Calibration of the sensor integrated wheel,
4. Training of the intelligent wheel,
5. Grinding tests,
6. Prototype demonstration.

The technical progress summarized in this report is concerned with tasks 3 and 5.

System Integration & Programming

The intelligent grinding wheel system consists of a grinding wheel core that is integrated with multiple AE and force sensors and an adapter disk that contains a miniaturized telemetric data acquisition module (DAQ). It is also equipped with a stationary telemetric data receiver that is connected to a desktop computer. The DAQ is made up of several sub-systems including a charge amplifier, a multiplexer, an anti-aliasing filter, an Analog-to-Digital Converter (ADC), a Digital Signal Processor (DSP), and an RF transmitter interface. The design and development of the individual components were described in the previous reports. This section focuses on the integration and programming of this complex system.

As shown in Figure 1, the DAQ is housed in an adapter disk along with the RF transmitter and power supply. When the adapter disk is fastened to the grinding wheel core, connectors mounted on the adapter disk make electrical contact between the sensors embedded in the grinding wheel and the DAQ in the adapter disk. A set of miniature D-type connectors further connect the DAQ to the RF transmitter. Two J-type batteries, wired in series, are used to power the DAQ and RF transmitter during operation.

The adapter disk has several design features that facilitate efficient operation. These include a plug-in pod for program transfer, flexible jumper settings for power supply selection, and hardware reset. The 14-pin plug-in pod provides a convenient way to upload application-specific programs developed on a host computer on to the on-chip memory of the Digital Signal Processor (DSP). These programs include routines for

sensor and RF transmitter initialization, sub-system control, signal processing, and data transmission. The two batteries power the electronics during grinding operation. In the current circuit design, the batteries are able to provide continuous service of up to three hours, after which they need to be replaced to ensure reliable system operation. For preparatory operations, such as program uploading or debugging, an external 6V DC supply can be used to preserve battery life. Switching between the battery and external power is achieved by shorting appropriate jumpers on the adapter disk. By means of a reset button, the DSP can be reset when an anomalous situation occurs that requires a fresh system boot up.

The DSP functions as the "brain" of the data acquisition module. It is programmed to:

- Acquire data from all fifteen sensors in a real-time, multiplexed fashion;
- Dynamically vary the gain of the charge amplifier to enable measurement of normal grinding forces over a wide range (from 5 N to 400 N);
- Acquire data at precise sampling rates ranging from 27 Hz to 576 kHz to accommodate various wheel velocities;
- Process the acquired signal in real-time and compute the averaged normal force;
- Acquire acoustic emission signals during grinding;
- Interface with the RF Transmitter and control the transmission of data from the rotating grinding wheel at a baud rate of 4,900 bps (bits per second).

The sensor-embedded grinding wheel and the adapter disk containing telemetric data acquisition electronics are both dynamically balanced at the Norton Company and certified

to operate at a rotational speed of up to 6,000 rpm.

System Calibration

The intelligent grinding wheel was calibrated and several grinding tests were conducted. These tests and the results are discussed in the following section. An external receiver unit connected to the serial port of a host computer was used to receive data transmitted from the rotating grinding wheel. Software was developed to facilitate data reception, decoding, and automated recognition of grinding features.

The monitoring system was calibrated before it was used for the monitoring grinding processes. Specifically, the charge amplifier gain was chosen to avoid saturation of the amplifier when the wheel is subjected to grinding forces. The charge amplifier gain can be selected by using different feedback capacitors. The effective feedback capacitance C is determined as:

$$C = (C_{45} + C_{46})\,(C_{41}+C_{44}+R*C_{36}+Q*C_{35}+P*C_{34})/C_{41} \qquad (1)$$

where C_{XX} are capacitors in the charge amplifier input circuit and R, Q and P are binary signals (either 0 or 1). This arrangement facilitates the selection of one among four possible capacitance values C for a given set of capacitor values. For calibration, it is necessary to select the capacitors to provide sufficient attenuation for measuring the normal force over a wide range (5 N to 400 N). One way to find the optimal capacitor value was to apply a controlled load (e.g., by means of an Instron material testing machine) on the sensor-integrated grinding wheel together with the data acquisition electronics. However, the charge amplifier has a lower cut-off frequency of 400 Hz, which

is far beyond the capability of the Instron machine. This difficulty was overcome by using the sensor-integrated grinding wheel along with a Kistler charge amplifier having a known feedback capacitor value. The wheel was then subjected to a varying load and the sensor output conditioned by a charge amplifier. In this case, the effective capacitance during grinding, C, can be determined by using the relationship:

$$V_{kistler}\, C_{kistler} = V_{grind}\, C \qquad (2)$$

where $V_{kistler}$ is the voltage output from the Kistler charge amplifier and $C_{kistler}$ is the amplifier's feedback capacitance which was set to 2 nF. The maximum voltage that can be handled by the DAQ, V_{grind}, is 3.5V. The sensor integrated grinding wheel was mounted on the Instron machine and the sensors were wired to the Kistler charge amplifier. The sensor output was amplified and converted to a voltage signal by the charge amplifier, which was logged on a computer. The effective capacitance C required during grinding was determined using Equation 2.

Grinding Tests

Several realistic grinding tests were conducted to experimentally investigate the functionality of the sensor-integrated grinding wheel. Force data were taken each time when a wheel-embedded sensor passes through the grinding zone. The data-sampling rate was varied over a wide range to investigate its effect on the acquired data. Silicon nitride workpiece of length 75 mm, was used as the grinding material. The maximum wheel peripheral velocity was 20 m/s (1075 rpm). The results are shown in Figure 2. Each data acquisition operation was initiated when the sensor output exceeded a threshold level. This corresponds to the passage of the sensor through the grinding zone. The data

acquired was transmitted (without any processing) by means of the RF transmitter. The initial data received by the receiver contains substantial noise due to the extreme environmental condition of the system (metallic shielding of the wheel system, rotating transmitter, and remote receiver). However, the system was able to retrieve the true normal force profile from the initial signal by using the filter. At low sampling rates the triggering occurred well after the peak was reached. This situation was remedied by sampling at a higher frequency as shown in Figure 2. For monitoring the normal force, the gain of the charge amplifier was set to provide high signal attenuation. This filtered out any acoustic signal that may overwhelm the circuitry, resulting in the smooth force profile shown in Figure 2.

Grinding tests were also conducted with an out-of-round wheel deliberately mounted off center in order to test the ability of the embedded electronics to detect this situation. Figure 3 shows a time history of sensor outputs during three successive passes. Only two of the eleven sensors (sensor # 2 and sensor # 3) responded, indicating that the wheel was not in full contact with the workpiece. Since the wheel did not run true, only about one-sixth of the wheel periphery made contact with the workpiece during grinding. As the wheel rounds up, more sensors will respond, indicating an increasing portion of the wheel being in contact. Finally a stable output can be obtained from all eleven sensors indicating a wheel that is running true. Therefore, the time history of sensor response can serve as an effective indicator of the wheel's out-of-roundness.

Grinding tests were conducted at various depths of cut to determine the relationship

between normal grinding force and signal output of the embedded monitoring system. To verify the reliability of the embedded wireless system, an identical but wired system was built that utilizes a Kistler dynamometer placed under the workpiece fixture. Both the wired and wireless systems were used during the grinding tests and their respective outputs were compared. The grinding tests were conducted at a wheel peripheral velocity of 20 m/s and feed rate of 2 mm/s. With these conditions, the sensor passes through the grinding zone at a frequency of 3.15 kHz. Therefore, the wheel-embedded wireless system was programmed to sample data as a sensor pass through the grinding zone at 206 kHz, which did not violate the Nyquist criteria. The DSP's computing power was used to compute the average normal force from the large amount of data sampled. After 11 successive acquisition and computation, the processed data were transmitted to the external receiver. Data was transmitted in the form of packets that contained ten repetitions of the same data point in order to minimize the influence of transmission errors. Data transmission typically took about one second. Since each grinding pass lasted approximately 30 seconds, the wired system was set up to continually sample normal forces during grinding at a low sampling rate of 20 Hz. The results are presented in Figure 4. The wired system was calibrated to give normal force in units of Newtons, while the output from the wireless wheel system was in terms of voltage. It is apparent that the wireless system was able to faithfully detect the normal force data as the wired system did. For the next reporting period, a large number of systematic tests have been planned in order to calibrate the wheel-embedded wireless system to monitor the normal force in Newtons.

Tests were also conducted to verify the acoustic emission signal acquisition. For this purpose, the grinding wheel was placed on top of a metal sheet. The metal sheet was ground using a hand held grinding tool. Acoustic waves generated during grinding were transmitted to the wheel due to the firm contact between the metal sheet and the wheel. The acoustic signal was sampled at 576 kHz by the wheel-embedded system. The result of one such test is shown in Figure 5. It is clear that the grinding wheel can respond and effectively collected acoustic signals. Further tests are planned to collect the acoustic signals during actual grinding.

Trips and Meetings

B. Varghese and C. Guo visited Norton Company on November 8, 1998 to statically balance the sensor integrated grinding wheel together with the adapter disk. B. Varghese also visited Norton Company on February 17, 1999 and March 18, 1999 to replace two damaged abrasive segments on the grinding wheel.

Personnel

- Stephen Malkin, Sc.D., Distinguished Professor, Principal Investigator

  Overall project management, grinding test and analysis.

- Robert Gao, Ph.D., Assistant Professor, Co-Principal Investigator

  Design of miniaturized sensors, telemetry, and microelectronics; testing, and prototype demonstration.

- Changsheng Guo, Ph.D., Senior Research Fellow, Co-Principal Investigator

  Mechanical design, setup, testing and prototyping of grinding wheel.

- Biju Varghese, Graduate Research Assistant, Ph.D. Student

  Mechanical design, system integration, calibration, training and testing of the grinding wheel prototype

- Sumukh Pathare, Graduate Research Assistant, M.S. Student

  Sensor development, electronic circuits design, implementation, and testing

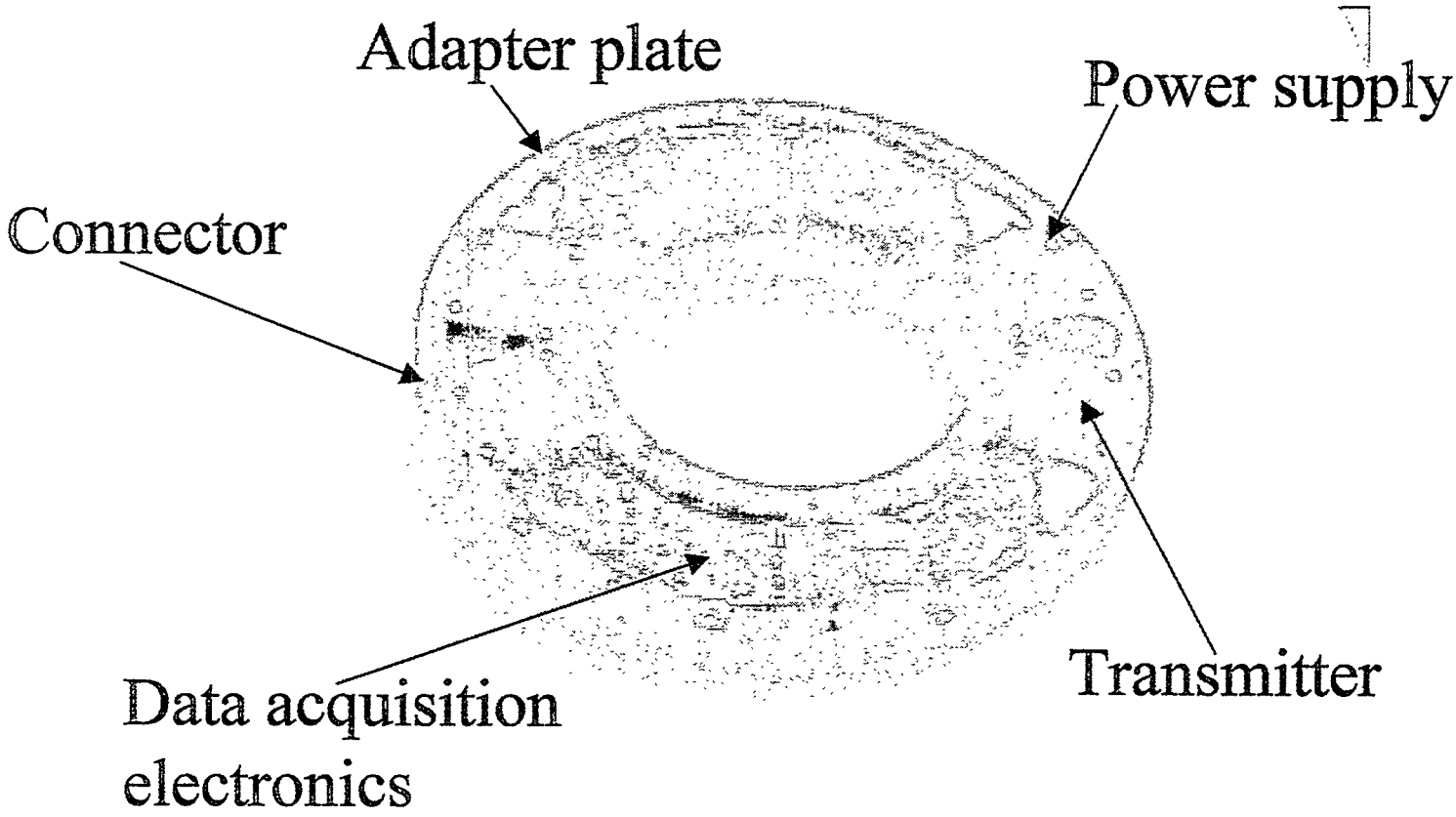

Figure 1 Adapter disk with electronics

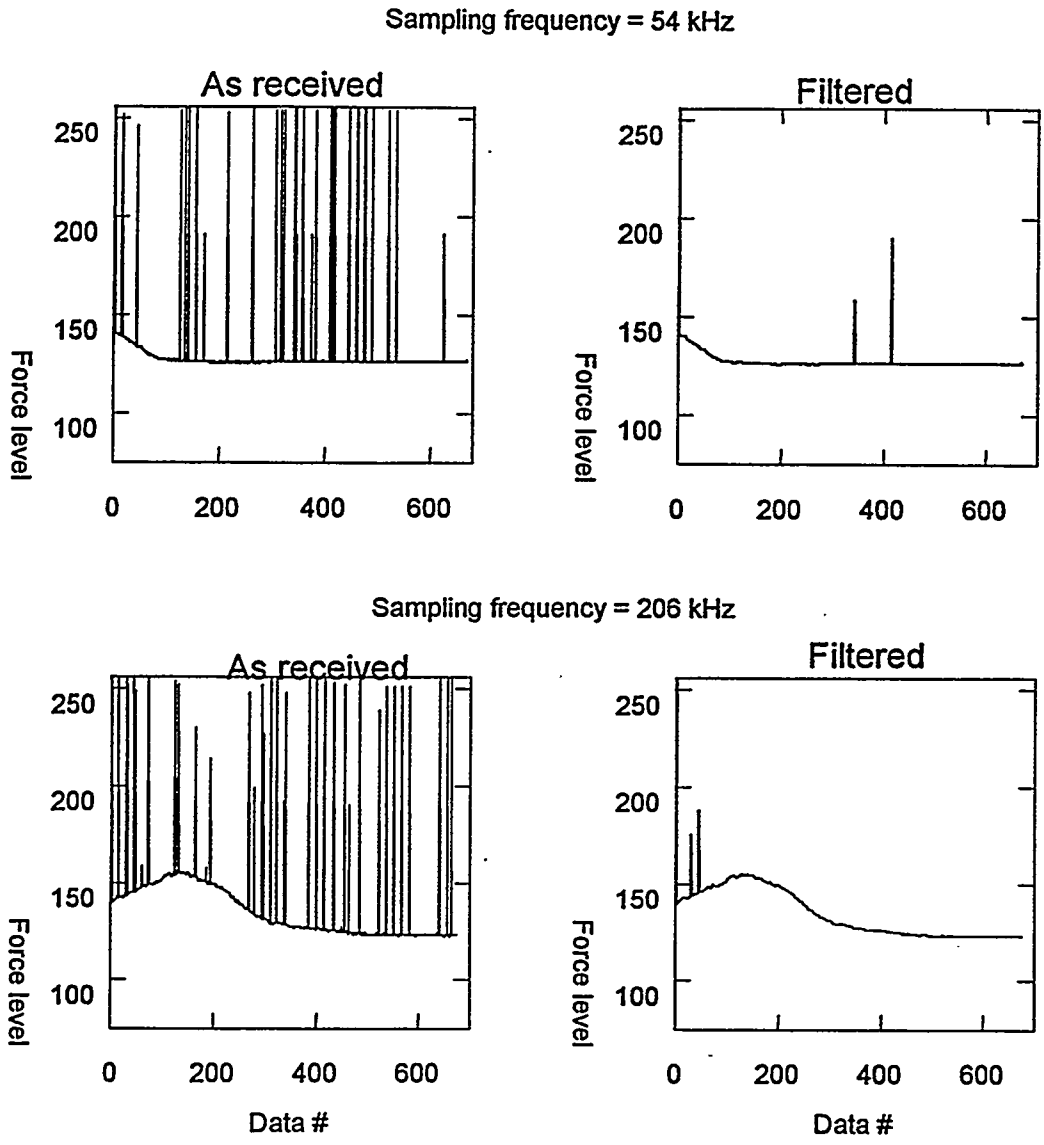

Figure 2 Force profile as one sensor passes through the grinding zone

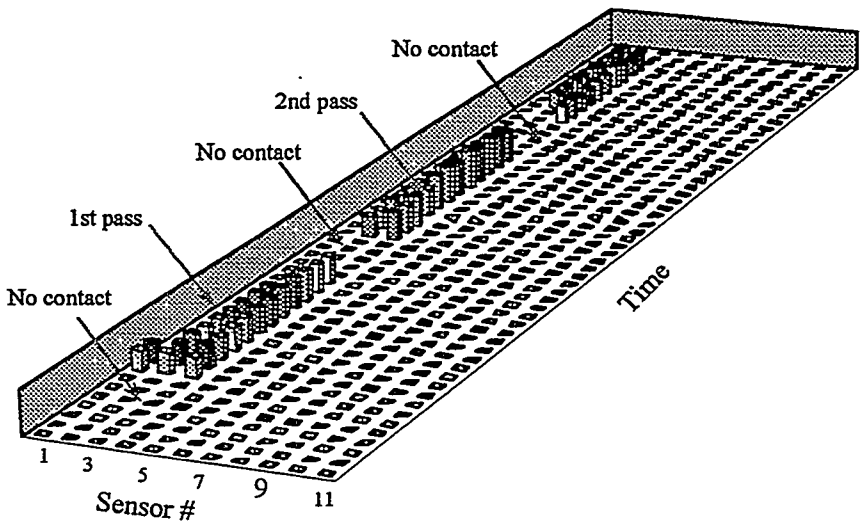

Figure 3 Sensor output versus time

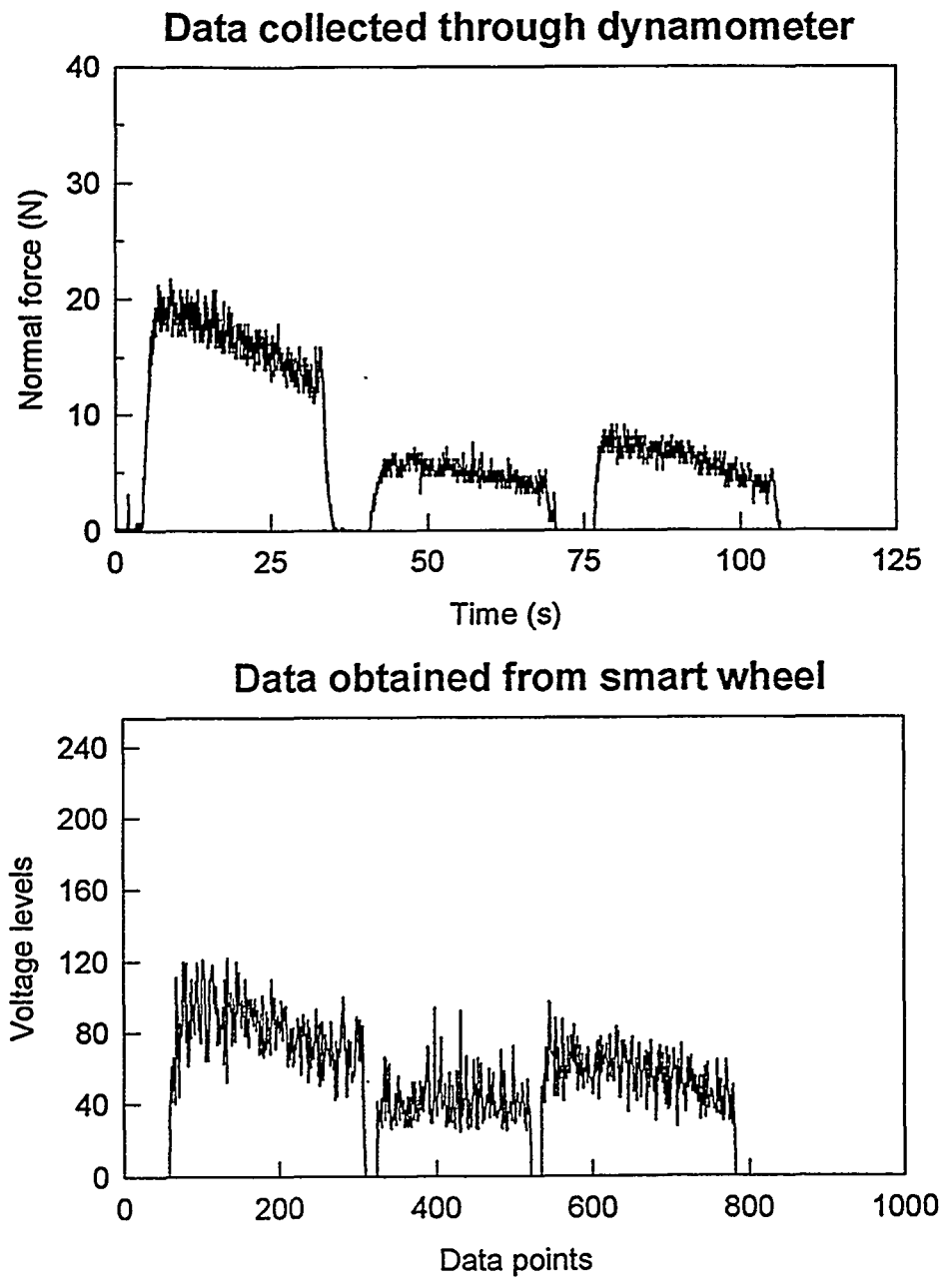

Figure 4 Comparison of wired system and smart wheel data

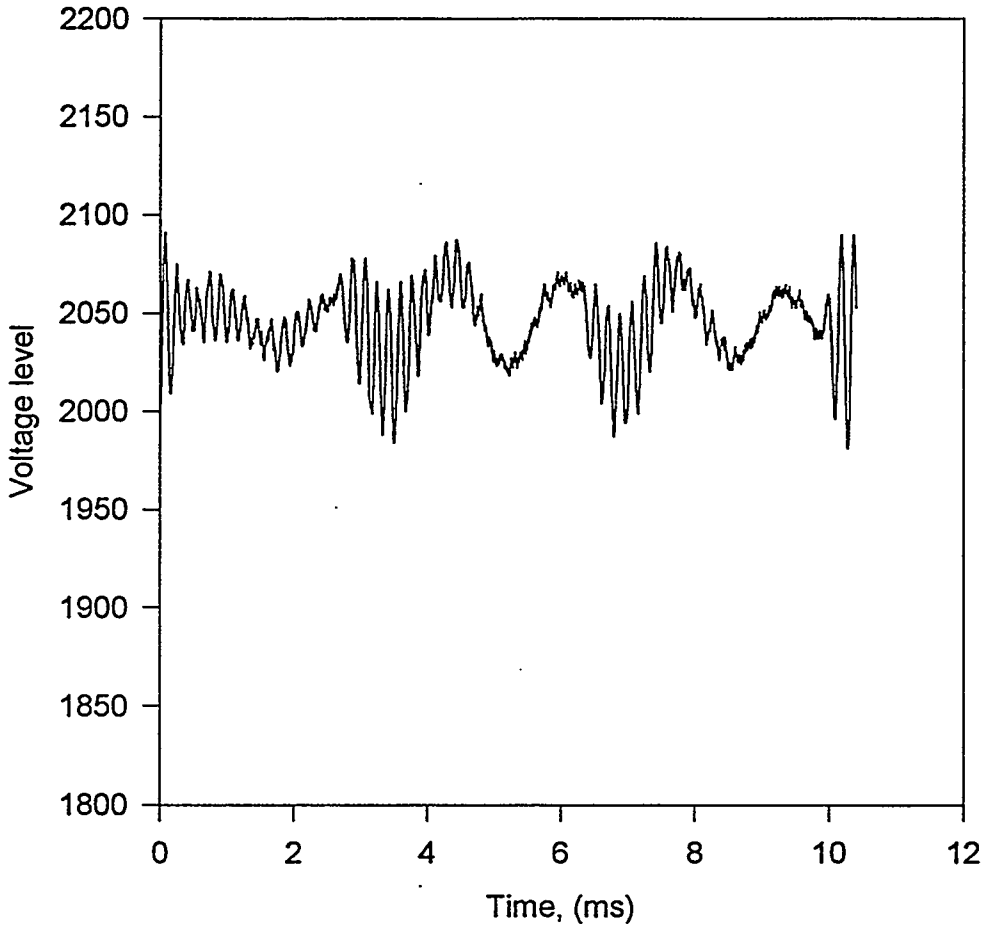

Figure 5 Acoustic emission signal acquired by the wheel during static testing

Laser Scatter Methods for Detecting Subsurface Machining Damage in Ceramics – Jiangang Sun, William A. Ellingson, (Argonne National Laboratory), Michael C. Long, Michael H. Haselkorn, and Charles J. Anderson (Caterpillar Inc.)

Objective/scope

The primary objective of this program is to develop a laser-based elastic optical scattering procedure which would provide a direct (near real-time) method to detect machining induced damage in monolithic ceramics. Median and lateral crack detection are of primary importance. The laser-based elastic optical scattering program is being executed in three steps. The first step is to optimize the elastic scattering procedure by examining specimens machined using innovative machining techniques. The second step involves correlation of the elastic scattering results with mechanical properties in "real" machined ceramic specimens. The final step involves the development of a prototype instrument to be evaluated for on-line implementation in a production environment.

Technical progress

1. Elastic Optical Scattering Results

Work during this period focused on improving data acquisition speed of the elastic optical scattering system and on acquiring and analyzing laser scattering data for a new set of machined specimens.

We received a new set of 34 diamond-ground Ceralloy and GS44 specimens from Caterpillar, Inc. The machining conditions of these specimens are listed in Table 1. The 20 Ceralloy specimens were machined with 10 conditions and the 14 GS44 specimens with 7

Table 1. Machining conditions of new diamond-ground specimens

Test No.	Wheel Specification	Run	Material	MRR
1	Resin/150Grit /150Conc./Friable	1/2	Ceralloy	Low
2	Resin/150Grit /150Conc./Friable	1/2	Ceralloy	High
		1/2	GS44	High
3	Resin/100Grit /150Conc./Friable	1/2	Ceralloy	High
4	Vitreous/150Grit /150Conc./Friable	1/2	Ceralloy	High
		1/2	GS44	High
5	Vitreous/150Grit /150Conc./Friable	1/2	Ceralloy	Low
		1/2	GS44	Low
6	Vitreous/150Grit /150Conc./Non-friable	1/2	Ceralloy	High
		1/2	GS44	High
7	Vitreous/100Grit /150Conc./Non-friable	1/2	Ceralloy	Low
		1/2	GS44	Low
8	Vitreous/100Grit /150Conc./Non-friable	1/2	Ceralloy	High
		1/2	GS44	High
9	Vitreous/150Grit /100Conc./Friable	1/2	Ceralloy	High
		1/2	GS44	High
10	Vitreous/100Grit /100Conc./Friable	1/2	Ceralloy	Low

conditions, with two specimens at each condition. The machining variables include: resin of vitreous bond diamond wheels, grit number, grit concentration, friable or non-friable grit, and low or high material removal rate (MRR). Each specimen has a machined surface area of 45 mm x 45 mm and a thickness of ~3 mm.

Laser scattering measurements were conducted only on a 20 mm stripe at the center of each specimen with two overlapping scans (25-mm x 20-mm areas), as illustrated in Fig. 1. Each scan contains 2500 x 2000 pixels at 10 μm steps. Using the LabView program at a maximum speed of 75 Hz, the data acquisition for each specimen needs ~37 hours, which is too long. Therefore, a new data acquisition program written in C language was developed. This program continuously acquires optical data while the specimen is translated continuously by a stage, in contrast with a step-by-step measurement by the LabView program. As a result, the speed of the new program reaches about 830 Hz, and the data acquisition time for each specimen becomes ~3.4 hours. This program was used to obtain scatter data for all 34 specimens as listed in Table 1.

Figure 2 shows laser scattering ratio and sum images on two overlapping 25-mm x 20-mm regions at 10-μm resolution for the GS44 specimen 2.1, identified as Test No. 2 and Run 1 as listed in Table 1. Figure 3 shows detailed scatter images from Fig. 2. These images show typical characteristics of defects and machining damage on the ground surface that can be detected by laser scattering, i.e., distributed defect/damage spots and parallel machining damage lines which show brighter in the sum images and darker in ratio images.

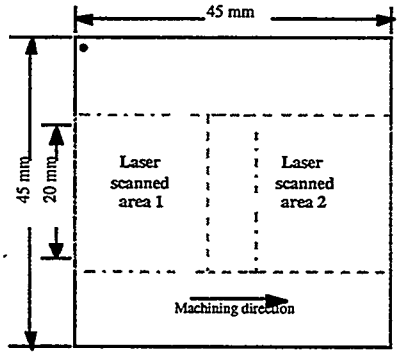

Figure 1. Diagram of a diamond-ground specimen from Caterpillar and the laser scanned areas on the specimen surface.

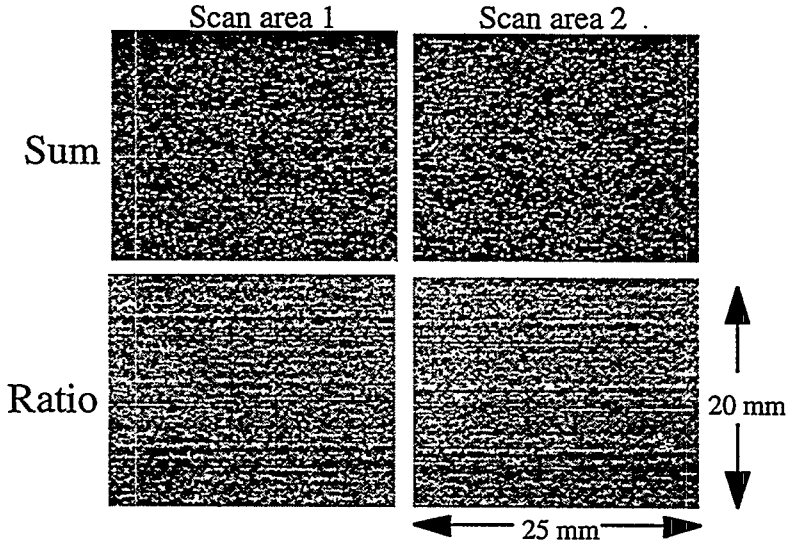

Figure 2. Elastic optical scattering sum and ratio images of the ground surface of diamond-ground GS44 specimen 2.1.

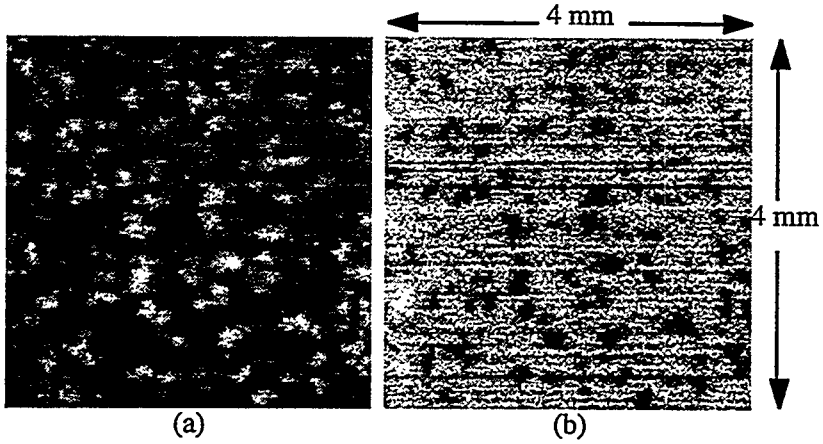

Figure 3. Detailed elastic optical scattering (a) sum and (b) ratio images from near the lower-right corner of the scan area 1 images in Fig. 2.

Figure 4 shows laser scattering ratio and sum images on two overlapping 25-mm x 20-mm regions at 10-μm resolution for the Ceralloy specimen 5.2, identified as Test 5 and Run 2. These images also show typical characteristics of defects and machining damage on the ground surface. However, some laser scatter images of Ceralloy specimens show features indicating variations in the material structures within a specimen or distinct machining patterns between the two specimens of same machining condition. Figure 5 shows laser scatter data for Ceralloy specimens 4.1 and 4.2, the machining patterns are apparently different between the two specimens. The white circular region at the center of specimen 4.2 may be the result of differing material structure. In addition, some laser scatter images (for both Ceralloy and GS44 specimens) show gross gray-scale variation from one side to the other (see ratio images in Figs. 2, 4, and 5).

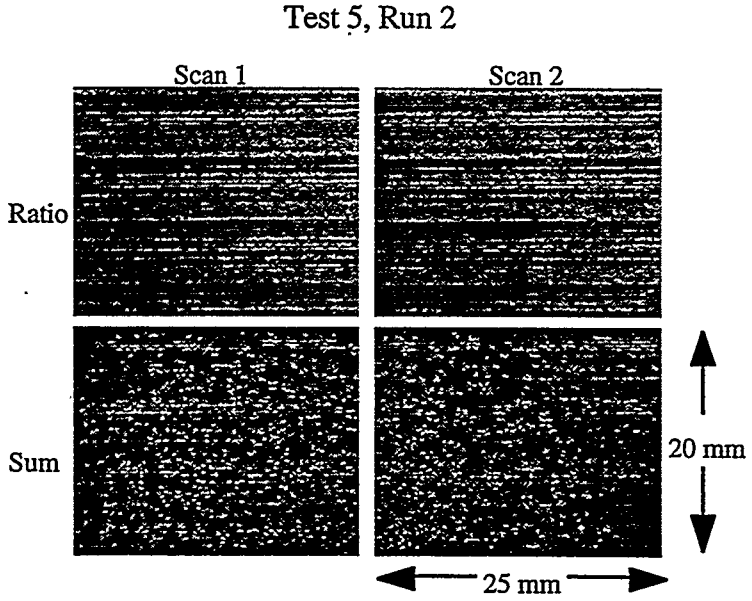

Figure 4. Elastic optical scattering sum and ratio images of the diamond-ground surface of Ceralloy specimen 5.2 (Test 5, Run 2).

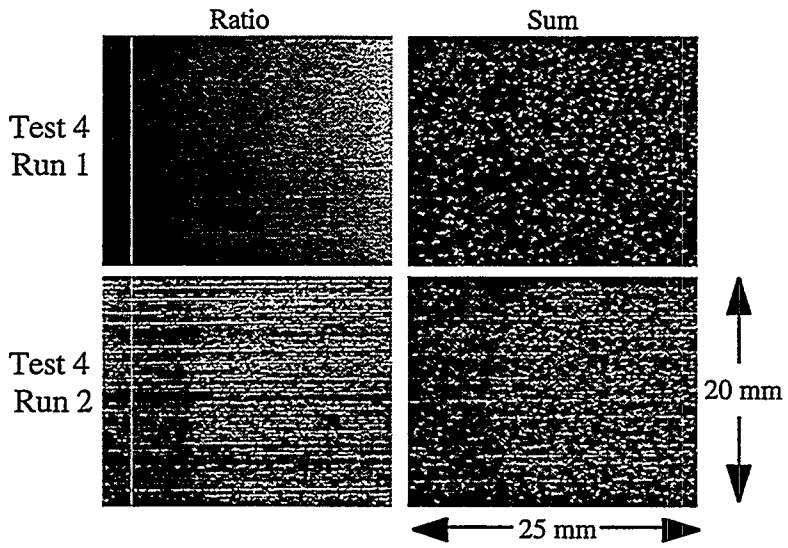

Figure 5. Elastic optical scattering sum and ratio images of the diamond-ground surface of Ceralloy specimens 4.1 and 4.2 (Test 4, Runs 1 and 2).

We have calculated statistical variables, including mean, standard deviation, and skewness, from the histograms of the laser scattering sum images for all Ceralloy and GS44 specimens. However, because of large variations of the laser scattering data showing in each scanned areas (25-mm x 20-mm in size), some of the statistical values showed considerable scattering in the two scanned images from the same specimen or from the two specimens of the same machining condition. To reduce the data scattering, we derived a new data processing method. We first divided the original image into smaller sections, then calculated the statistical variables for each section, and finally averaged the results from all sections to obtain the statistical data of the entire image. Two partition sizes were used to divide the original images: (1) 500 x 500-pixel sections as shown in Fig. 6 and (2) 250 x 250-pixel sections. It was found that the difference between the statistical values calculated from the 500 x-500-pixel and the 250 x 250-pixel sections are typically <1%, while the difference may be >20% when compared with the values calculated from the entire 2500 x 2000-pixel image. Therefore, statistical values calculated from the 500 x-500-pixel and the 250 x 250-pixel sections are considered representative of the measured data and are presented below.

Two nondimensional statistical parameters, the coefficient of variance C_v (= standard deviation / mean) and the coefficient of skewness C_s (= skewness / mean), and their ratio C_s/C_v were studied. Figure 7 shows C_v, C_s, and C_s/C_v vs. the test no. for the GS44 specimens. The ranges of data scatterings are indicated as vertical bars around the mean values. It is seen that there are considerable data variations for some specimens, due mainly to the differences of the two specimens (or two runs) in each test condition (see Table 1). In general, the trends of C_v and C_s to the test no. (Figs. 7a-b) are similar. The trend of C_s/C_v (Fig. 7c) to the test no. is opposite to those of C_v and C_s. In Fig. 8, the statistical parameters C_v, C_s, and C_s/C_v are plotted for the Ceralloy specimens. However, by comparing Figs. 7 and 8, we were not able to find consistent correlations for both sets of specimens. The reason for this difficulty may be partially elucidated from the laser scattering images as those shown in Figs. 2-6. For GS44 specimens the material defects (the brighter spots which had been identified as regions of high porosities) are much more prominent than machining damage (brighter lines), while for Ceralloy specimens there are large-scale variations of material structure on the surface.

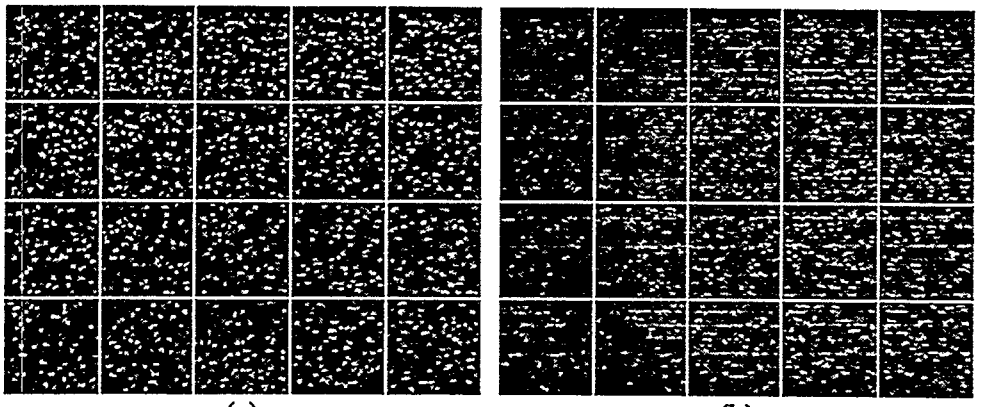

(a) (b)

Figure 6. Partitions of elastic optical scattering sum images into 500-pixel x 500-pixel sections for calculation of statistical parameters: (a) GS44 specimen Test 4, Run 2 and (b) Ceralloy specimen Test 4, Run 2.

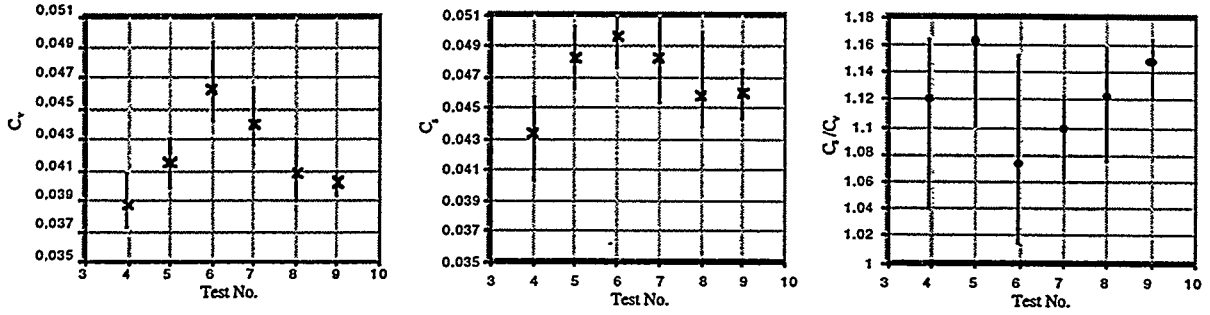

(a) (b) (c)

Figure 7. Plots of statistical data (a) C_v, (b) C_s, and (c) C_s/C_v vs. test no. for GS44 specimens.

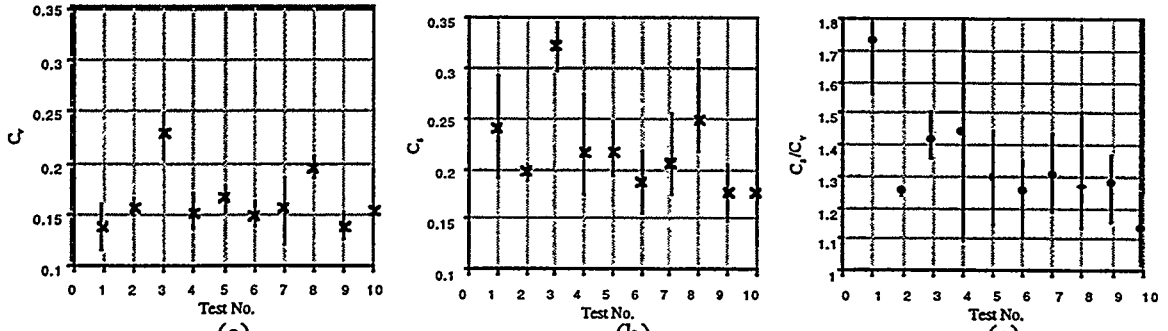

(a) (b) (c)

Figure 8. Plots of statistical data (a) C_v, (b) C_s, and (c) C_s/C_v, vs. test no. for Ceralloy specimens.

2. Calibration of New Tunable Laser

A new continuous-wave (CW) Ti:sapphire tunable laser was acquired and setup. It has a tunable wavelength from 700 to 1000 nm, i.e., from red to infrared light (the wavelength of He-Ne laser is 632.8 nm). It was supplied with two optics sets, the first allows tuning between 700 and 850 nm and the second between 850 and 1000 nm. Currently, the first optics set has been

installed. A calibration of the output wavelength with an older model monochromator is shown in Fig. 9. Although the measured data do not match with the manufacturer's data, the figure shows that the laser can be tuned in the range of 700 and 850 nm. More accurate calibration data will be determined when a new monochromator is acquired. This laser will be used to study optical transmission and scattering properties of Si_3N_4 ceramics as a function of wavelength.

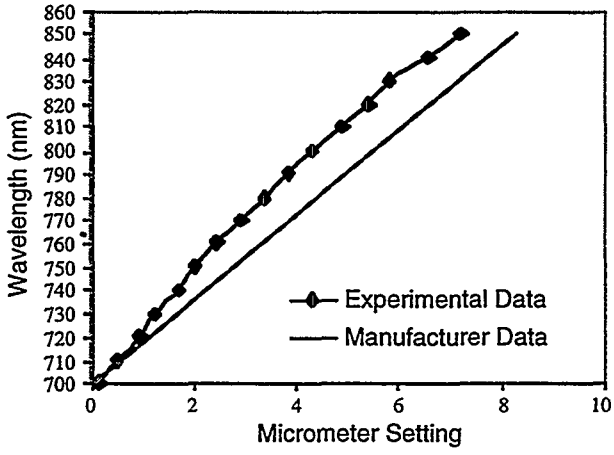

Figure 9. Wavelength calibration chart for the CW Ti:sapphire laser.

2. Automation for On-Line Inspection with Optical Scattering

We did not devote any effort to this part of the project this period because we have been working to establish correlations. However, the improvement in data acquisition speed with the new data acquisition program will enable us to obtain real-time data for on-line inspections.

3. Impact Acoustic Resonance

We have received the single point laser vibrometer and have successfully acquired test data for validation purposes. The frame structure previously designed and fabricated has been assembled and the vibrometer mounted to the transitional stages. A schematic diagram of the system is shown in Fig. 10 along with a photograph of the system setup in Fig. 11. The STAR Acoustic modal analysis software package has been installed and has been tested using a ceramic "square" specimen with a slight spherical curvature. The first couple of mode shapes have been calculated and are shown Fig. 12. The two mode shapes correspond to resonant frequencies of 1.93 and 2.80 kHz respectively.

Current issues involve better coordinating the motion of the laser head with the data acquisition routines. Also, a near-realtime calculation of signal coherence needs to be integrated to the data acquisition system in order to improve mode shape accuracy.

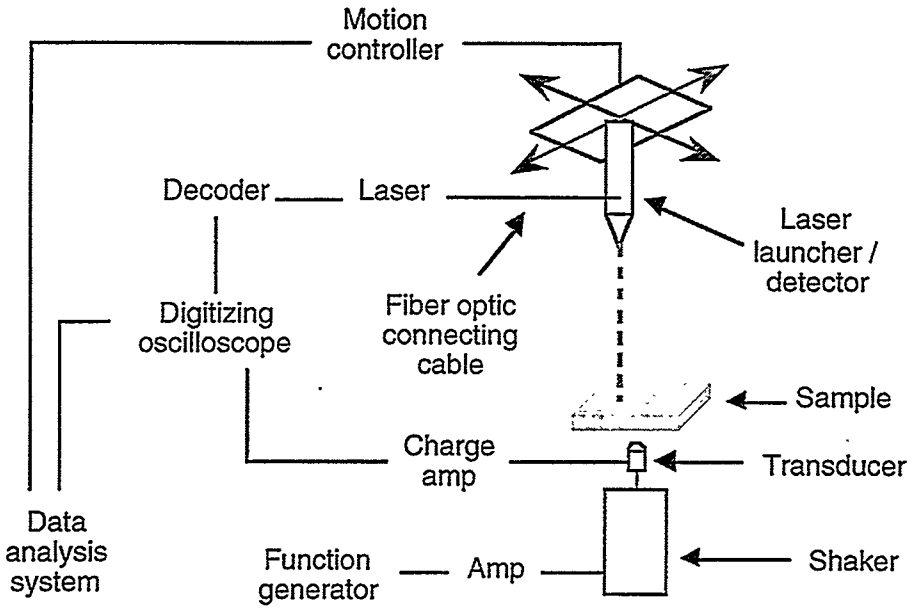

Figure 10. Schematic diagram of laser vibrometer setup.

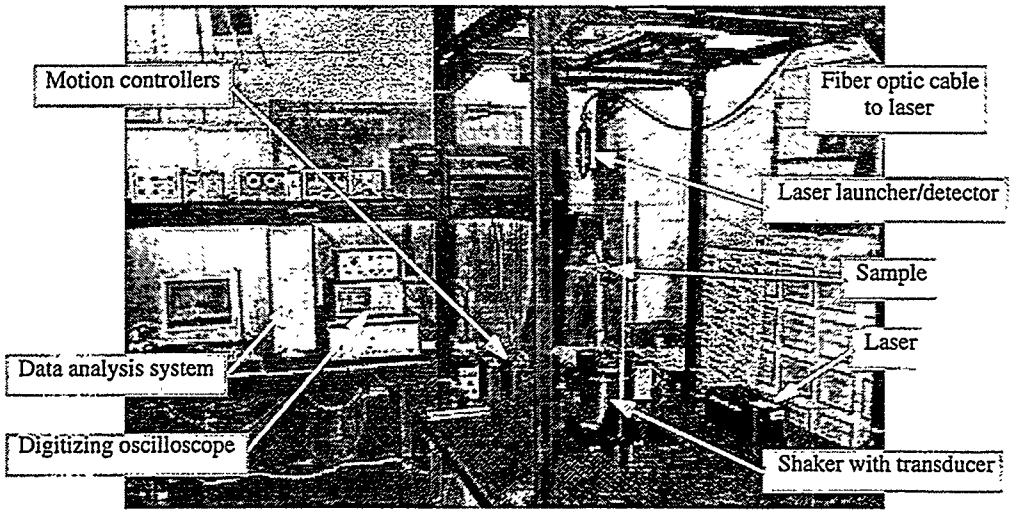

Figure 11. Photograph of laser vibrometer setup.

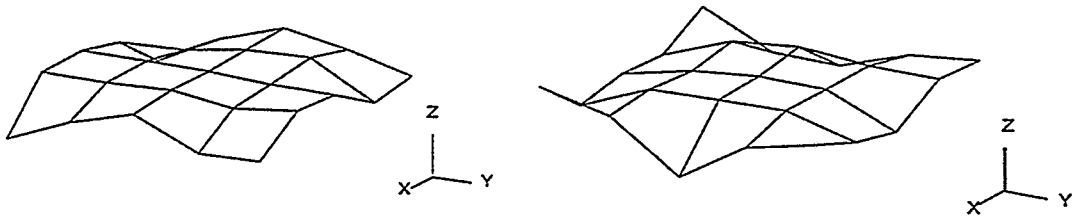

Figure 12. First two mode shapes of a ceramic "square" test sample.

Status of Milestones

Current ANL milestones are on or ahead of schedule.

Communications/Visits/Travel

Travel:

1. W. A. Ellingson visited AlliedSignal Ceramics in Torrance, CA on Oct. 5, 1998.
2. W. A. Ellingson and J. G. Sun visited Solar Turbines in San Diego, CA on Oct. 6, 1998.
3. W. A. Ellingson visited Oak Ridge on Dec. 17, 1998.
4. W. A. Ellingson and J. G. Sun attended the Annual Cocoa Beach meeting at Cocoa Beach, FL, in Jan. 25-29, 1999.

Communication:

1. Discussions have been taking place with Eaton Corporation and St. Gobain Industrial Ceramics to obtain additional machined specimens with carefully controlled machining conditions.

Problems Encountered

None this period.

Publications

None this period.

Milestone Schedule

FY 99

Obtain initial valve specimens.	2/30/99	Re-scheduled
Prepare step-wedge samples and complete optical property measurement.	4/30/99	
Obtain samples of machined round valve and flat graded-ceramic specimens.	6/15/99	
Complete initial elastic optical scatter data acquisition on specimens.	8/15/99	
Complete initial correlation of optical data with microstructure, surface roughness, IAR data, and/or dye penetrant data.	9/30/99	
Obtain complete sets of valve specimens with standard machining conditions.	9/30/99	

FY2000

Submit report and write technical paper on initial findings.	10/15/99
Complete elastic optical scatter and IAR data acquisition on the standard specimen sets.	4/15/2000
Complete microstructural analysis.	7/15/2000
Submit technical paper.	9/15/2000

FY2001

Obtain mechanical properties and correlate with NDE data.	11/30/2000
Complete and test set up of initial high speed elastic optical scatter data acquisition system on grinding machine.	12/30/2000
Submit project report.	1/15/2001

INTERMETALLIC-BONDED CERMETS

P. F. Becher and C. G. Westmoreland
Oak Ridge National Laboratory
Oak Ridge, TN 37831-6068

Objective /Scope

The goal of this task is to develop materials for diesel engine applications, specifically for fuel delivery systems and wear components (e.g., valve seats and turbocharger components). This will require materials with a minimum hardness of 11 GPa and a thermal expansion coefficient of between 10 to 15 x 10^{-6}/°C over the temperature range of 25° to 300° C. The material should also have excellent corrosion resistance in a diesel engine environment, a flexure strength in excess of 700 MPa, and a fracture toughness greater than 10 MPa$\sqrt{m}$ to ensure long term reliability. The material should also be compatible with and not cause excessive wear of the steel counter face. The upper temperature limit for fuel delivery systems applications is 540° C, and for the other wear applications, the limit is 815° C. Finally, the total material processing costs for these advanced materials should be competitive with competing technologies such as TiN or other ceramic coatings on high speed tool steels.

Technical Highlights

To date, cermet samples consisting of TiC with Ni_3Al binder phase levels of up to 40 vol. % have been provided to Cummins to evaluate scuffing and wear response of the cermets and the metallic counter face materials, Table I. The most recent cermet samples were prepared using a commercial Ni_3Al alloy (IC-50) powder and submicron TiC powder (Japan New Metals, grade 007). These resultant cermets (HP series) exhibit TiC grain sizes of < 1 micron as compared to a TiC grain size of ~ 5 microns in the earlier (MIS series) cermets prepared from the coarser (~ 2 micron) TiC powder. In addition, samples of commercial cobalt-bonded tungsten carbide were also provided to them as part of their evaluation of the influence of material properties on wear behavior.

As shown in Table I, the TiC-based cermet series will allow one to evaluate the effect of both the TiC grain size and the Ni_3Al content on wear and scuffing. To date Cummins has completed tests on HP-36 and HP-30, and test results of both indicate minimal wear of the metallic counter face material and negligible wear of the cermet.

Table I. Samples for Scuff and Wear Tests by Cummins

Sample No.	Composition	Provided to Cummins for Wear Tests	Wear Test Results
Submicron TiC Cermets (made using JNM-007 TiC powder)			
HP-36	TiC-10 vol. % Ni_3Al	July 98	Two runs, both very good
HP-48	15.5 vol. %	8 Dec 98	
HP-45	16.5 vol. %	16 Nov 98	
HP-46	19 vol. %	14 Dec 98	
HP-30	25 vol. %	31 March 98	One run, very good
HP-59	40 vol. %	17 March 99	
~ 5 μm TiC Cermets (made using Kennametal K-001-767 TiC powder)			
MIS 7-30	30 vol. % IC-50	1997	1300°C/1h 98.7%TD
MIS 8-30	30 vol. % IC-50	"	1300°C/1h 98.7%TD
MIS 9-30	30 vol. % IC-50	"	1300°C/1h 98.5%TD
MIS 10-30	30 vol. % IC-50	"	1300°C/1h 98.4%TD
Cobalt Alloy-Bonded WC			
VC-12	WC-10 wt. % Co	15 Feb 99	
VC-103	WC-16 wt. % Co	15 Feb 99	
VC-14	WC-24 wt. % Co	15 Feb 99	

Our recent work has focused on improving the processing of cermets formulated with the submicron TiC powders to enhance the densification under sintering (no applied stress) conditions. Wetting of these powders by the liquid Ni_3Al is diminishes, in part due to the much smaller capillary sizes in compacted preforms employing submicron powders as compared to the earlier TiC powders having ~ 5 micron average particle sizes. From earlier studies, it appears that the stoichiometry of the TiC powders can be a factor with lower Ti: C ratios enhancing the wetting process in submicron TiC powders.

Studies continue to examine means to enhance the liquid phase densification of TiC-Ni_3Al cermets that are based on submicron TiC powders. The goal is to be able to produce cermets with a wide range of Ni_3Al contents with simple pressureless sintering process. The process to obtain dense cermets was resolved early on; however, wetting of the TiC and the retention of high Ni_3Al contents where the Ni_3Al is the liquid phase presence some difficulties for pressureless sintering processes. The first was simply to reduce the green density of the compacts in an attempt to increase the pore channel sizes. This proved of little value, the lower starting density simply required excessive shrinkage and particle rearrangement. Recent work has focused on the use of molybdenum powder additions to the TiC. The Mo tends to react with the TiC and form an external layer. This can be seen in Figure 1 where energy dispersive analysis has shown that the lighter regions (arrowed) on the TiC grains contain molybdenum. The Mo additions appear to promote wetting by the Ni_3Al and its retention as it is now possible to obtain fully dense TiC-Ni_3Al cermets containing up to 40 vol. % Ni_3Al.

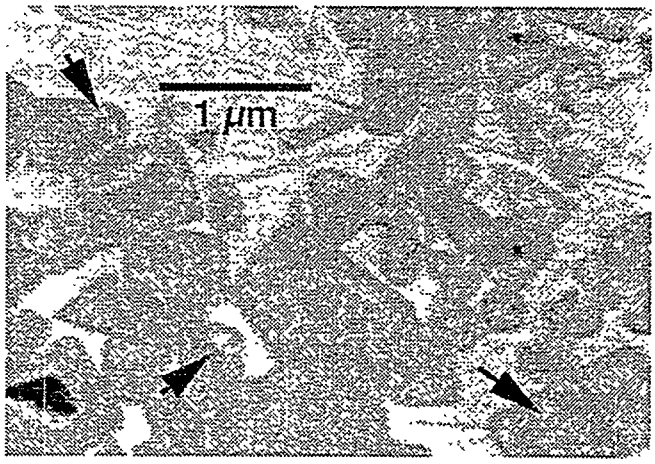

Figure 1. Dense TiC-40 vol. % Ni_3Al cermet which incorporates molybdenum addition to promote wetting by reacting with the surface of the TiC grains and forming a molybdenum rich shell (examples arrowed).

Status of Milestones
On Schedule

Communication/Visits/Travel
Review meeting was held at Cummins Engine Company (12/8/98) with personnel Kevin McNerney of Coors, Jim Stephan of Advanced Materials Technologies, Randall German and Tim Weaver of Pennsylvania State University, Paul Becher and Ray Johnson of ORNL, and Tom Yonushonis, Carl McDonald, Malcolm Naylor, Randy Stafford, and Magan Patel of Cummins Engine to discuss progress on cermet materials.

Problem Encountered
None

Publications
None

COST EFFECTIVE MACHINING OF CERAMIC ENGINE COMPONENTS

S. B. McSpadden, Jr.
T. O. Morris

Oak Ridge National Laboratory
Box 2008, Building 4515
Oak Ridge, Tennessee 37831-6069

Objective/Scope

To develop and demonstrate optimized, cost-effective grinding processes for the production of ceramic components for use in diesel engines.

Technical Highlights

High-speed Grinding on the Cincinnati Milacron Centerless Grinder

High speed centerless grinding is being investigated as a cost-effective method for producing ceramic engine components. The process is attractive because the need is eliminated for workpiece fixtures and workpiece alignment. Compared to other grinding processes, centerless grinding is fast, wheel wear rates are low (due to the large surface area of the grinding wheel), and the process produces high quality parts.

After several months of inactivity, the centerless grinder was restarted with one of two new diamond-coated work rest blades installed. Using the same settings that had been used successfully in the past, initial attempts to grind silicon nitride button-head tensile specimens at high in-feed rates were unsuccessful. Specimens appeared to fracture during the grinding process due to excessive bending, and a difference of approximately100 microns (0.004 inch) was observed between the two larger diameters at the ends of the gauging section. (The diameters should have been the same.) After extensive in-house investigation, the problem was discussed with centerless grinding experts at the Milacron Marketing Company's Abrasive Products Division. The most likely cause of the broken specimens is believed to be an intermittent slipping condition between the specimen and the regulating wheel. The regulating wheel controls the rotational speed of the workpiece during grinding, and it is important to maintain rolling contact with the workpiece. This condition is believed to have occurred because of a change in the friction coefficient when the work-rest blade was coated with diamond. New regulating wheels have been ordered to increase the friction coefficient to an acceptable value.

Using the Weldon cylindrical grinder, additional silicon nitride machining blanks have been prepared for use on the centerless grinder. We were able to "leverage" this effort through the HTML User Program. The blanks also serve as "specimens" for the Norton Company's current HTML user project. Norton submitted a user proposal in which we are jointly evaluating the

long-term performance of the Norton innovative grinding wheel (Scepter™ wheel) under real-world grinding conditions for ceramic workpiece materials. Norton is supplying high-quality grinding wheels at no cost and we are using the wheels to prepare the silicon nitride blanks. This is a final beta test of the wheel's long-term performance prior to commercialization.

Chand Kare Grindability Test System Upgraded

The grindability test system has been upgraded by the addition of a digital tachometer and a load cell, which aid in the calibration of the abrasive belt speed and applied test load, respectively. The equipment is now attached to a dedicated computer system on which a grindability database is being maintained. The database completely automates calculation of the grindability index, which was previously a tedious, manual calculation. Additional studies are under way to quantify the repeatability of this equipment and to develop a more rigorous test standard.

Upgrade of CAD/CAM Software

SurfCAM software has been purchased and installed on a graphics workstation to provide an enhanced 3-dimensional computer aided design/computer aided manufacturing (CAD/CAM) capability for the Machining and Inspection Research Group.

Communications/Visits/Travel

Sam McSpadden and Tom Morris attended a meeting at Milacron Marketing Company in Cincinnati, OH, to discuss potential areas for increased collaboration between the HTML and Milacron and to finalize details of a consignment agreement between ORNL and Milacron that permits the continued use of the centerless grinder.

Sam McSpadden and Tom Morris visited the UNOVA/Landis-Gardner facility in Hebron, KY to view the facility where centerless grinders are manufactured and assembled. UNOVA recently completed the acquisition of Cincinnati Milacron Machine Tool Division and the GoldCrown Company – two major domestic manufacturers of centerless grinding equipment.

Sam McSpadden, Tom Morris, and Lawrence O'Rourke visited the Caterpillar Design Center in Peoria, IL to discuss the impending expansion of an existing CRADA. We also visited the production facility in Pontiac, IL, and established contact with production manufacturing personnel who will eventually be responsible for the manufacture of ceramic engine components.

Publications

Sam McSpadden presented a paper entitled *Vitreous Bond CBN High Speed and High Material Removal Rate Grinding of Ceramics* has been accepted for presentation at the 1998 Annual Meeting of the American Society for Precision Engineering in St. Louis. (Principal author was Dr. Albert Shih, formerly of Cummins Engine, and now an Associate Professor at North Carolina State University.)

TESTING AND CHARACTERIZATION

Task Title: Computed Tomography
Principle: R. Koehl, H.R. Lee, H.P. Engle,
Argonne National Laboratory

Objective/Scope

The objective of phase III has changed. The densitometry study of the chopped carbon fiber/GS-44 for Allied-Signal/Caterpillar has been completed. GS-44 material with chopped carbon fiber has been under development as a candidate material for diesel engine valve guides with reduced wear. The nondestructive evaluation approach utilized 3D x-ray computed tomographic (3D X CT) imaging technology with an emphasis on correlation of image data with destructive analysis. We continue to cooperate with Caterpillar, Inc. and Allied-Signal Ceramic Components as we move towards different objectives.

Emphasis has now shifted to Silicon Nitrides for diesel engine valves. We have also focused on the evaluation of the amorphous silicon x-ray imaging detector for improved detection sensitivity.

Technical Highlights

The technical highlights will be described in three areas: 1) a discussion of the CRADA work on the amorphous silicon detector, 2) analysis of spiral CT, and 3) the x-ray densitomtery of the GS-44/Chopped carbon fiber valve guides.

1. CRADA—
Evaluation of an Amorphous Silicon X-ray Imaging Detector

A. Development of CT scanning code

During this period, we have continued to develop the necessary software to allow evaluation of this advanced high-speed x-ray detector as a device for both projection x-ray imaging and for sequential scan x-ray computed tomography (CT). Previous code developed in LabView could not capture more than 10 sequential frames. This limitation was first extended to code that was able to grab more than 100 frames consecutively, but was not entirely error-free. There were occasional error messages indicating software time out while attempting to read or write to the buffer on the DIPIX interface. We believe that error was due to a synchronization problem

between the software driver and the LabView application software. Currently, the occasional time-out error is not significant in the single-image, projection mode.

The development of LabView Virtual Instrument Control Panels (codes or VIs) for CT scan modes is a continuing effort. Sequential projection image data can be combined into a final main program for the CT scan modes. We have developed the Labview VIs so that they can be used as a sub-VI for our main CT program. Fig. 1 is a screen image of the Labview Virtual Instrument (VI) Control panel (code) that captures and displays either an individual image or a sequence of images. This code captures and displays an individual image for sequential image acquisition, in which the number of projections is defined.

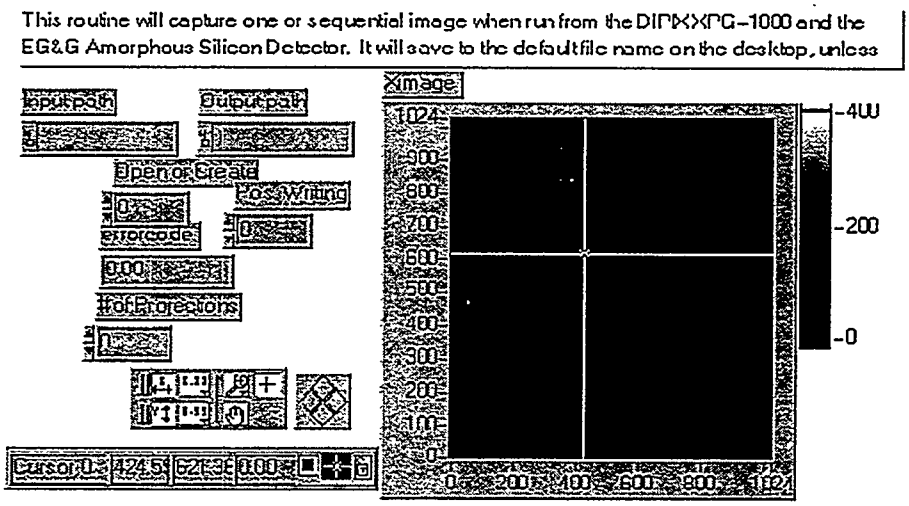

Fig. 1. Image of computer screen showing one projection image from Amorphous Silicon Detector

With an additional sub-VI that defines the region of interest for an individual frame, the code, shown in Fig. 2, is able to combine sequential frames into one data set, a CT scan file, and to display the images in that set. By adding a motion-control sub-VI to the sequential scan VI (see Fig. 3), the final CT code has the ability to capture sequential images while rotating the sample and saving the images to a CT scan file. This sub-VI controls the speed of sample rotation and the step size (i.e. the number of projections) of a scan. It includes a data-acquisition sub-VI and another sub-VI to reduce the size of an individual frame by defining the region of interest.

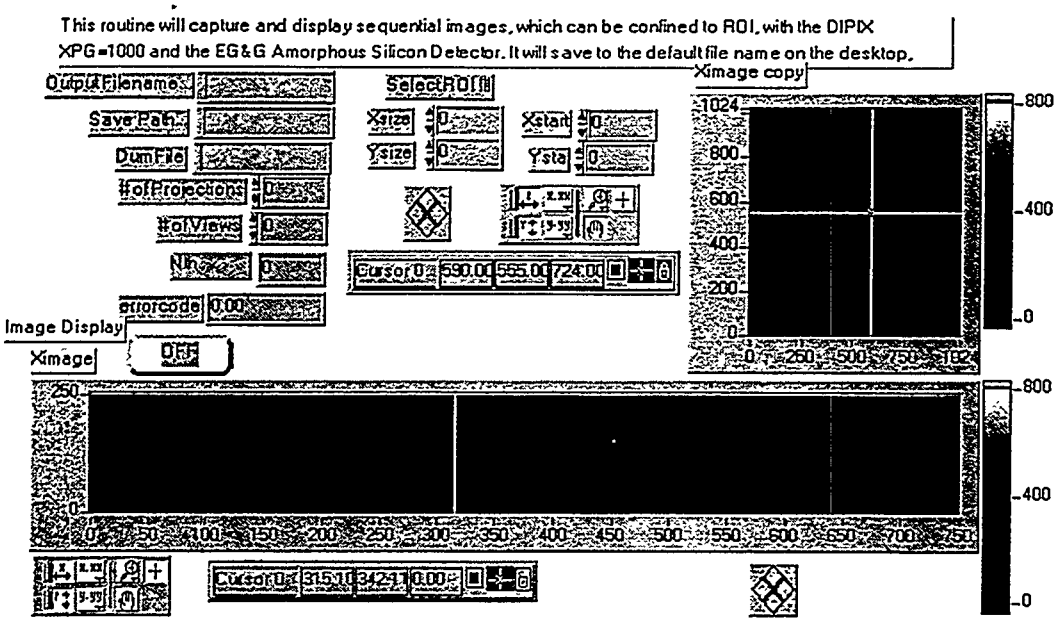

Fig. 2. Computer screen image showing the pictorial diagram of the code used for data acquisition and defining the region of interest

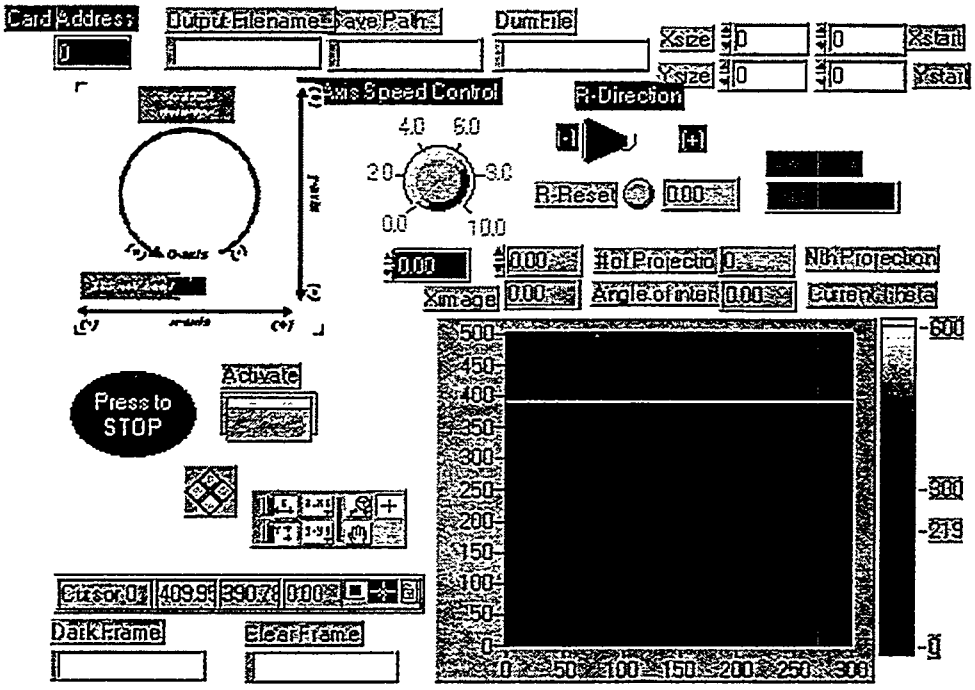

Fig. 3. Screen capture of CT control panel consisting of several sub-VIs that communicate between the motor drive control and the image acquisition code, such that rotation and translation of the stages is accomplished while image data sets are obtained and stored to disc.

October 1998 – March 1999

To complete the development, we also need to develop extra data-acquisition VIs for cone-beam applications, e.g., a grid calibration to determine the beam divergence and the center of beam, and a wire calibration to detect the center of rotation. Since the detector has defective pixels, in order to run our existing algorithm for the calibrations, it is necessary to develop a special VI that can detect the defective pixels and interpolate neighbor-averaged values on them. Further, one item of concern to us right now is the necessary long wait-state between image capture and writing to disc. Currently this takes 4-5 seconds. We need to get this down to less than 100 msec if possible.

B. CT Reconstruction

The first CT scan and reconstruction using the amorphous silicon detector has been completed. To evaluate the capability of the detector as a CT detecting device, using a parallel beam code, we used a small sample to reduce beam-divergence and avoid calibration procedures. The sample was an electric insulator made of ceramic material with a radius size of 1 cm. The sample-to-detector distance was ~100 cm, which resulted in 0.01-radian divergence. The unit pixel size of the detector is 100 x 100 _m^2, which cannot be degraded by the beam-divergence. According to a paraxial-beam approximation, since we did not have all core beam data acquisition codes, we simply used a parallel-beam reconstruction algorithm for this sample. Fig. 4-a represents a normalized projection image that shows a defective pixel line. This line causes the circular artifact in the reconstructed image shown in Fig. 4b. Figure 4-b also shows the cross-sectional shape of a slot in the sample and the hard-coated surface with a thickness of ~0.3 mm. Fig. 4-c is a 2-D reconstruction generated by slicing the 3D reconstruction. Shown in Fig. 5 is an image orthogonal to the direction to the axis of rotation; Fig. 5 is the surface rendering image of the sample.

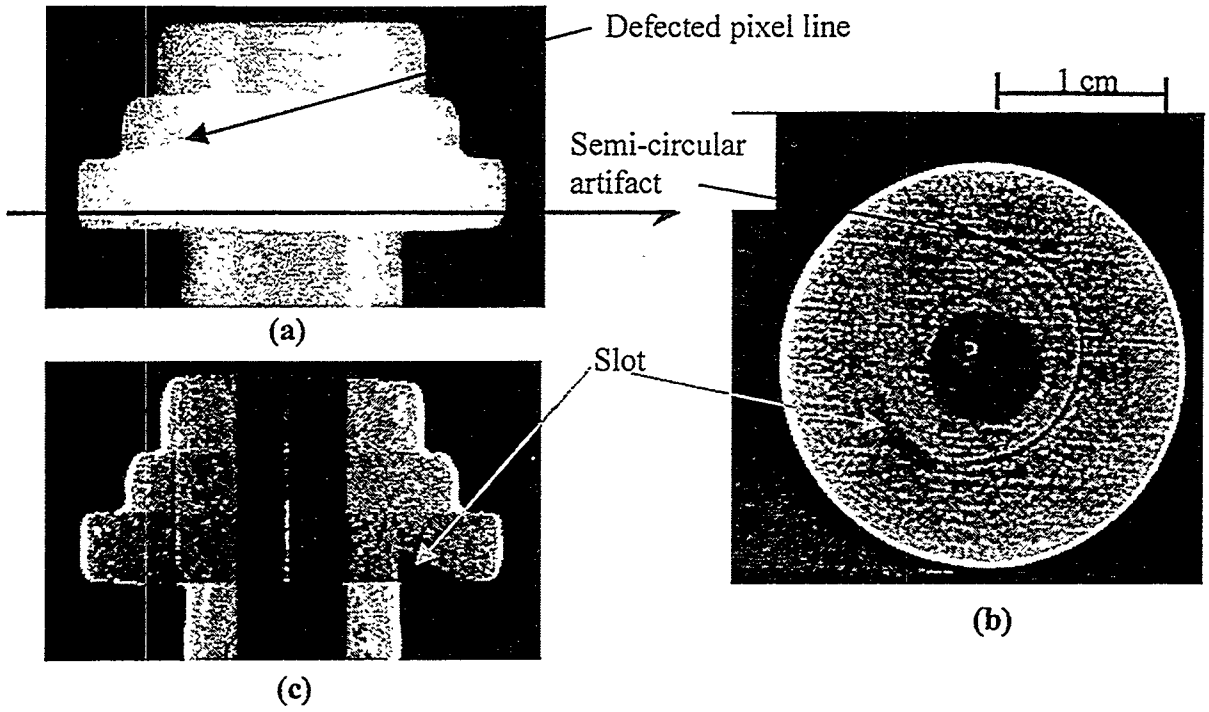

Fig. 4. (a) Normalized x-ray projection image, (b) one reconstructed x-ray CT slice of the level pointed by the arrow in (a). (c) Reconstructed axial scan generated by computer aided imaging.

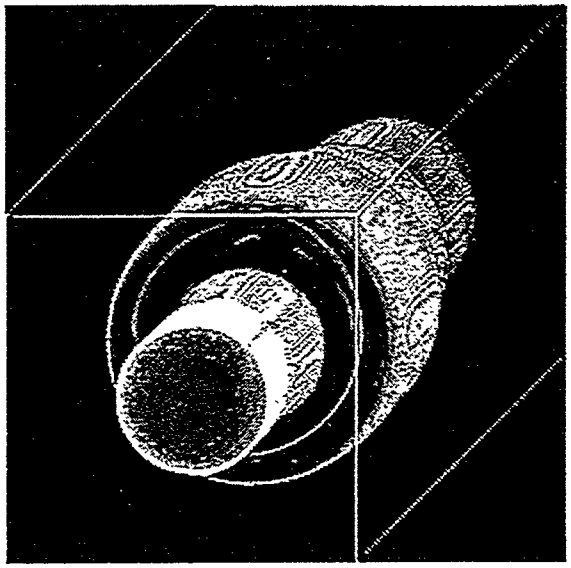

Fig. 5. 3-D surface-rendered image of ceramic insulator used for first CT image with amorphous silicon detector.

The amorphous-silicon detector is a promising x-ray detector that can enhance a CT reconstruction. It may inform us of structural information that does not obviously appear in the projection data. For cone-beam CT scan, the conventional detecting device is a CCD detector coupled with an image intensifier. Such a coupling system, that causes contour in projection data, may degrade a high-resolution scan. Even if we apply a calibration procedure to match a sampling pixel to a pixel in detector, sometimes, the accuracy of the calibration is not high enough to keep the resolution of the detector; positioning a phantom for calibration or/and structural tolerance the phantom may become a factor of degradation. However, a flat channel detector like the amorphous-silicon detector can avoid such a calibration to simplify the whole reconstruction procedure and to provide projection data with higher resolution.

C. Signal-to-Noise Ratio and Modulation Transfer Function on 2-D Projection Image

SNR was calculated from a normalized image of an aluminum step-wedge test object. The thickness of the step-wedge object varies from 1.90 mm to 2.79 mm with an increment of 0.127 mm, and the image of each step as a sub-image can be extracted to calculate the SNR for different intensities. This measurement, in each sub-image, of the parameter of the SNR allows their variations with intensity to be tracked. The SNR has been calculated according to the following;

$$SNR = \overline{m}/\sigma \qquad (1),$$

where $\overline{m}$ represents the mean value of the sub-image and σ its standard deviation. Figure 6 shows the SNR *vs.* intensity corresponding to the thickness of the step. Standard deviation, that represents a background noise, remains constant as 16, so that the SNR responds linearly as the intensity increases. The overall SNR in this picture of the step-wedge is 130.

Image resolution of the detector was determined by its MTF. A LP phantom was used, as shown in Figure 7-a, which is the normalized image. The phantom was mounted directly on the surface of detector to isolate the blurring effect due to any extended size of x-ray source (which is ~50 _m). By calculating the image contrast at different position of LP phantom, with the equation given by

$$I.C. = \frac{I_{max} - I_{min}}{I_{max} + I_{min}} \qquad (2),$$

the MTF was developed as shown in figure 7-b. The MTF shows that the detector can achieve 140-_m (3.6 LP/mm) resolution at half maximum of image contrast and a resolution of approximately one pixel (100_m) for 20% of maximum of image contrast.

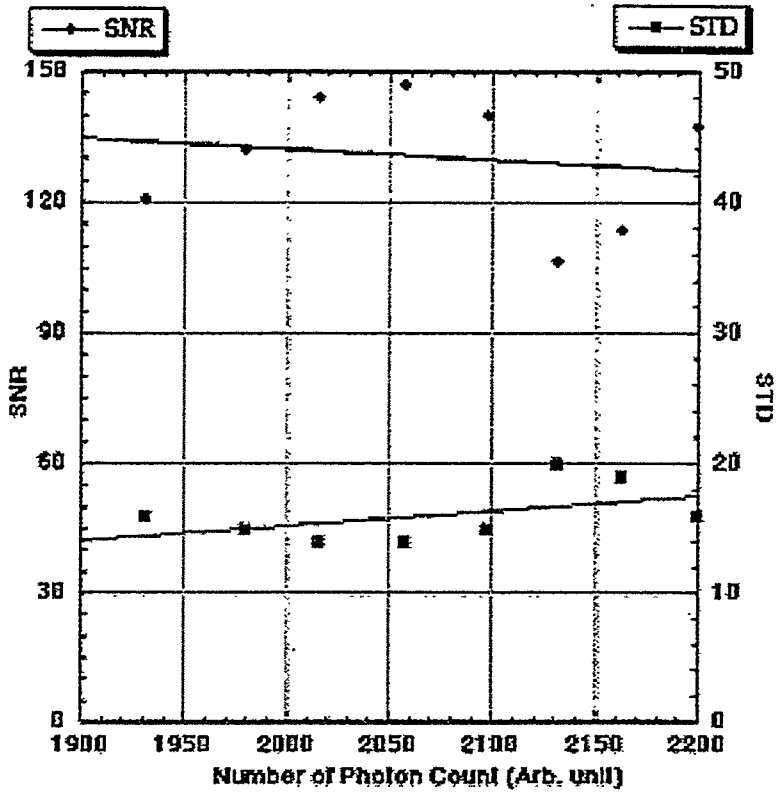

Fig. 6. Effect of thickness on SNR (Aluminum step wedge used).

The main purpose of this effort is to investigate the amorphous silicon detector for practical use in a high-resolution volumetric (cone-beam) CT scanner. To determine a resolution of 3-D reconstructed image, a phantom sample was used, which consisted of two separate cylinders made of monolithic Si_3N_4. The upper cylinder has a diameter of 20.3 mm; the bottom cylinder has a diameter of 25.4-mm diameter; and both of them have a height of 12.6-mm. The phantom sample had 9 artificial holes, that is, three sets of three different diameters of 0.33, 0.66, and 0.508 mm. 720 projection images were taken within a full range of rotation, 360 degrees, at 120kVp/0.4mA. Each projection has a size of 400x300 pixels^2, and the entire scan took about 1 hour.

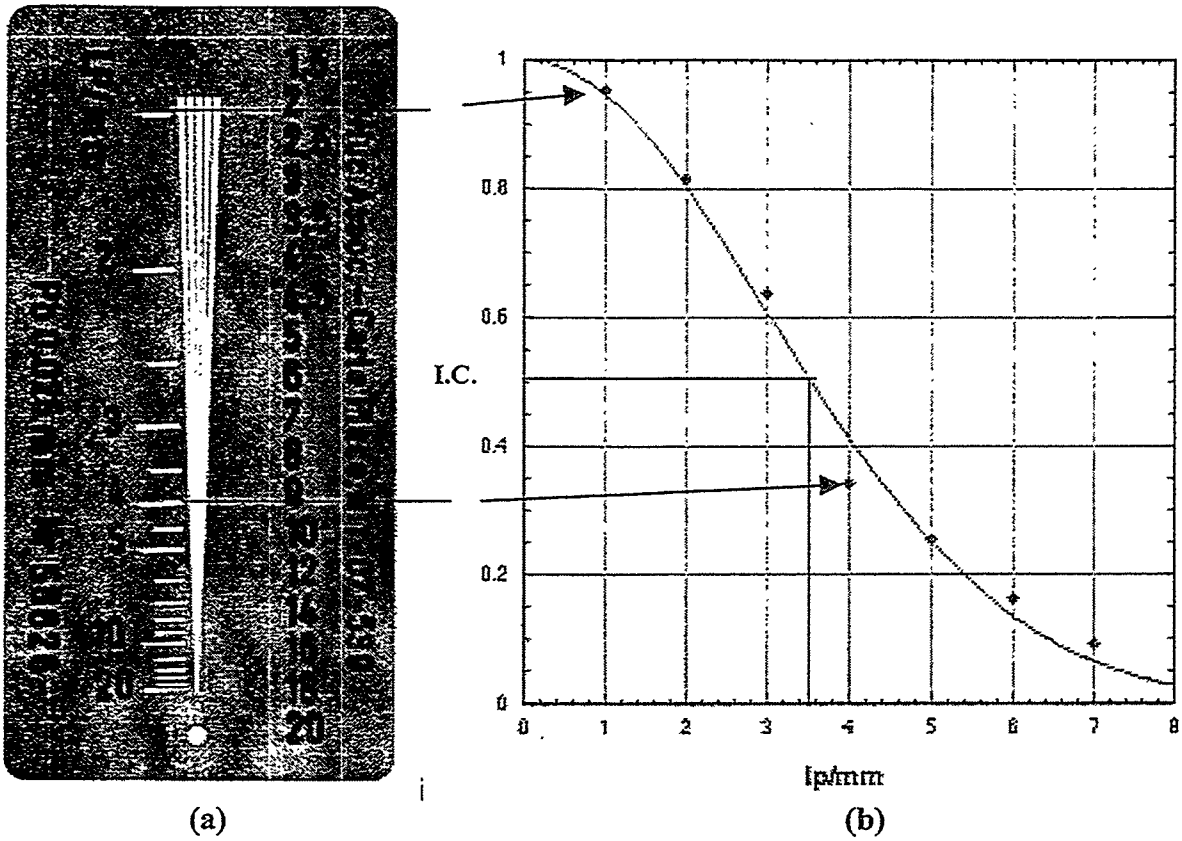

Fig. 7. Determination of spatial resolution using LP phantom. (a) Image of phantom when placed on detector (650x350 pixels²). (b) 20-frame average line pair resolution.

In general, a reconstructed image has a comparable resolution to a projection image. Figure 8-a represents a projection image of the sample while figure 8-b does a 2-D slice reconstruction at the level indicated by an arrow in figure 8-a. To evaluate the spatial resolution, a line profile was generated (see Figure 9) across one of the holes in the CT image shown in figure 8-b. The 0.508-mm hole was selected. The point spread function can been determined by differentiating the curve fit of the line profile. Finally, by applying Fourier transformation on the point spread function, as shown in Figure 9, the MTF of the CT reconstruction image can be generated in frequency domain, which has the same concept of the MTF from the projection of the LP phantom. Here, 2 f/mm corresponds to one LP/mm. The resolution of the reconstructed image is compatible to that of the projection image, which is ~140 um at the half maximum.

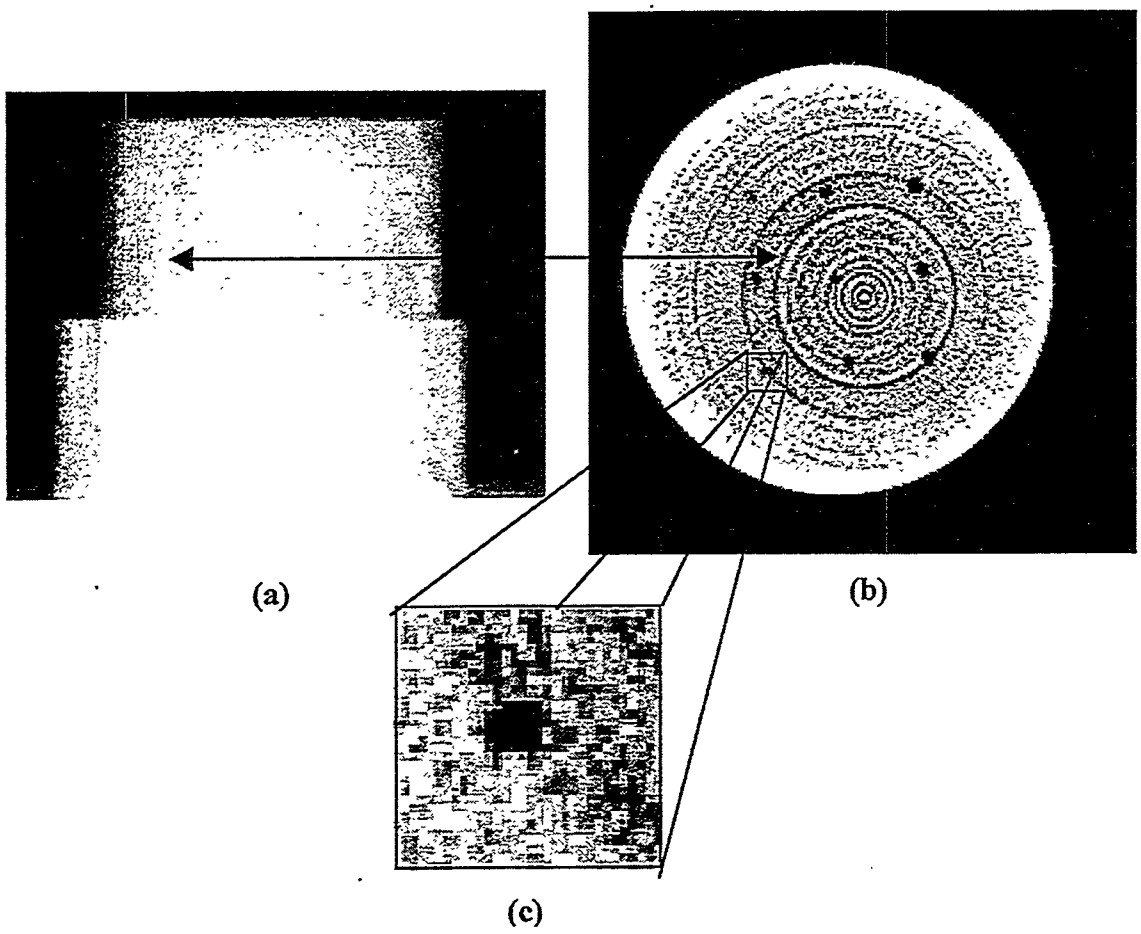

Fig. 8. X-ray images. (a) Projection image of silicon nitride (Si_3N_4) cylinders. (b) CT reconstruction image of Si_3N_4 cylinder of (a). (c) Magnified image of part of (b).

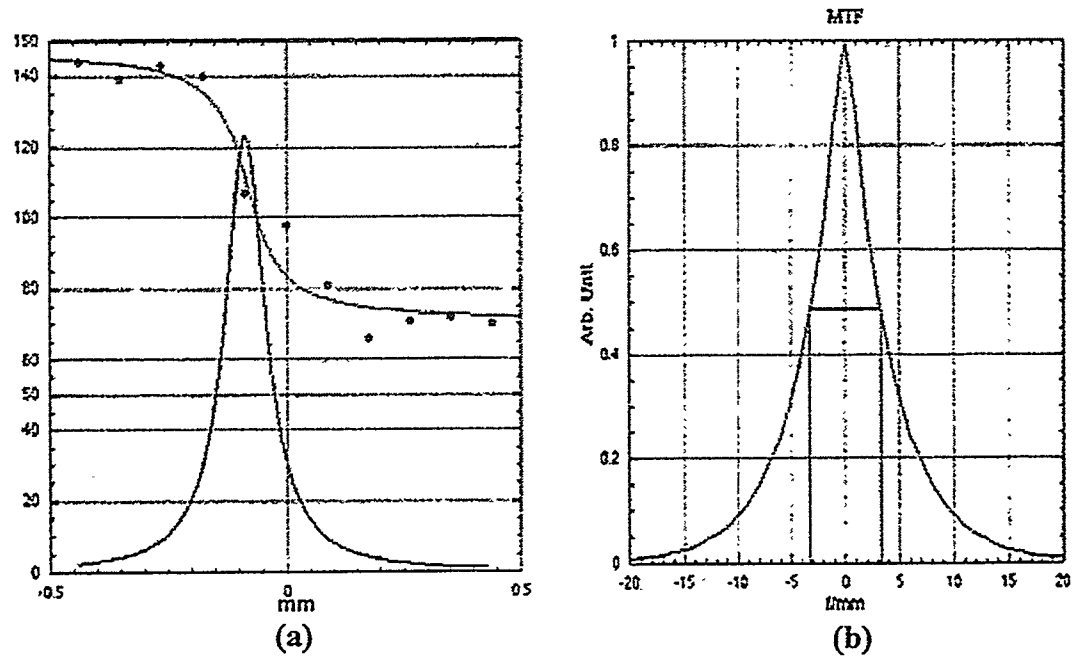

Fig. 9. (a) Line profile across 0.508-mm hole from image of Fig. 3-b. The point spread function appears as gaussian shape. (b) MTF derived from point spread function shown in (a).

In this work, the performance of the detector as an x-ray CT imaging device was examined with respect to a conventional cone-beam operation. The experimental results obtained from a MTF and a CT reconstruction have demonstrated that x-ray CT system using this type of detector offers promising improvement in image quality and, further, broadens applications in variety of fields for nondestructive evaluation. The detector, MX1024, which consists of 1024 x 1024 pixels^2 with a unit pixel size of 100 _m, is able to record high-resolution CT data of a large sample with a diameter comparable to the field of view of the detector, ~10 cm. The spatial resolution of each projection image, defined at 20% of the maximum image contrast, is on the order of 1 pixel, i.e., ~ 100 _m on the detector face, and that of a reconstructed image was also approximately one-pixel resolution.

2. SPIRAL VOLUMETRIC CT

As part of our efforts, we have been looking to increase the speed of CT data acquisition and display. The technique introduced in this report is a spiral CT scanning based on medical spiral CT, which has a capability of scanning a complete volume in a single breath hold, through table motion and subsequent x-ray image data interpolation. With the concept of this technique, we will evaluate our existing CT system for speed and figure out how to improve our CT system as a real time scanning device.

A. Characteristics of Spiral CT Scanning

Spiral CT is a major recent advance in x-ray CT for rapid volumetric scanning. Spiral scanning is achieved by continuously transporting a sample through the x-ray detector gantry in synchrony with continuous data acquisition over a multitude of 360-degree scans. It is usually performed with a planar beam like a fan beam, of which the beam size determines the increment of transporting a sample. Each scan is obtained with a period of approximately one-second gantry rotation, which is duration sufficient to complete the scan for a reconstruction.[1-5] The thickness of each slice reconstruction is related to beam width and transporting distance. The longitudinal resolution of the reconstruction in spiral CT can be improved by computational method like interpolation, so that can be close to the transverse image resolution.[6] This imaging method has the primary advantage of scanning a complete volume of the sample within a minute, ensuring slice-to-slice contiguity.

The reconstruction algorithms for spiral CT are more sophisticated because they must accommodate the spiral path traced by the x-ray source around the

sample. Data for reconstruction of images are estimated from the spiral data by interpolation. Spiral CT necessitates that planar projection sets be synthesized from helical projection data by means of interpolation.[2-7] Among various interpolation techniques, linear interpolation (LI) is usually preferred, due to its efficiency and fast performance. Typical LI techniques include full-scan, under-scan, full-scan interpolation, half-scan, half-scan interpolation, and half-scan extrapolation methods. For example, in the full-scan interpolation method, a set of planar projection data in a 360° angular range is obtained by means of LI of neighboring raw data at the same orientation.[4,5] For each slice position z and angular position _, the projection value $P_z(I, \_)$ for detector element I is calculated as

$$P_z(i, \_) = (1-w)*P_j(i, \_)+w*P_{j+1}(i, \_), \quad (3)$$

where j is of the last scan reaching angle _ before reaching position z and z_j is the respective position where $P_j(i, \_)$ is obtained. The weight w is calculated as $(z - z_j)/d$, with d being the table feed distance per 360-degree scan and $0 \leq w \leq 1$. The synthesized data are subjected to the standard image reconstruction process.

Various computer systems are used by manufacturers to control system hardware, acquire the projection data, reconstruct, display, and manipulate the tomographic images. One of typical systems, as an example, uses 12 independent processors connected by a 40-Mbyte/sec multi-bus [8]. Multiple custom array processors are used to achieve a combined computational speed of 200 MFLOPS (million floating-point operations per second) and a reconstruction time of approximately 5 seconds to produce an image on a 1024x1024-pixel display. A simplified UNIX operating system is used to provide a multitasking, multi-user environment to coordinate task.

B. Comparison of Argonne's Existing CT Systems to a Typical Spiral CT

One of ANL's existing CT systems, named as X-320, consists of an x-ray source, sample stage, detector, and computer. The x-ray source generates a x-ray cone-beam, which is Bremsstrahlung radiation, by focusing an electron beam on the tungsten target with a spot size of ~50 _m in diameter. The sample stage is comprised of 3-D transverse and rotational stages. Recommended speed for vertical stage movement is <1 mm/sec and that for rotational movement is ~1 degree/sec. Under the assumption that we use the amorphous-silicon detector mentioned previously as a detecting device, it would provide 2-D projection images within ~100 msec, which have a size of

1024x1024 and a resolution of 100 _m. The computer system is comprised of a Pentium processor (G6) with 266 MHz speed and 384 Mbytes RAM. It uses a 16-bit, black-and-white frame grabber provided by DIPIX Technologies, Inc. with a digital signal processor (DSP). The duration for the system to store each projection image is ~ 5 seconds. Reconstruction time for each slice (2-D reconstruction), of which size is 1024x1024 with 360-projection scan data, is expected to take ~10 minutes.

With the assumption of having a collimator that produces a 1-mm wide fan-beam and a multi-processor computer with DSPs, the X-320 system could be exploited as a spiral CT scanner. The speed of scanning is determined by the criteria of avoiding blurred image edges due to the movement. The image of a sample should move less than about one third of a pixel size during acquisition, which is less than 100 _m. For instance, a sample with a 10-cm diameter and a 10-cm height should move with the speed less than 100 _m/sec, that is equivalent to 0.02 rad/sec (~1 degree/sec) in rotation. As consequence, each scan to capture 360 frames during 360-degree rotation can be done with ~6 minute. Since the longitudinal increment of the sample, compatible to the thickness of the beam, is 1 mm during the period of rotation, the total scanning time will be approximately 10 hours that is 20 times longer than that of a typical CT scan with a cone-beam. Here, the scanning time is limited by the readout speed of the detector. By means of interpolation, a set of data obtained during one entire rotation produces three 2-D slice reconstructions that have a resolution compatible with that of the 2–D projection data. Each data set may be put into the spiral-beam reconstruction algorithm, and the reconstruction can be done during a period of the next entire scan.

The high-speed CT scan is mainly characterized by physical conditions of a CT system including x-ray source, detector, sample stage, and computer system; it does not necessitate a spiral-CT scan for high-speed or for high-resolution 3-D reconstruction. As mentioned previously, the X-320 CT system does not need to be operated as a spiral CT scanner. It can capture a 2-D image and save it in hard disk within ~5 seconds, and the 360-frame scan covering the entire body of a sample takes ~30 minutes. Further, if the computer hardware can be customized into a multi-processor computer or a parallel operating system, a 360-frame CT-scan can be done within 6 minutes that is limited only by the image resolution (i.e., the avoidance of image blurring). In the future, we need to verify which computer system is suitable for the X-320 system in order to perform fast data acquisition.

3. X-RAY DENSITOMETRY OF DIESEL ENGINE VALVE GUIDES

All Si3N4/chopped carbon fiber samples have been sent to Allied Signal Ceramics for sectioning and destructive density measurements. During this period we finished 3D x-ray imaging CT of these diesel engine valve guide samples using the high spatial resolution 160 kVp microfocus x-ray imaging system and have compared the results of the nondestructively measured density profiles determine using these two machines. All x-ray transmission data on the 160 KVp microfocus were taken at 135 kVp/ 0.3 mA. Figures 10 to 13 show typical cross section CT reconstructions, which provides the gray scale information used to determine density variations as a function of the concentration of chopped carbon fiber content. These image data sets show about 1 to 2% deviation from the average density, which depends on sampling location. Most of samples have a density in the middle portion (L/2 location) that is higher than that at either end.

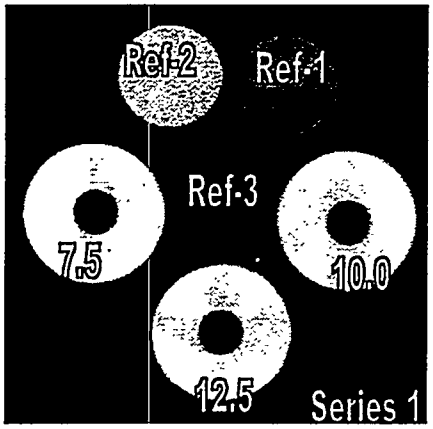

Allied-Signal/Caterpillar, Series 1, Mix-2 Density

Location	Percent Carbon Fiber		
	7.5	10.0	12.5
L/4	2.34	2.28	2.22
L/2	2.35	2.30	2.23
3L/4	2.33	2.29	2.22

Legend: Ref-1 = lucite
Ref-2 = teflon
Ref-3 = air
Sample CF content listed in %

Fig. 10. X-ray CT image reconstructions of Allied-Signal Si_3N_4/chopped carbon fiber diesel engine valve guides, Series 1, Mix-2.

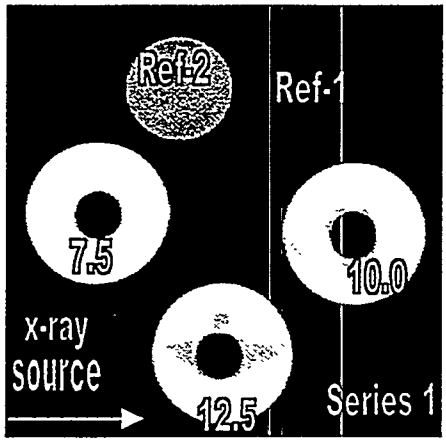

Allied-Signal/Caterpillar, Series 1, Mix-3 Density

Location	Percent Carbon Fiber		
	7.5	10.0	12.5
L/4	2.35	2.29	2.26
L/2	2.35	2.29	2.20
3L/4	2.30	2.26	2.22

Fig. 11. X-ray CT image reconstructions of Allied-Signal Si_3N_4/chopped carbon fiber diesel engine valve guides, Series 1, Mix-3.

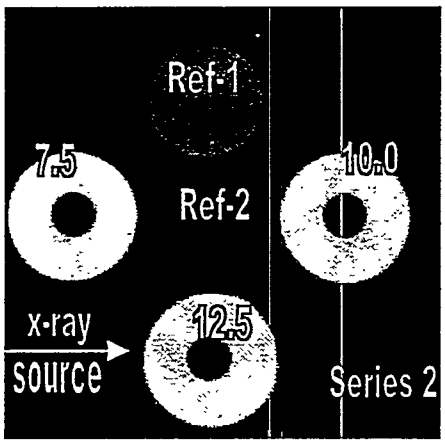

Allied-Signal/Caterpillar, Series 2, Mix-1 Density

Location	Percent Carbon Fiber		
	7.5	10.0	12.5
L/4	2.53	2.49	2.42
L/2	2.53	2.49	2.41
3L/4	2.47	2.47	2.42

Legend: Ref-1 = lucite
Ref-2 = air
Sample CF content listed

Figure 12 – X-ray CT image reconstructions of Allied-Signal Si_3N_4/chopped carbon fiber diesel engine valve guides, Series 2, Mix-1

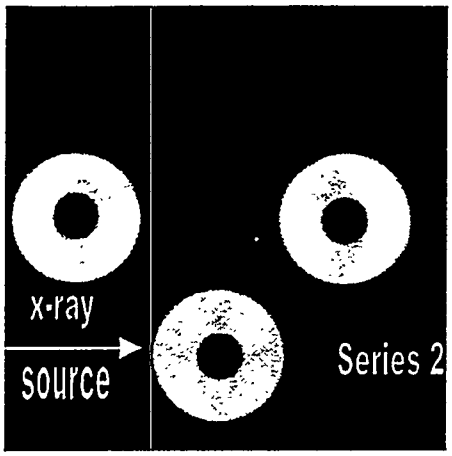

Allied-Signal/Caterpillar, Series 2, Mix-2 Density

Location	Percent Carbon Fiber		
	7.5	10.0	12.5
L/4	2.54	2.52	2.41
L/2	2.54	2.54	2.40
3L/4	2.54	2.53	2.38

Fig. 13. X-ray CT image reconstructions of Allied-Signal Si_3N_4/chopped carbon fiber diesel engine valve guides, Series 2, Mix-2

Figure 14 is a summary of the comparison of density profiles of these diesel engine valve guides provided by the two different machines, 160 kVp and 320 kVp x-ray systems. The difference in averaged densities of each sample is ~2%. Figure 15 is a plot of density as a function of the applied energy. Since the absorption coefficients of materials decreases as the energy of x-rays increase, the density is inversely proportional to the energy. Additional analysis of the energy-dependence on density is incomplete.

Sample set 1

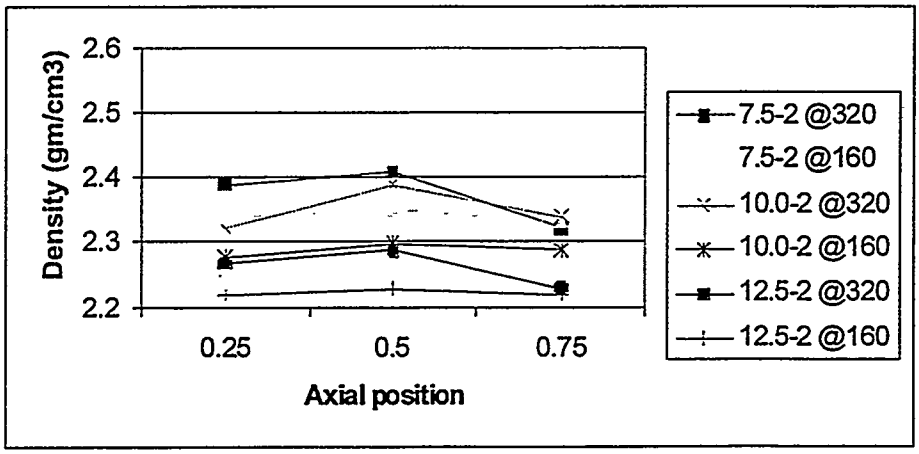

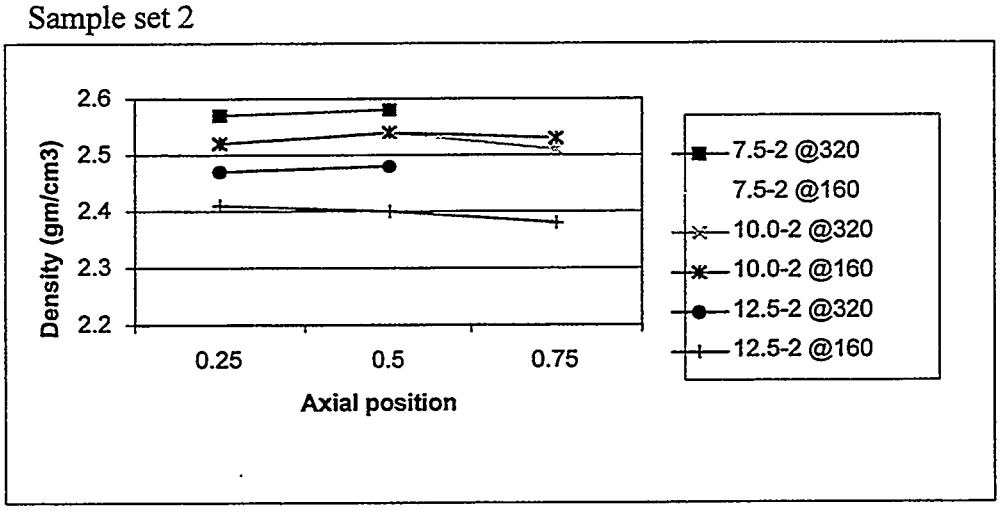

Fig. 14. Comparison of averaged density provided by 320 kVp and 130 kVp systems.

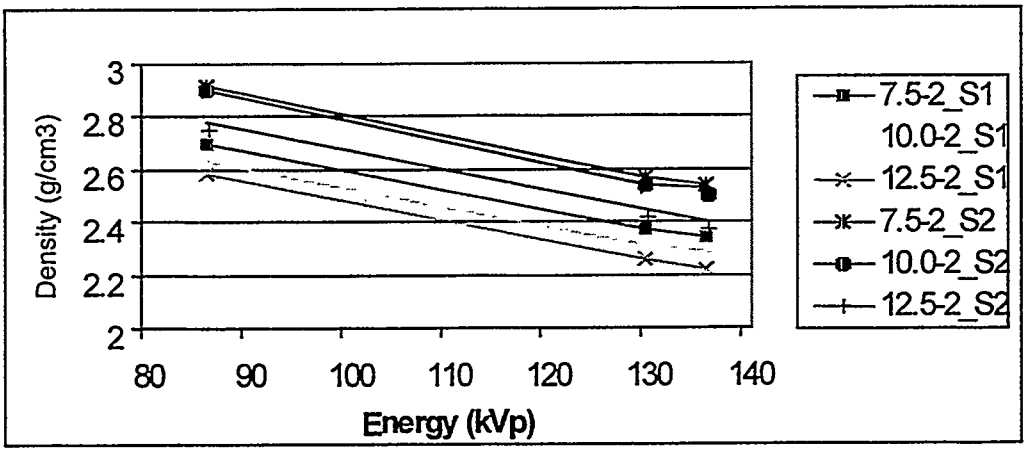

Figure 15. Energy-dependency of density

References

1. J.A. Brink, J.T. Lim, G. Wang, J.P. Heiken, L.A. Deyoe, and M.W. Vannier, "Technical optimization of spiral CT for depiction of renal artery stenosis: *in vitro* analysis," Radiology, **194**, 157-163 (1995).

2. G. Wang and M.W. Vannier, "Stair-step artifacts in three-dimensional helical CT: an experimental study," Radiology, **191**, 79-83 (1994).

3. A. Polacin and W.A. Kalender, "Measurement of slice sensitivity profiles in spiral CT," Med. Phys., **21**, 133-140 (1994).

4. W.A. Kalender and A. Polacin, "Physical performance characteristics of spiral CT scanning," Med. Phys., **18**, 910-915 (1991).

5. W.A. Kalender, W. Seissler, and E. Klotz, and P. Vock, "Spiral volumetric CT with single-breath-hold technique, continuous transport, and continuous scanner rotation," Radiology, **176**, 181-183 (1990).

6. G. Wang and M.W. Vannier, "Longitudinal resolution in volumetric x-ray computerized tomography-Analytical comparison between conventional and helical computerized tomography," Med. Phys., **21**, 429-433 (1994).

7. A. Polacin, W.A. Kalender, and G. Marchal, "Evaluation of section sensitivity profiles and image noise in spiral CT," Radiology, **185**, 29-35 (1992).

8. I.A. Cunningham and P.F. Judy, *The Biomedical Engineering Handbook* (IEEE Press, 1995), Chap. 64.

TESTING AND EVALUATION OF ADVANCED CERAMICS AT HIGH TEMPERATURE

J. Sankar, A. D. Kelkar and L. Russell (Department of Mechanical Engineering, North Carolina A & T University, Greensboro, NC 27407)

Objective/Scope

The objective of this research is to test and evaluate the long-term mechanical reliability of a Si_3N_4 at temperatures up to 1300^{0}C. The required research includes four (4) major tasks:

Task 1. Cyclic Fatigue Testing of PY6 and GS 44

Cyclic fatigue of GTE-PY6 and GS 44 silicon nitride shall be performed at lower temperatures to investigate characteristics of the material at the temperature range of 500^0 - 1100^{0}C. At these lower temperatures, there may be a true cyclic fatigue effect that enhances failure compared with the static load case.

Task 2. Stress-Rupture Study of PY6 and GS 44

Stress-Rupture testing of GTE-PY6 and GS-44 silicon nitride shall be performed at a lower temperature range of 500^0 - 1100^{0}C. Since there is little information about the time dependent behavior of this material is available at this temperature regime, this task should provide some valuable data.

Task 3. Four (4) Point Flexural Test

Four (4) point flexural tests shall be performed for AlliedSignal's GS-44 silicon nitride from room temperature to elevated temperature.

Task 4. Thermal Barrier Protective Surface Coating

A basic science understanding of thermal barrier protective surface coating to promote high-temperature performance and the effects of notches and oxidation at the roots of the notches at elevated temperatures for silicon nitride shall be carried out.

Task 5. Microscopy

High-resolution microscopy and fractography work will be a part of all tasks discussed above.

Technical Highlights and Discussion

During this reporting period, flexural experimental data and finite element analysis modeling were completed on coated and as received GS-44 silicon nitride specimens.

Objective/ Scope

Sintered Si_3N_4 was deposited with calcium stabilized zirconia slurry and was compared with as received samples. Isothermal soaking in an oxidative environment was used to determine the feasibility of this protective barrier coating (PBC) and its contributions to the flexural behavior of the Si_3N_4. The substrates were soaked for 32 and 96 hours at 1275 °C and tested at room temperature in a four points flexural test configuration.

Introduction

Silicon based ceramics have been developed to function in high temperature applications. While they are highly oxidation resistant, they are not impervious to thermal degradation. Protective barrier coatings (PBCs) are used to shield silicon based components used in aggressive high temperature environments. PBCs improves mechanical properties and enhances the performance of the material by reducing their cooling air requirements. PBCs are used in gas turbine engines, heat exchangers, and advanced internal combustion engines. For materials experiencing creep, fatigue, and tensile type stresses under severe environmental conditions, a shorter life expectancy rate is expected when compared to materials with a protective barrier coating preserving the surface. Deterioration of the surface affects the performance of the material. By applying a protective barrier coating to the surface of the material, it enables the material to withstand the surrounding conditions longer by enhancing the mechanical properties. The purpose of this research is to develop a systematic approach to understanding how the coating effects the material behavior of sintered silicon nitride substrates.

Experimental Data

Material

The material used for investigation is sintered silicon nitride, GS-44, provided by Allied Signal. The dimensions for the samples used in the bend test are 3 x 4 x 45 millimeters. Earlier studies on silicon nitride states it contains small amounts of Y_2O_3, Al_2O_3, and other minor constituents as densification aids.

Thermal Soaking

The purpose of thermal soaking at high temperatures is to study how the PBC protects the microstructure and changes the mechanical behavior after thermal degradation. It is believed that protecting the surface increases the life of the material and enhances its mechanical properties.

Protective Barrier Coating

As a preliminary investigation, the following was carried out. Adiabatics, Inc., Columbus, IN, applied the slurry deposited protective barrier coating for the samples tested. Each sample was grit blasted on the coating side for sample preparation. The protective barrier coating mixture consist of calcium stabilized zirconia, alumina and amorphous silica hollow spheres, with a mixing binder solution consisting of distilled water and zinc chromate, and a densifying binder solution consisting of saturated chromic acid solution.

Test Equipment and Characterization

Applied Test Systems, Inc., Butler, PA, Four Point Bend Test Series 1605 Computer-Controlled Universal Testing Machine was used to generate flexure strength, Young's modulus, and load- displacement curves. We used their 3330 High Temperature Furnace with Kanthal Super "33" elements and type S platinum/ platinum – 10% rhodium thermocouples. The maximum temperature range of the furnace is 1648 °C (3000 °F). The temperature control system controls the amount of power to the resistive heating elements, as required, to achieve and maintain the desired temperature as measured through the control thermocouple.

The test set-up uses Applied Test System's 4231 High Temperature Bend Testing Extensometer. The extensometer averages the readings during testing.

Scanning electron microscope (SEM) was used to conduct fractographic studies on fractured surfaces.

Test Conditions

Testing of coated and virgin GS-44 silicon nitride materials were performed in displacement control mode using Test-Vue software provided by Applied Test Systems, Inc. The specimens were tested with the PBC side facing downward to experience tensile stresses on the coating.

Flexural Testing Conditions:
Four Point Flexural Test

Four-point bend test consists of measuring the deflection of a simple beam subjected to symmetrical loading. The American Society of Testing and Materials (ASTM C 1161-9) Standard Test Method for Flexural Strength of Advanced Ceramics at Ambient Temperature was followed as a guide for testing. The experiments were performed using displacement control at a rate of 0.5 mm/ min.

Three sets of samples were tested and compared to obtain an accurate comparison of virgin verse coated silicon nitride samples. Two sets of samples were soaked for 32 and 96 hours at 1275 °C and tested to failure at room temperature. The furnace was programmed to ramp to 1275 °C and soak for 32 and 96 hours. After soaking, the furnace would shut down and cool to room temperature.

RESULTS AND DISCUSSION

Tables 1, 2, 3, 4, and 5 lists the results from the flexural test performed on the silicon nitride samples. All flexural tests were completed at room temperature. Table 1 lists the results from the specimens that were in as received condition from the manufacturer. Tables 2 and 3 lists the results from the as received specimens that were soaked for 32 and 96 hours at 1275 °C in an oxidizing environment. Tables 4 and 5 lists the results from the slurry coated silicon nitride specimens that were soaked for 32 and 96 hours at 1275 °C in an oxidizing environment.

Table 1. Silicon Nitride specimen test at room temperature.

Silicon Nitride Samples						
Test	**Test1**	**Test2**	**Test3**	**Test4**	**Test5**	**Test6**
Fracture Strength- Mpa	713	928	611	837	827	852
Maximum Load- N	855	1114	733	1004	992	1022
Maximum Deflection- mm	0.328	0.411	0.284	0.36	0.379	0.355
Young's Modulus- GPa	296.5	302.75	295.5	310.5	308	328
Fracture Location	center	center	outer pin	center & outer pin	inner pin	outer pin

Table 2. Silicon Nitride samples soaked for 32 hours at 1275 °C and tested at room temperature.

Silicon Nitride Samples				
File Name	**32SoakA**	**32SoakB**	**32SoakC**	**32SoakD**
Fracture Strength- Mpa	590.83	636.6	615	610
Maximum Load- N	709	764	739	732
Maximum Deflection- mm	0.311	0.448	0.437	0.417
Young's Modulus- GPa	305	305	300	315
Fracture Location	outer pin	inner pins	inner pin	inner pin

Table 3. Silicon Nitride samples soaked for 96 hours at 1275 °C and tested at room temperature.

Silicon Nitride Samples					
File Name	**96SoakA**	**96SoakB**	**96SoakC**	**96SoakD**	**96SoakE**
Fracture Strength- Mpa	550	540	561	624	626
Maximum Load- N	660	648	673	748	752
Maximum Deflection- mm	0.379	0.406	0.426	0.422	0.378
Young's Modulus- Gpa	268	269	287	295	270
Strain Energy- N*mm	86.89	79.80	74.21	100.09	108.23
Fracture Location	inner pins	inner pin	center	inner pins	inner pins

Table 4. Slurry coated silicon nitride samples soaked for 32 hours at 1275 °C and tested at room temperature.

Slurry Coated Silicon Nitride Samples					
File Name	**32coatA**	**32CoatB**	**32CoatC**	**32CoatD**	**32CoatE**
Maximum Load- N	807.5	766.8	776	756.6	693.3
Maximum Deflection- mm	0.458	0.527	0.445	0.556	0.463
Fracture Location	inner pins	center	center	inner pins	inner pin

Table 5. Slurry coated silicon nitride samples soaked for 96 hours at 1275 °C and tested at room temperature.

Slurry Coated Silicon Nitride Samples					
File Name	**96coatA**	**96CoatB**	**96CoatC**	***96CoatD***	***96CoatE***
Maximum Load- N	594	703	691	741	661
Maximum Deflection- mm	0.547	0.642	0.783	0.62	0.609
Strain Energy- N*mm	75.87	102.21	127.34	140.34	125.63
Fracture Location	inner pin	inner pin	inner pin	inner pin	inner pin

Figure 1 contains two micrographs of a mounted specimen displaying the porosity with in the slurry coating. Figure 2 displays the load-displacement curve for the as received sample tested at room temperature. Figure 3 displays the load- displacement curves for slurry coated and as received GS-44 Si_3N_4 substrates soaked for 96 hours at 1275 °C. Figure 4 displays the SEM fractograph of a slurry coated GS-44 Si_3N_4 substrate soaked for 96 hours.

Four Point Bend Test: Mechanics and Modeling

The modulus of elasticity in bending was determined by using the load verse displacement data from the four-point bend test. The load and deflection data was inserted into equation (1) the modulus of elasticity equation for four-point bending. Where, E_b is the modulus of elasticity in Pa; L is the distance between the two outer support pins, mm; t is the specimen thickness, mm; w is the specimen width, mm; ΔP is the increment in load, Newtons; $\Delta\delta$ is the increment in displacement. Equation (1) was derived from the deflection equation using the double integration technique.

$$(1)\ E_b = \frac{11PL^3}{768I}\frac{\Delta P}{\Delta \delta}$$

The flexural strength is determined by the maximum amount of load the specimen can withstand during bending. The experimental normal stress derived from the standard formula, equation (2) used to determine the flexural strength.

$$(2)\ \sigma_{max} = \frac{3PL}{4wt^2}$$

Where P is the applied load; L is the distance between the two outer support pins, mm; t is the specimen thickness, mm; w is the specimen width, mm.

Strain Energy

Strain energy (U), equation 3 is the work done by slowly increasing the load on the substrate as it undergoes deformation. The total work is equal to the area under the load- displacement diagram (figure 2).

$$(3) \qquad U = \frac{M^2 L}{2EI}$$

Where M is the applied moment; L is the distance between the two outer support pins, mm; E is Young's modulus, N/mm^2; and I the moment of inertia, mm^4.

Numerical analysis was used to determine the actual values of strain energy presented in tables 3 and 5. Linear regression was used to determine the assumed linear function that represents the load-displacement curve. The coefficients used in the linear equation (equation (4)) were determined by simplifying and rearranging a set of linear algebraic equations. Finally, a two term Gauss Quadrature was used to determine the area under the load- displacement curve.

$$(4) \quad G(x) = a_1 + a_2 x$$

Finite Element Analysis Modeling

Finite element analysis (FEA) was used to analyze the structure in order to determine the state of stress in the four-point bend test experiment. Finite element analysis is a numerical tool that converts differential equations representing engineering problems into algebraic equations that are solved to obtain the solution. Finite elements are subdivided within the domain of the structure and interconnected at points around each element called nodes. By subdividing the structure into elements and applying boundary conditions, each element can be numerically solved and combined to obtain the solution for the entire model. A three dimensional model was developed using brick elements with three degrees of freedom. The model was developed to compare with the data from the four point flexural test performed on the GS-44 silicon nitride specimens.

Comparison: Experimental vs. Finite Element Model

A three- dimensional finite element model with 1499 nodes and 863 brick elements was developed to predict the displacement of a flexural test specimen. To simulate the outer support pins the nodes were constrained in the x, y, and z directions. The results from the finite element model were consistent with the load -displacement data from the four point flexural test. Figure 5 demonstrates how the load-deflection curves from the finite element model results and the experimental data are within acceptable range. Tables 6 and 7 display total load, normal stress, and displacement at the center of the beam from the experiment and the FEA model. Table 7, contains the absolute percent error of the normal stress between the experimental data and the FEA model results. The percent difference was calculated by using equation 5.

$$(5)\ \text{Percent Difference} = \frac{|\text{FEM result} - \text{Experimental result}|}{\text{FEM result}}$$

It can be seen from the table 7 that the finite element results and the experimental data are with in two percent using equation (5).

Table 6. Finite Element Results using Ex = 309 GPa; G= 128.8 GPa

Load / Node	Total Load	Displacement	Normal Stress
0.1 N	1 N	.000334 mm	.842 MPa
0.5 N	5 N	.00167 mm	4.21 MPa
5	50	.0167	42.1
20	200	.0668	168
40	400	.134	337
80	800	.267	673

Table 7. Experimental and Mechanics of Materials Results

Total Load	Displacement	Normal Stress	*% Difference*
1 N	0.00033 mm	.833 MPa	1.06 %
5	0.00165	4.16	1.18
50	0.0165	41.6	1.18
200	0.0659	167	0.60
400	0.132	333	1.18
800	0.264	667	0.89

Figure 5 demonstrates how the load-deflection curves from the finite element model results and the as received GS-44 Si_3N_4 flexural experimental data are within acceptable range. Figure 6 shows the axial stress distribution of the beam.

Conclusions

There were some improvements in the mechanical properties of the slurry coated silicon nitride specimens when compared to the as received silicon nitride samples soaked at 1275 °C for 32 and 96 hours. After 96 hours of isothermal soaking the slurry coated substrate experienced an increase in deflection when tested at room temperature. There is a 37% increase in deflection of the slurry coated Si_3N_4 when compared to the as received samples under identical isothermal soaking conditions. The coating increased the elastic range and crack resistance of the substrate. This benefit is attributed to the protective coating absorbing energy as the test pins travels into the coating. The coating also provides crack deterrent mechanisms or a cushioning effect before the monolithic ceramic experiences the loading. The high concentration of porosity in the PBC provides crack collapsing mechanisms that increase the strain energy of the overall material system.

The results from the finite element model were consistent with the load -displacement data from the four point flexural test. The beam deflection and the axial stress are within two- percent using equation 5.

Status of Milestones

On Schedule

Communications/Visitors/Travel

Problems Encountered

None

Fig.1 A) and B) Micrographs of mounted slurry coated silicon nitride specimen.

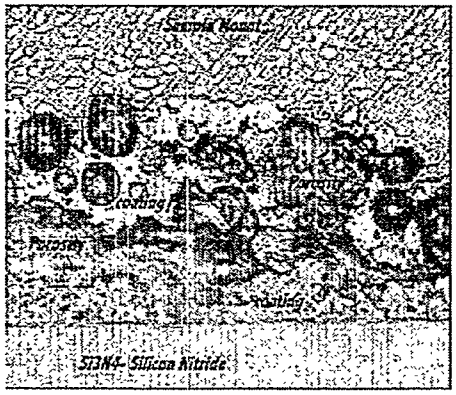

A)

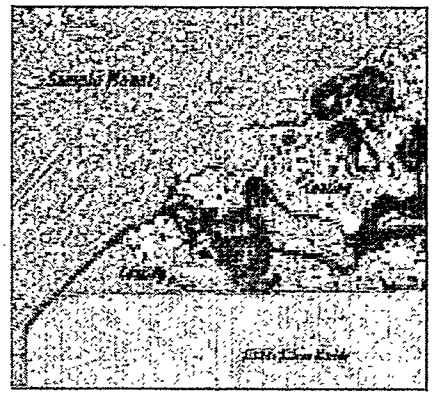

B)

Fig. 2 Load- Displacement curve for Room Temp four- point Flexural test of as received silicon nitride.

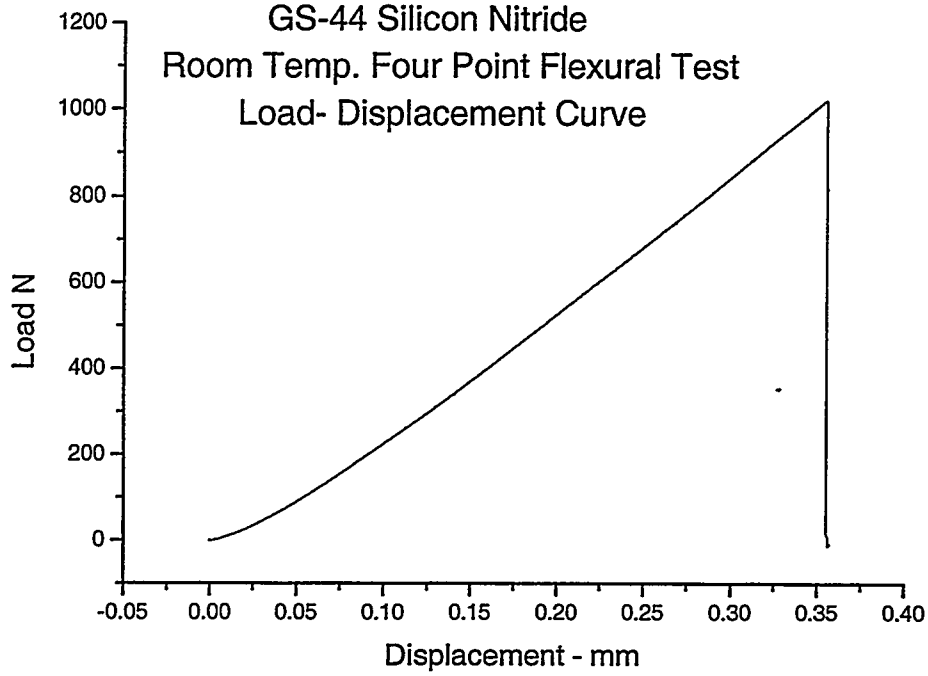

Fig. 3 Load - Displacement curves for slurry coated and as received silicon nitride substrates soaked for 96 hours at 1275 °C.

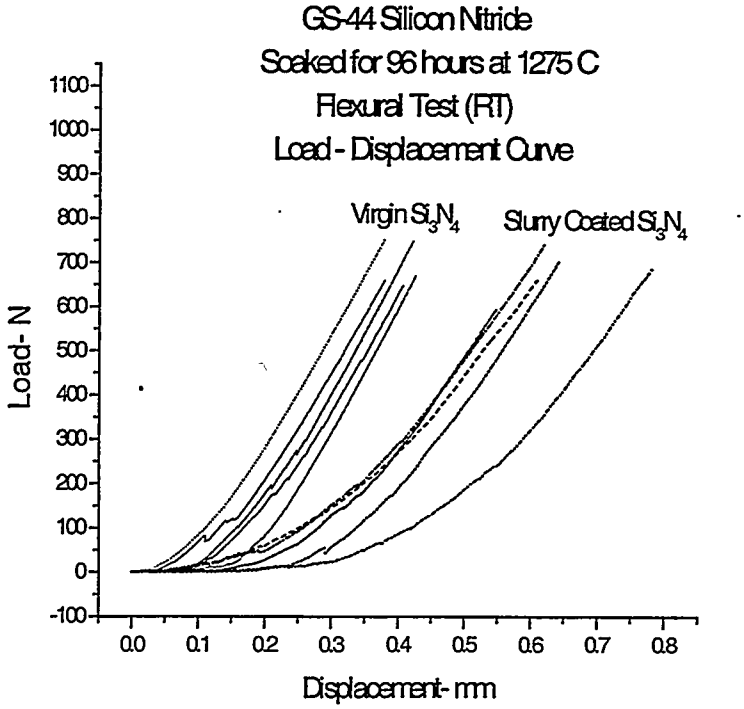

Fig. 4 SEM micrograph of fractured surfaces.

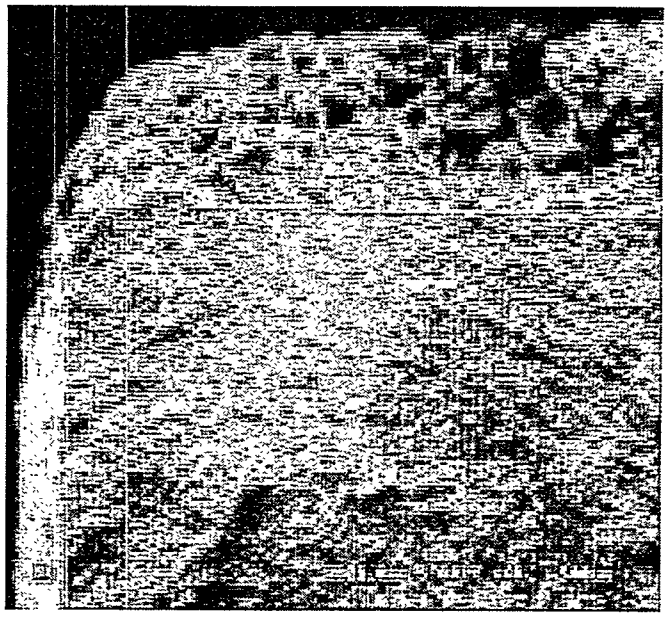

Fig. 5 Comparison of FEM Results with Experimental Data (Load (N)-Deflection (mm) Curve)

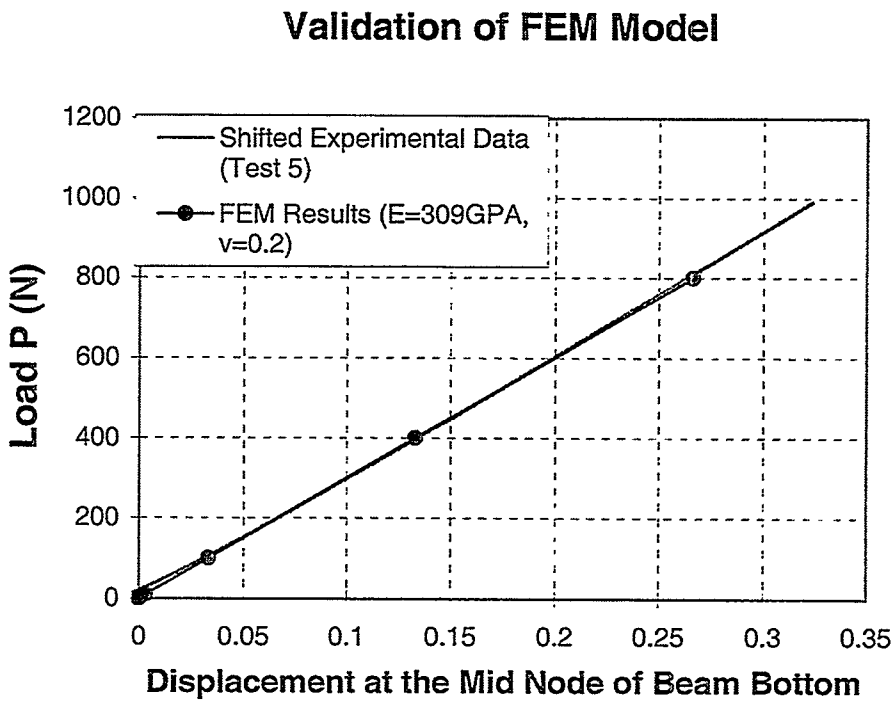

Fig. 6 Axial stress distribution.

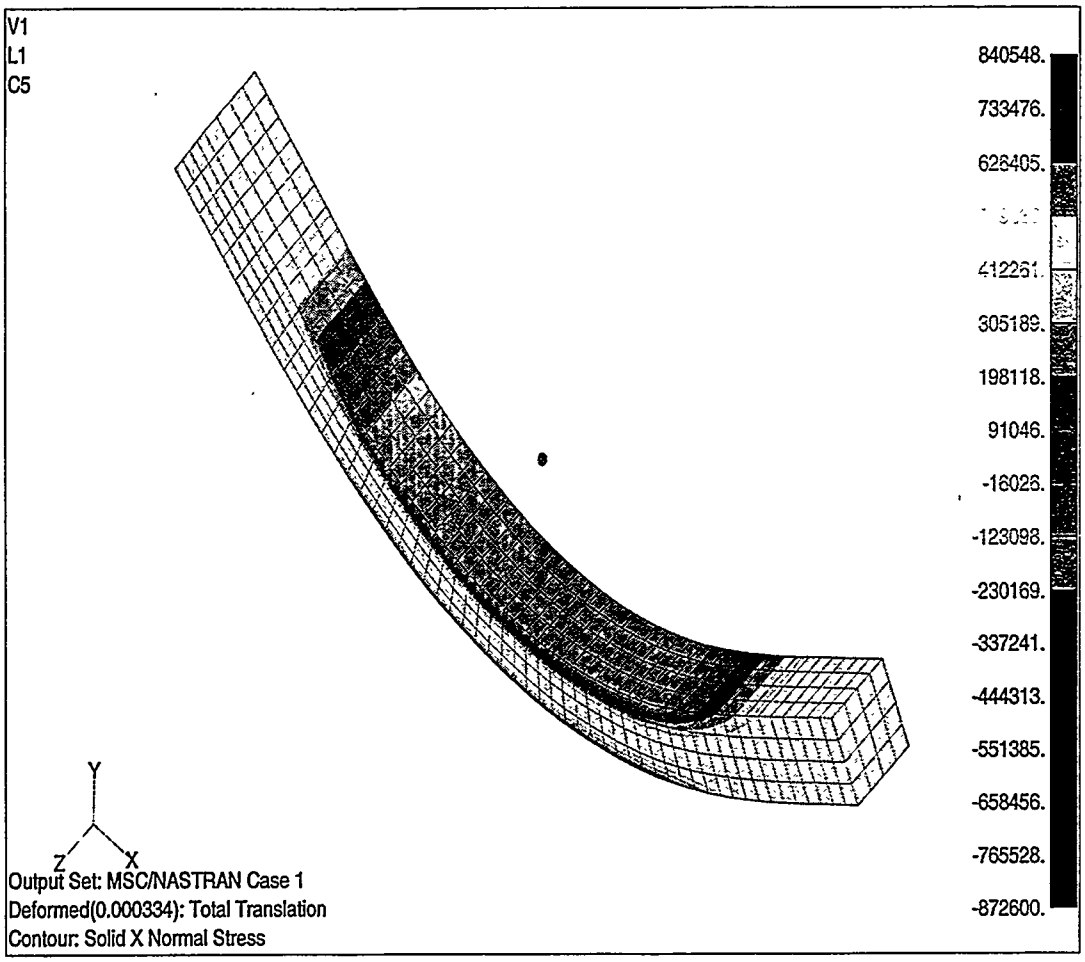

Life Prediction of Ceramic Diesel Engine Components

A. A. Wereszczak (ORNL), T. P. Kirkland (ORNL), M. J. Andrews (ORNL), M. K. Ferber (ORNL) and R. Tandon (Caterpillar)

Objective/Scope

The valid prediction of mechanical reliability and service life is a prerequisite for the successful implementation of structural ceramics as internal combustion engine components. There are three primary goals of this research project which contribute toward that implementation: the generation of mechanical engineering data from ambient to high temperatures of candidate structural ceramics; the microstructural characterization of failure phenomena in these ceramics and components fabricated from them; and the application and verification of probabilistic life prediction methods using diesel engine components as test cases. For all three stages, results are provided to both the material suppliers and component end-users.

The systematic study of candidate structural ceramics (primarily silicon nitride) for internal combustion engine components is undertaken as a function of temperature (< 900°C), environment, time, and machining conditions. Properties such as strength and fatigue will be characterized via flexure and rotary bend testing.

The second goal of the program is to characterize the evolution and role of damage mechanisms, and changes in microstructure linked to the ceramic's mechanical performance, at representative engine component service conditions. These will be examined using several analytical techniques including optical and scanning electron microscopy. Specifically, several microstructural aspects of failure will be characterized:

(1) strength-limiting flaw-type identification;
(2) edge, surface, and volume effects on strength and fatigue size-scaling
(3) changes in failure mechanism as a function of temperature;
(4) the nature of slow crack growth; and
(5) what role residual stresses may have in these processes.

Lastly, numerical probabilistic models (*i.e.*, life prediction codes) will be used in conjunction with the generated strength and fatigue data to predict the failure probability and reliability of complex-shaped components subjected to mechanical loading, such as a silicon nitride diesel engine valve. The predicted results will then be compared to actual component performance measured experimentally or from field service data. As a consequence of these efforts, the data generated in this program will not only provide a critically needed base for component utilization in internal combustion engines, but will also facilitate the maturation of candidate ceramic materials and a design algorithm for ceramic components subjected to mechanical loading in general.

Technical Progress

The description of the technical progress for the present reporting period is in three sections: laboratory testing of NT551 specimens, laboratory testing of NT551 valves, and Caterpillar testing program. The former two sections are affiliated with the near-completion of this project's life prediction work with DDC's Series 149 exhaust valve, while the latter effort constitutes this project's latest life prediction effort with Caterpillar.

Laboratory testing of NT551 specimens

Tensile dynamic fatigue testing was completed during the present reporting period. A modified ORNL button-head tensile specimen was used. The gage section surfaces of all specimens were transversely ground using a 320 grit wheel. The specimens had a gage section diameter of 3.5 mm, a gage length of 30 mm, and a gage volume of 288.6 mm^3. Three rates were used for

the testing (30, 0.3, and 0.003 MPa/s), and all specimens were tested at 20°C. Due to a lack of specimens, only 12-13 specimens were tested per condition.

A decrease in the uncensored characteristic tensile strength occurred as the applied stressing rate decreased. The Weibull distributions for the three tensile specimen sets are shown in Fig. 1, and the distribution parameters are summarized in Table I. When the tensile strengths were graphed as a function of stressing rate (see Fig. 2), a fatigue exponent equaling 46 was obtained. This loss of strength as a function of stressing rate at 20°C is consistent with the loss of NT551 strength exploited in earlier testing of ASTMC1161B and cylindrical specimens [1]. This strength data will be pooled with data generated with other specimen geometries to predict the mechanical performance of actual NT551 valves. Fractography was completed with these tensile specimens and more than one strength-limiting flaw was identified.

Laboratory testing of NT551 valves

The strengths of four sets of valves were measured. Two of the sets were "as-received" sets while the other two sets were comprised of engine-tested valves; the strengths of the as-received sets were compared to the retained strengths of the engine-tested sets. The fillet radius on the valves were either longitudinally or transversely machined, and this served as an independent parameter. The engine-tested valves whose fillet radius was longitudinally machined were engine tested at Detroit Diesel Corporation (DDC) for 166 hours. The engine-tested valves whose fillet radius was transversely machined were engine tested at DDC for 1000 hours. The strength of the as-received valves and the retained strengths of the engine tested valves were measured using a valve test facility constructed by engineers in ORNL's Engineering Technology Division [2]. The face of each valve was hydraulically loaded until fracture resulted. DDC-supplied valve seats and guides were incorporated in the testing. The strength of valves that were not subjected to engine testing were also examined, and are referred to in the present discussion as "as-received" strengths.

The uncensored strength distributions of the as-received longitudinally and transversely machined fillet valves are compared in Fig. 3. The strengths were higher for the valves whose fillet radius was longitudinally machined (note, the greatest principal tensile stress during both service and laboratory strength testing is located at the surface of the valve's fillet radius). Engine testing the longitudinally machined valves for 166 hours resulted in a decrease in the retained characteristic strength of approximately 26% (see Fig. 4). Engine testing the transversely machined valves for 1000 hours resulted in a decrease in the retained characteristic strength of approximately 8% (see Fig. 5). These decreases in strength are not unexpected because past strength and fatigue testing at elevated temperatures using laboratory specimens showed that the strength of NT551 decreased [1]. Lastly, the Weibull distributions for these four valve strength sets are compared in Fig. 6. It is arguable that the retained strengths of the longitudinally machined valves after 166 hours of engine service are still larger than the strength of the valves whose fillet radius were transversely machined. Fractography was to identify the strength-limiting flaw in the fractured valves in these four sets, and porous regions, dark-shaded inclusions, and machining damage were the active and dominant flaw-types among the sets.

Additional NT551 valve life prediction analyses were completed during the present reporting period. Strength data from two different test specimen geometries (ASTM C1161B and cylindrical bend bars) were used to predict the inert strength failure probability of a NT551 DDC Series 149 valve. As a result of (different types of) inhomogeneities in the strength-limiting flaw populations among the specimens and the valves, the life prediction using input from these two flexure specimen data sets did not correlate well to the measured valve strengths. This result reiterates and emphasizes the requirements that ceramic materials must both have the same uniformly distributed flaw population(s) in the test specimen and the component. Unless material homogeneity exists, *any* meaningful life prediction or reliability analysis of a ceramic component may not be possible.

Caterpillar Test Program

This is a two phase effort. In the first phase, the strength distributions as a function of temperature, grinding orientation, and time (fatigue) of several candidate silicon nitrides will be generated and compared. In phase two (next fiscal year), the better performing one or two silicon nitrides from phase one will be subjected to a more systematic study of the effects of fatigue, temperature, corrosion, and environment on their probabilistic strength.

Currently there are five silicon nitrides involved in the phase one testing: AlliedSignal's AS800 and GS44 (both isopressed), CFI's N7202, and Kennametal's KYON3000 and KYON3500. The present project tested the KYON3000 approximately one year ago; however, Kennametal staffmembers desired to provide new stock material for the bend bar machining and strength testing (earlier supplied billets were "near-net-shape" processed and a desire existed to provide new, thicker billets). Approximately 180 ASTM C1161-B bend bars of each silicon nitride are being flexure tested for strength as a function of temperature, grinding orientation, and time at 850°C (this test condition deemed a worst-case scenario). Lastly, all specimens were commercially finish ground with 320 diamond grit grinding (for both transverse and longitudinal machining orientations) according to recommended practices described in ASTM C1161. All specimens were longitidudinally bevelled. The phase one test matrix is outlined in Table 1, and those sets that were been completed during the present reporting period are indicated.

Comparisons of the 20°C/30MPa•s^{-1}/longitudinal, 20°C/30MPa•s^{-1}/transverse, and 850°C/30MPa•s^{-1}/longitudinal uncensored strength distributions for the isopressed AS800 silicon nitride are illustrated in Figs. 7-8. At 20°C, the inert characteristic strength for the transversely machined specimens was approximately 5% less than for the longitudinally machined specimens. For the longitudinally machined specimens, the 850°C inert characteristic strength decreased by approximately 12%. The observed strength differences were statistically significant within 95% confidence. The uncensored Weibull modulus appeared the highest for the 20°C/30MPas^{-1}/longitudinal set; however, the statistical significance of this was not strong within 95% confidence.

Comparisons of the 20°C/30MPa•s^{-1}/longitudinal, 20°C/30MPa•s^{-1}/transverse, and 850°C/30MPa•s^{-1}/longitudinal uncensored strength distributions for the isopressed GS44 silicon nitride are illustrated in Figs. 9-10. At 20°C, the inert characteristic strength for the transversely machined specimens was approximately 13% less than for the longitudinally machined specimens. For the longitudinally machined specimens, the 850°C inert characteristic strength decreased by approximately 19%. The observed strength differences were statistically significant within 95% confidence. Like the AS800, the uncensored Weibull modulus appeared the highest for the 20°C/30MPas^{-1}/longitudinal set; however, the statistical significance of this was not strong within 95% confidence.

Comparisons of the 20°C/30MPa•s^{-1}/longitudinal, 20°C/30MPa•s^{-1}/transverse, and 850°C/30MPa•s^{-1}/longitudinal uncensored strength distributions for the N7202 silicon nitride are illustrated in Figs. 11-12. At 20°C, the inert characteristic strength for the transversely machined specimens was approximately 12% less than for the longitudinally machined specimens. For the longitudinally machined specimens, the 850°C inert characteristic strength decreased by approximately 11%. The observed strength differences were statistically significant within 95% confidence. Lastly, like both the AS800 and GS44, the uncensored Weibull modulus appeared the highest for the 20°C/30MPas^{-1}/longitudinal set; however, the statistical significance of this was not strong within 95% confidence.

Lastly, as a comparison the 20°C/30MPa•s^{-1}/longitudinal, 20°C/30MPa•s^{-1}/transverse, and 850°C/30MPa•s^{-1}/longitudinal uncensored strength distributions for the NT551 silicon nitride are illustrated in Figs. 13-14 [1]. At 20°C, the inert characteristic strength for the transversely machined specimens was approximately 22% less than for the longitudinally machined specimens. For the longitudinally machined specimens, the 850°C inert characteristic strength decreased by approximately 46%. The observed strength differences were statistically significant within 95% confidence.

Flexure testing is continuing and fractography is planned to identify strength-limiting flaws in the materials and to examine if the different dominant flaw type is changing with machining condition, test temperature, and time at 850°C.

Status of Milestones

All milestones are on schedule.

Communications / Visitors / Travel

- M. Andrews had several communications with AlliedSignal Engines' P. Brehm regarding compiling of the latest versions of CERAMIC and ERICA.
- M. Andrews had several communications with DDC staff regarding the finite element stress analysis of the Series 149 exhaust valve at service conditions.
- NT451 and NT551 data from previous bimonthly reports was provided to Caterpillar engineer Jeff Bougher.
- Valve strength data was provided to Norton's Vimal Pujari and DDC's Yuri Kalish.
- Caterpillar's Raj Tandon visited the HTML on January 11 to discuss strength testing of candidate silicon nitride materials for valve head applications.
- A summary of NT551 flexure strength data was provided to Norton's Vimal Pujari and David Jacobs, DDC's Yuri Kalish, and Caterpillar's Raj Tandon.
- Communications with Kennametal have resulted in the strength testing planning of their KYON3000 and KYON3500 silicon nitrides in support of this project's collaboration with Caterpillar.
- A. A. Wereszczak and M. J. Andrews attended the 23rd Annual Cocoa Beach Conference and Exposition on Composites, January 23-29, 1999. The former served as a session chair on Ceramic Reliability and the latter gave a presentation entitled "Prediction of the Inert Strength Distribution of Si_3N_4 Diesel Valves."
- A. Wereszczak, M. Andrews, and K. Breder visited Saint-Gobain/Norton, Northboro, MA, February 22 to meet with Vimal Pujari and Dave Jacobs about the completion of the NT551 testing.
- R. Yeckley of Kennametal communicated that large billets of KYON3000 and KYON3500 for bend bar machining are currently being sintered and will soon be supplied.

Problems Encountered

None.

Publications

- M. J. Andrews, A. A. Wereszczak, K. Breder, T. P. Kirkland, and M. K. Ferber, "Investigations of the Weibull Modulus as a Function of Stressing Rate," *Ceramic Engineering and Science Proceedings*, Vol. 19, pp. 79-87, 1998.
- A. A. Wereszczak, M. K. Ferber, T. P. Kirkland, A. S. Barnes, E. L. Frome, and M. N. Menon, "Asymmetric Tensile and Compressive Creep Deformation of Hot-Isostatically-Pressed Y_2O_3-Doped Si_3N_4," *Journal of the European Ceramic Society*, **19** 227-237 (1999).
- M. J. Andrews, A. A. Wereszczak, and K. Breder, "Prediction of the Inert Strength Distribution of Si_3N_4 Diesel Valves" In press, *Ceramic Engineering and Science Proceedings*, Vol. 20, 1999.

References

[1] A. A. Wereszczak, M. J. Andrews, T. P. Kirkland, and M. K. Ferber, "Life Prediction Verification," *Ceramic Technology Project Semiannual Technical Progress Report to DOE Office of Transportation Technologies*, Oct 1997 - Mar. 1998.

[2] J. M. Corum, R. L. Battiste, R. C. Gwaltney, and C. R. Luttrell, "Design Analysis and Testing of Ceramic Exhaust Valve for Heavy Duty Diesel Engine," CRADA Y12 92-0088 with Detroit Diesel Corporation, ORNL/TM-13253 (1996).

Table I. Summary of NT551 tensile strength Weibull distributions parameters.

Stressing Rate	Number of specimens tested	Uncensored Weibull modulus [± 95%]	Uncensored Characteristic Strength [± 95%]
30 MPa/s	13	6.7 [4.3, 9.6]	768 MPa [699, 840]
0.3 MPa/s	12	9.4 [5.7, 14.1]	701 MPa [653, 750]
0.003 MPa/s	12	9.2 [5.8, 13.3]	615 MPa [573, 659]

Table 2. Silicon nitride test matrix to compare inert strength, high temperature fatigue performance, and effect of machining orientation. A minimum of twenty-five ASTM C1161B specimens will be (4pt) flexure strength tested per condition.

Test Condition	AS800	GS44	KYON 3000	KYON 3500	N7202
20°C 30 MPa/s Longitudinal	Completed	Completed	X	X	Completed
20°C 30 MPa/s Transverse	Completed	Completed	X	X	Completed
850°C 30 MPa/s Longitudinal	Completed	Completed	X	X	Completed
850°C 30 MPa/s Transverse	X	X	X	X	X
850°C 0.003 MPa/s Longitudinal	X	X	X	X	X
850°C 0.003 MPa/s Transverse	X	X	X	X	X
Material's Manufacturer	AlliedSignal Ceramic Components	AlliedSignal Ceramic Components	Kennametal	Kennametal	CFI

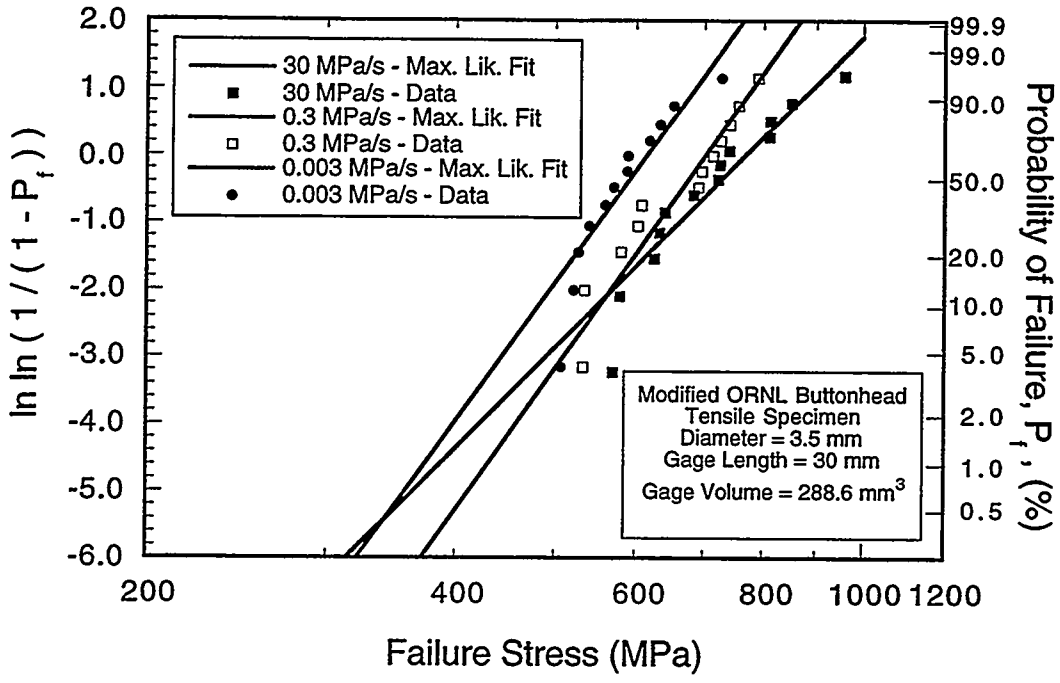

Fig. 1. Comparison of NT551 tensile dynamic fatigue strength distributions.

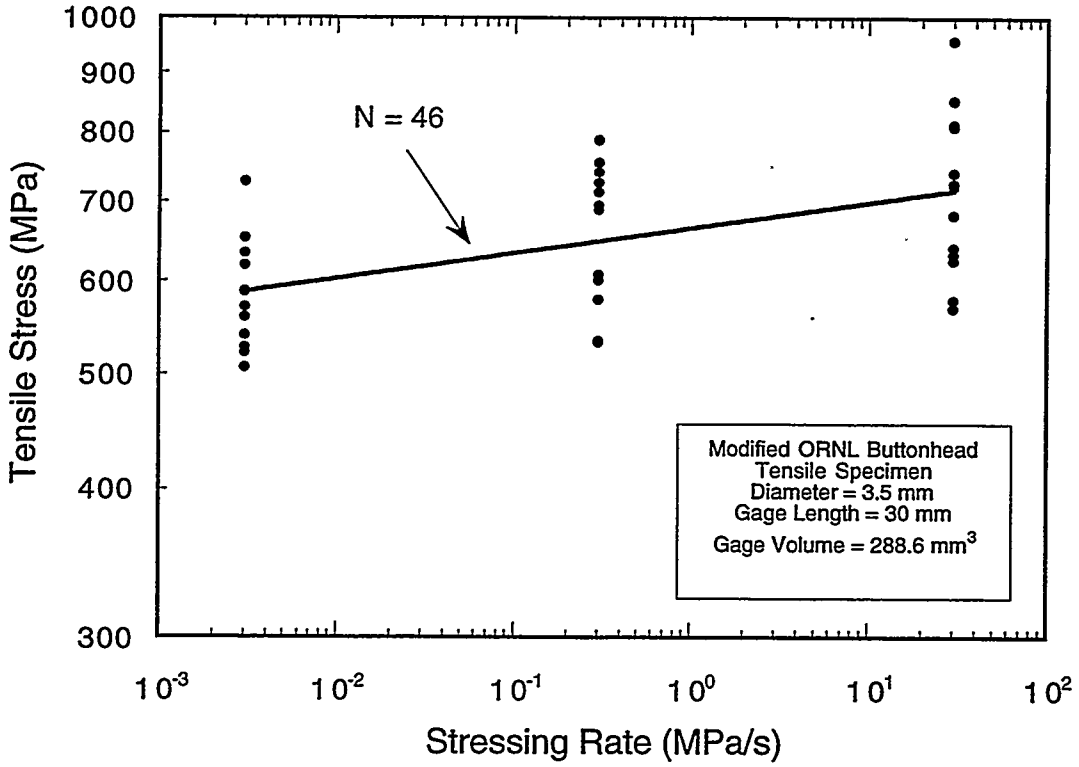

Fig. 2. The fatigue exponent for the NT551 tensile strengths was 46.

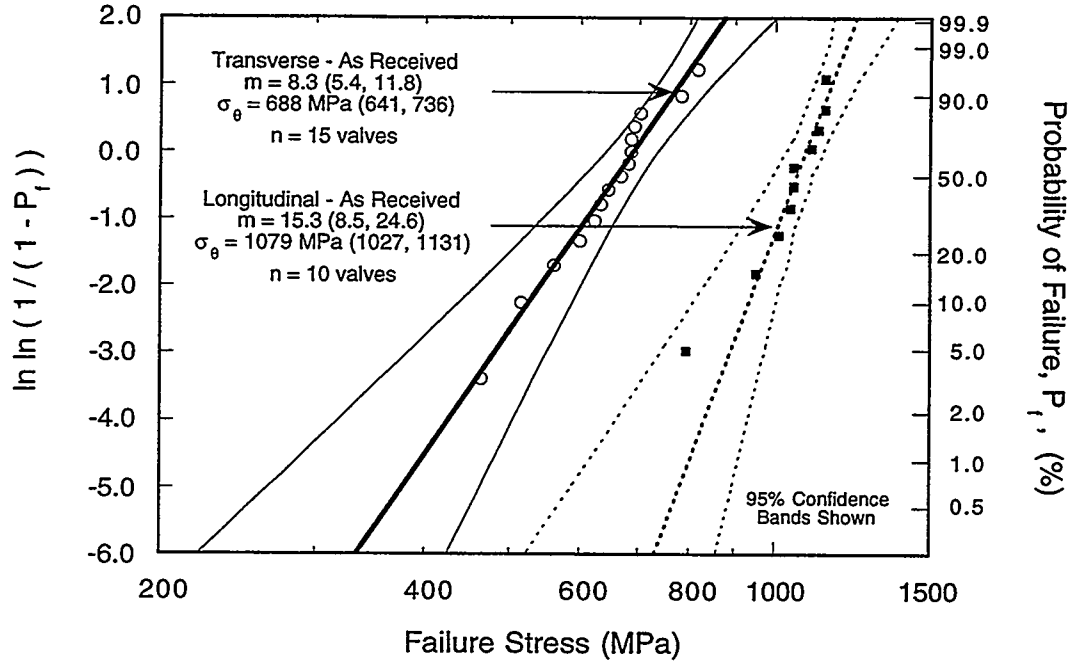

Fig. 3. Comparison of as-received NT551 valve strengths as a function of how their fillet radius was machined.

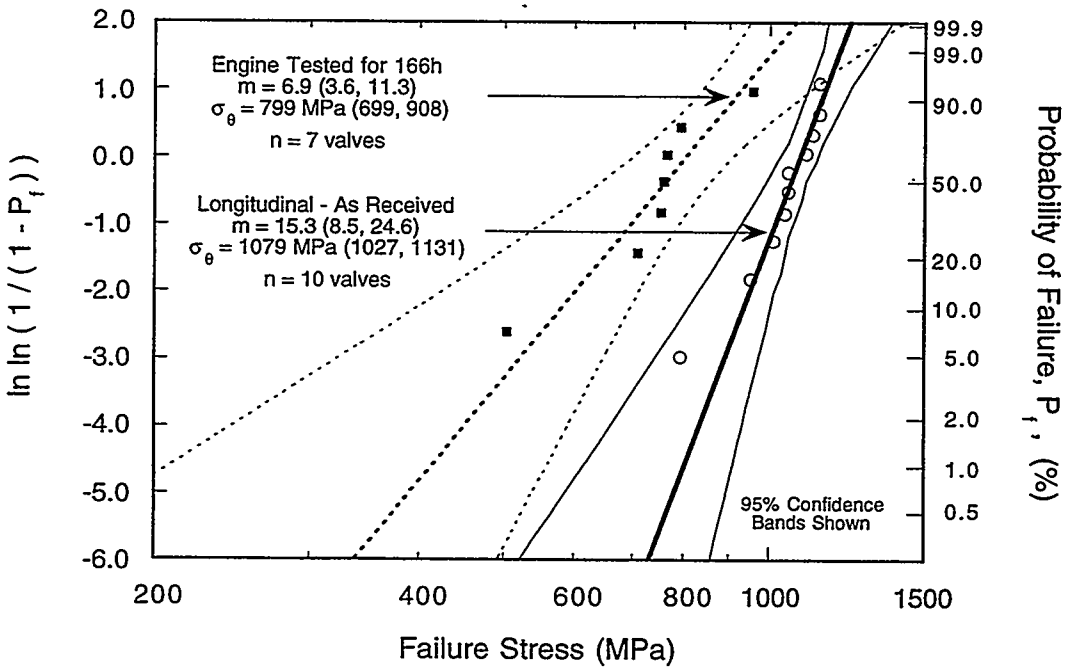

Fig. 4. Strength distribution comparison of NT551 valves that were longitudinally machined (before and after engine testing).

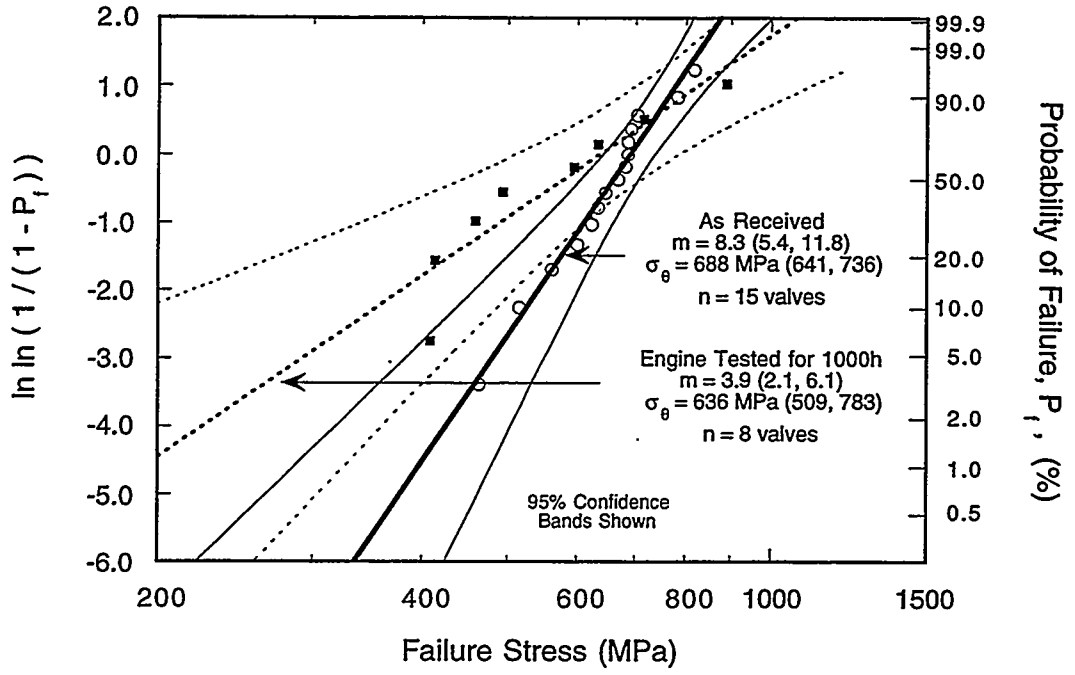

Fig. 5. Strength distribution comparison of NT551 valves that were transversely machined (before and after engine testing).

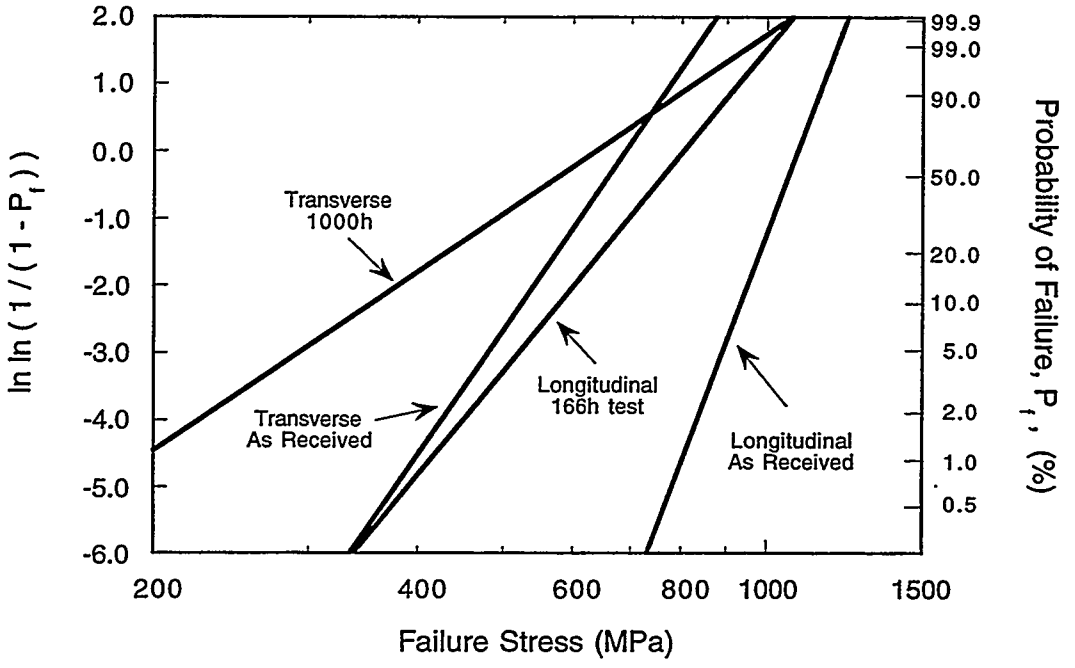

Fig. 6. Strength distribution comparison of the four NT551 valve sets shown in Figs. 3-5.

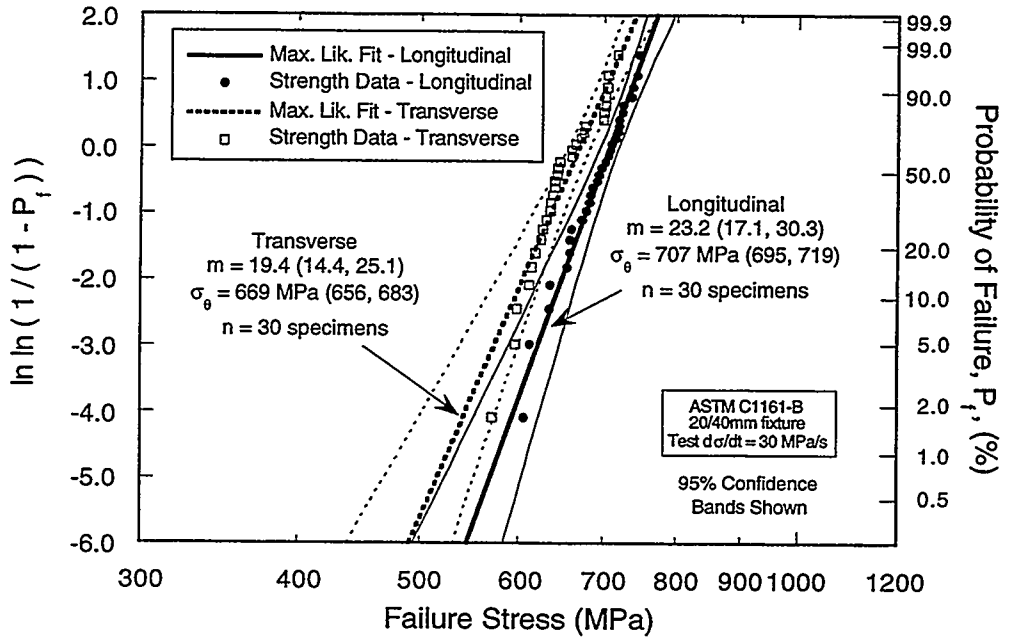

Figure 7. Comparison of 20°C inert flexure strength distributions for longitudinally and transversely machined AS800.

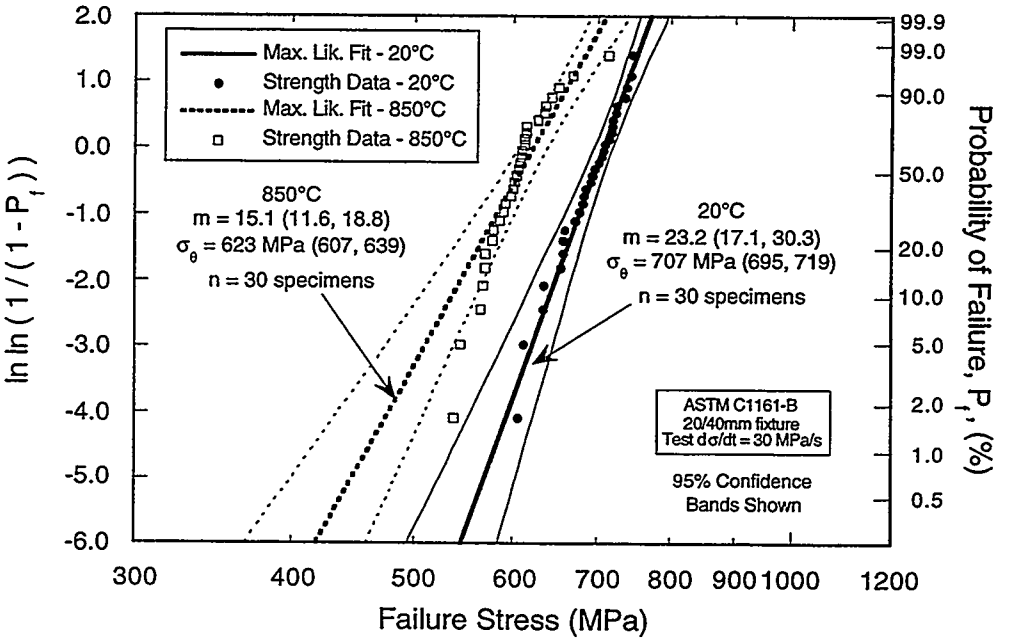

Figure 8. Comparison of 20 and 850°C inert flexure strength distributions for longitudinally machined AS800.

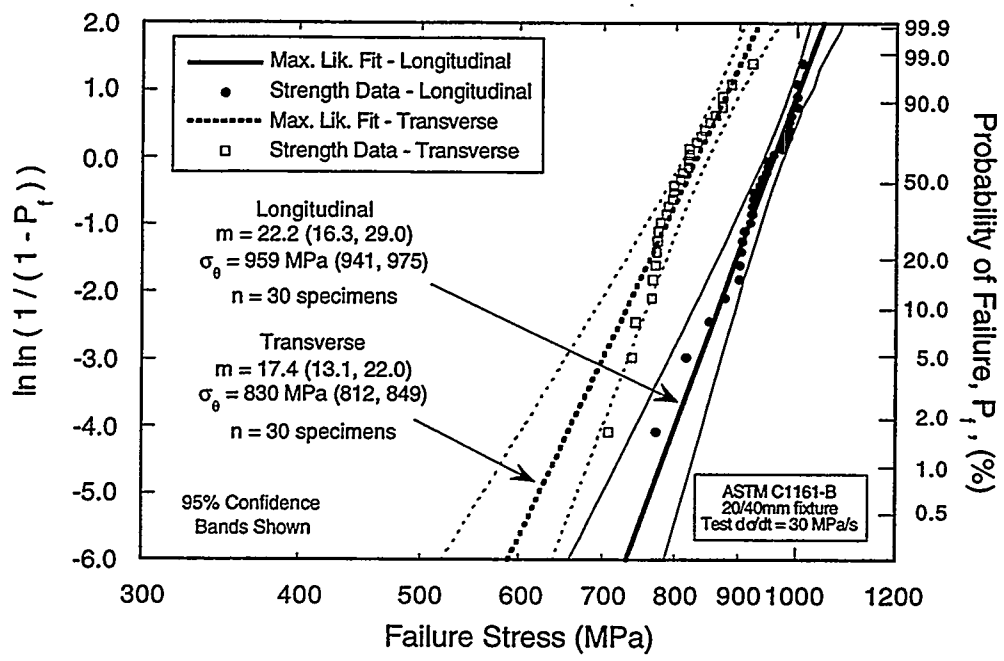

Figure 9. Comparison of 20°C inert flexure strength distributions for longitudinally and transversely machined GS44.

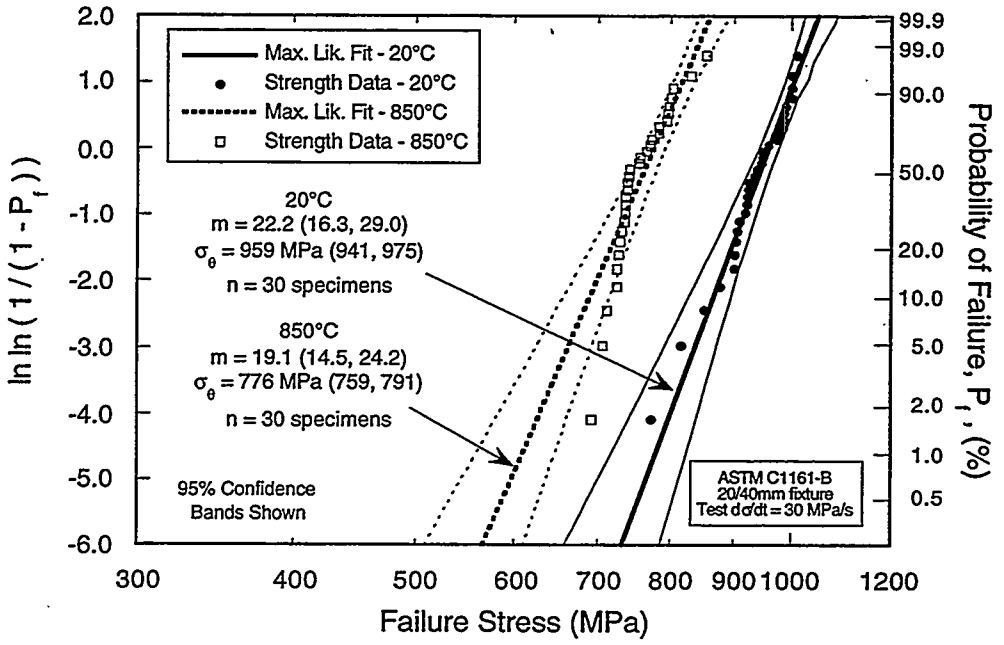

Figure 10. Comparison of 20 and 850°C inert flexure strength distributions for longitudinally machined GS44.

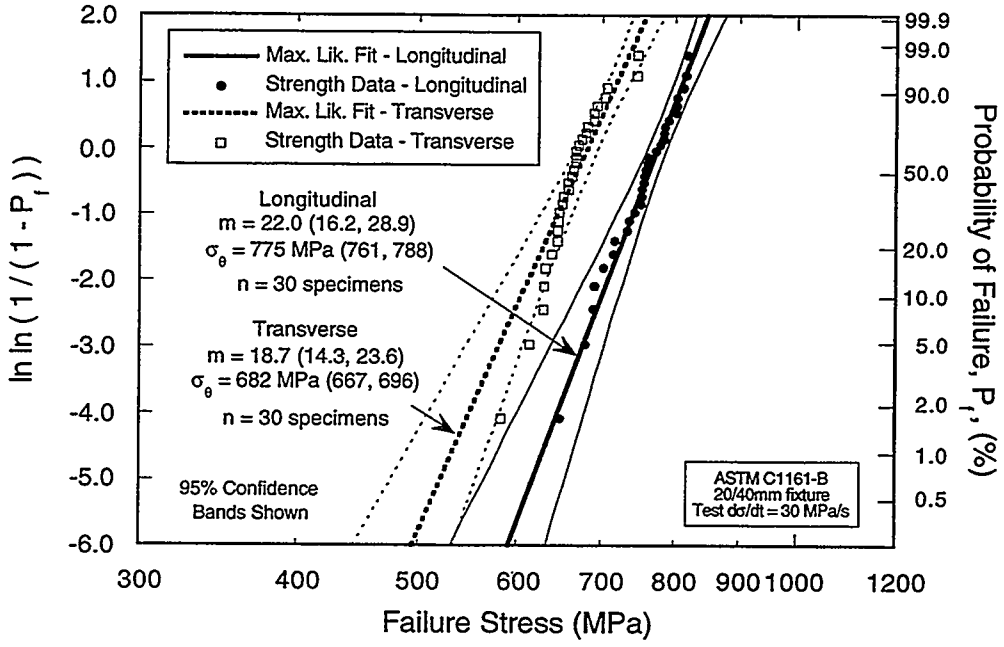

Figure 11. Comparison of 20°C inert flexure strength distributions for longitudinally and transversely machined N7202.

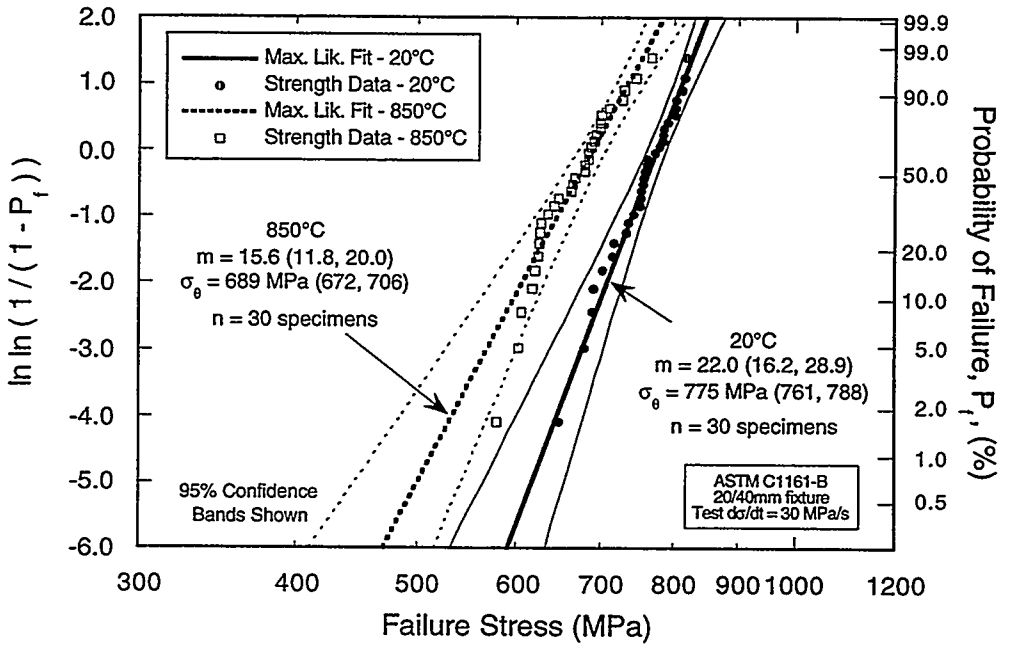

Figure 12. Comparison of 20 and 850°C inert flexure strength distributions for longitudinally machined N7202.

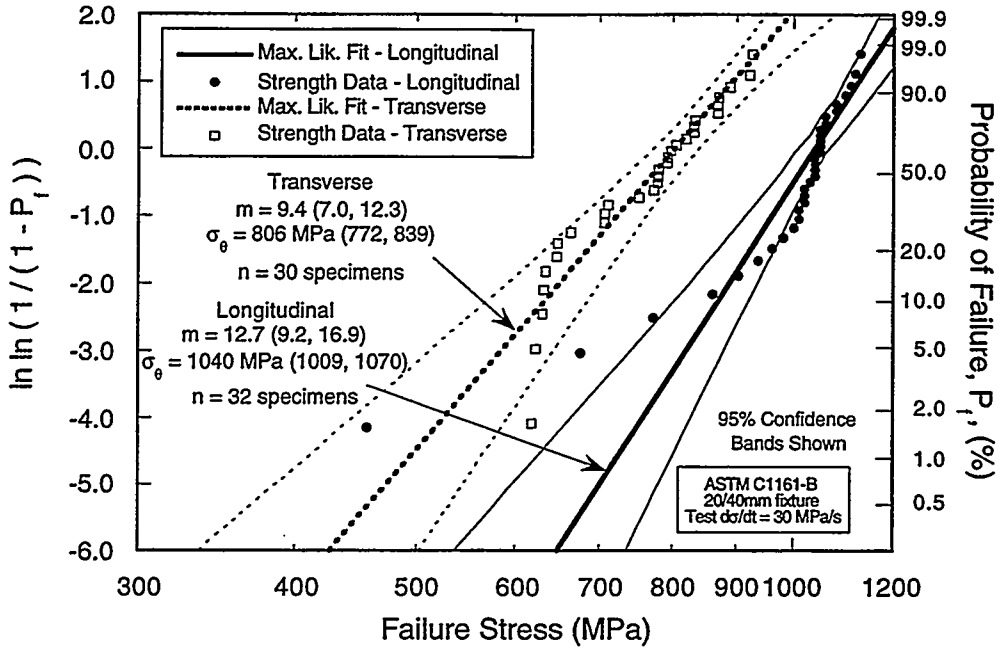

Figure 13. Comparison of 20°C inert flexure strength distributions for longitudinally and transversely machined NT551 [1].

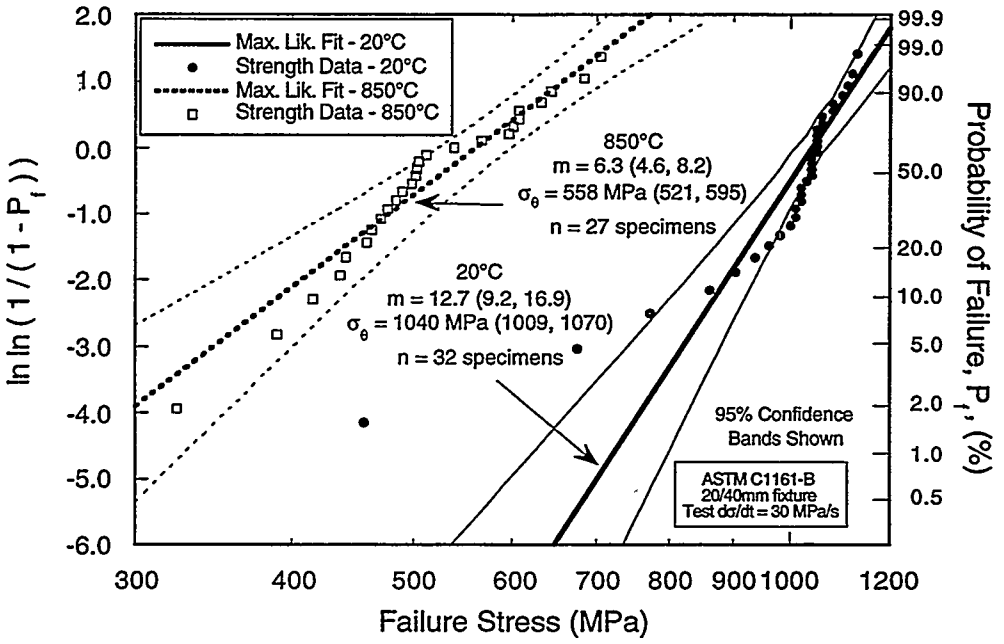

Figure 14. Comparison of 20 and 850°C inert flexure strength distributions for longitudinally machined NT551 [1].

Field Emission Analytical Electron Microscopy for Characterization of Catalyst Microstructures

L. F. Allard and T. A. Nolan

OBJECTIVE/SCOPE

The objective of the research is to use analytical and high resolution transmission electron microscopy (TEM) to characterize the microstructures of emission control catalysts. Emphasis is placed on relating microstructural changes to performance of diesel NOx reduction catalysts. The research is focussed on understanding these changes through TEM studies of experimental catalysts materials reacted in an ex-situ catalyst reactor system especially constructed to allow appropriate control of the reaction conditions and the transfer of the sample between reactor and microscope.

TECHNICAL HIGHLIGHTS

Materials studied

Work has been conducted, using the HF-2000 field emission TEM, on two different catalyst systems which have application to reduction of NOx emissions. A fundamental study of a new series of experimental catalyst materials was begun with Prof. Bruce Gates and his students at UCal-Davis, to better understand the characteristics (i.e. dispersion, size, behavior during reactions) of very small clusters of heavy metal species on several different oxide support materials. These include Os/MgO, Rh/TiO_2, and Ir/Al_2O_3. Characterization has also begun on a series of experimental catalysts comprising silica-alumina mixtures as supports for platinum as the active catalyzing species. The support materials for this study (in conjunction with colleagues at Ford Research Laboratory, Dearborn, MI) were produced by a sol-gel processing technique, described in detail in the referenced publication. Earlier studies at Ford of sol-gel materials processed for automotive applications showed there was a significant positive effect for NOx reduction when silver was used as the active species on sol-gel-prepared alumina compared to silver deposited on commercial γ-alumina, in the temperature range 475-525°C. The present study was initiated to improve the NOx conversion efficiency and the hydrothermal stability of the Pt/Al_2O_3 system by incorporating silicon in the alumina matrix.

Fine cluster work

Heavy metal species were characterized initially by a variety of techniques that have shown, for example, that Os carbonyl species on MgO form nearly exclusively as clusters containing 5 atoms of Os in both a carbonyl form ($Os_5(CO)_{14}$) and when decarbonylated by treatment in He at elevated temperatures. The goal of the TEM study was to determine first whether these fine clusters could be reliably imaged with the HF-2000, whether the Os could be detected by energy dispersive spectroscopy, and finally how uniformly were the Os clusters dispersed over the MgO support material.

In addition to the HF-2000 results, the same material was examined recently in a new dedicated scanning transmission electron microscope (STEM), the HD-2000, being offered commercially by Hitachi Co. This instrument allowed recording of both bright-field and high-angle annular dark-field images. Figure 1a is an image from the HF-2000 of the Os-carbonyl clusters on the MgO support, illustrating that these clusters containing so few atoms can indeed be imaged by the TEM. However, it was not possible with the HF-2000 EDS system to detect Os in the EDS spectrum from only a few clusters. Results from the dedicated STEM were more promising. For example, Fig.1b is a typical dark-field image, taken using the high-angle annular detector on the instrument, which records the intensity scattered at high angles from the higher atomic number species in

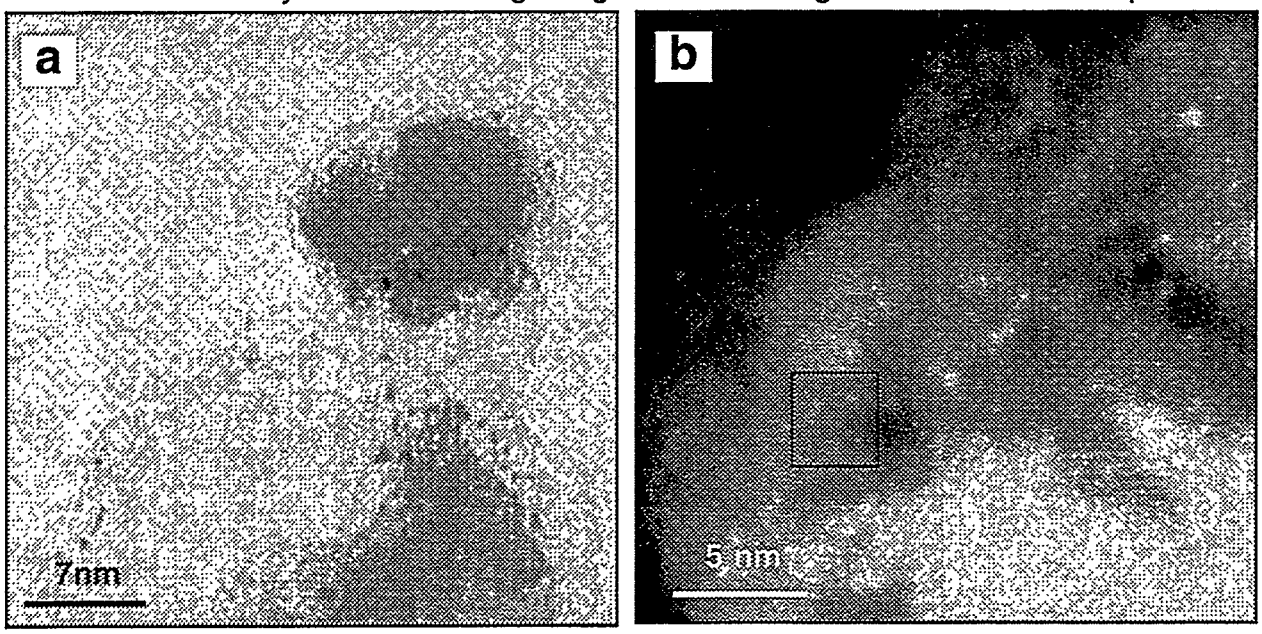

Fig. 1 a) Bright-field FE-TEM image of 5-atom Os-carbonyl clusters on MgO b) Similar image taken in high-angle annular dark-field using the Hitachi dedicated STEM. EDS spectrum from area indicated (only a few clusters) showed presence of Os.

the sample, showing the clusters in bright contrast. In a 30 s acquisition, an EDS spectrum from a few clusters showed a clear Os peak, further confirming that the image

features are indeed the expected Os clusters. Similar results were obtained from both the Ir/Al2O3 and the Rh/TiO2 systems.

Pt/silica-alumina studies

Three catalysts were prepared, comprising 1% Pt on 10, 30 and 50% SiO_2 in Al_2O_3. They exhibited respectively 52, 57 and 38% conversion efficiency for NOx, versus 45% for 1% Pt on standard gamma-alumina. Because of their large differences in conversion efficiency, transmission electron micrographs of the 30% and 50% SiO_2 samples are shown in Fig. 2a and 2b. Both samples show nearly the same support particle morphology, acicular particles on the order of 3-5nm x 20-25nm. The Pt species was not directly visible in the TEM images, suggesting a near-atomic level dispersion on both specimens. Pt can, however, be detected in an energy dispersive x-ray spectrum acquired with a long counting time. The difference in conversion efficiencies between the 30 and 50% SiO_2 samples may be related to the relative surface acidity as controlled by the change between Si incorporated in the alumina structure at low percentage SiO_2 to SiO_2 becoming the dominant species at the 50% SiO_2 level. A reduced contact of Pt with Brønsted acid sites causes a reduction in the NOx conversion efficiency.

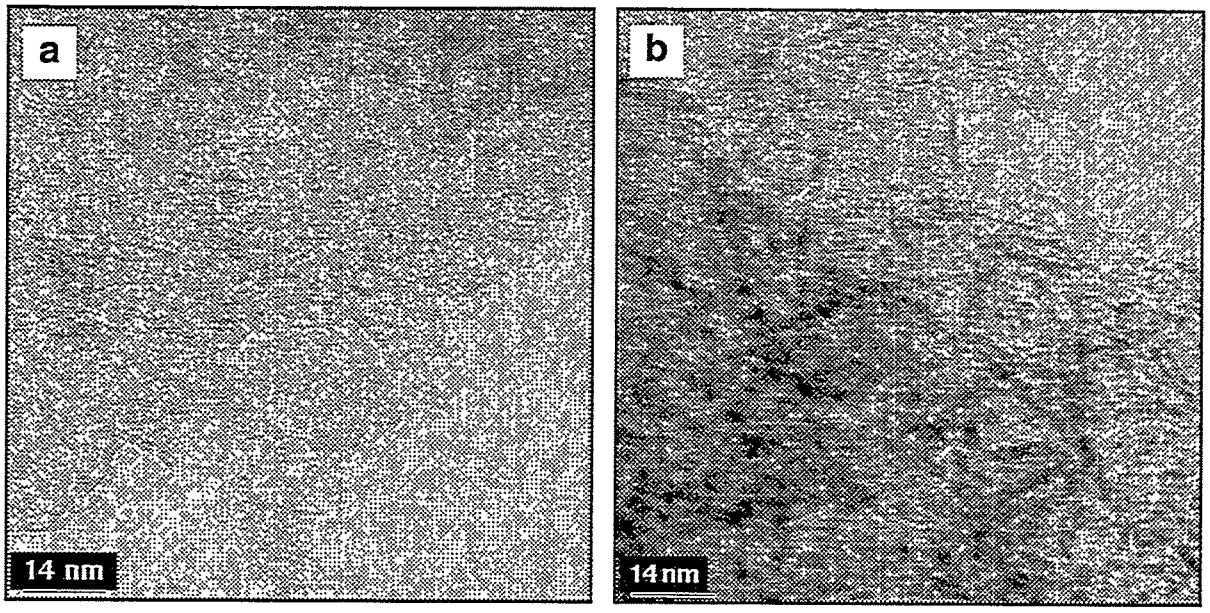

Fig. 2 a) Sol-gel processed 30%SiO_2/Al_2O_3 catalyst with 1%Pt loading, showing acicular support particles but no discretely visible Pt species. b) 50% SiO_2/Al_2O_3 sample shows similar support morphology and also no visible Pt clusters.

PUBLICATIONS

C. K. Narula, M. Rokosz, L. F. Allard, R. K. Kudla and M. S. Chattha, "Sol-Gel Processed Silica-Alumina Materials for Diesel Engine Emissions Reduction Catalysts," submitted to Langmuir, April 1999.

MATERIALS AND TESTING STANDARDS

IEA ANNEX II Management (October 1, 1998-March 31, 1999)

M. K. Ferber and K. Breder (Oak Ridge National Laboratory)

Objective/Scope

The purpose of this task is to organize, assist, and facilitate international research cooperation on the characterization of advanced structural ceramic materials. A major objective of this research is the evolution of measurement standards. This task, which is managed in the United States by ORNL, now includes a formal IEA Annex agreement identified as Annex II between the United States, Germany, Sweden, Japan, and Belgium. The original annex included four subtasks: (1) information exchange, (2) ceramic powder characterization, (3) ceramic chemical and physical characterization, and (4) ceramic mechanical property measurements. In the United States, a total of 13 industrial and government laboratories have participated and contributed their resources to this research. The research in Subtasks 2, 3, and 4 is now complete. In 1990, research in two new subtasks was initiated, including Subtask 5, Tensile and Flexural Properties of Ceramics, and Subtask 6, Advanced Ceramic Powder Characterization. The research in Subtasks 5 and 6 was completed in 1993 and the reports were distributed. Two new tasks (Subtask 7 on Ceramic Machining and Subtask 8 on Ceramic Powder Characterization) were proposed in late FY 1993 and the research is completed (1996). Subtask 7 in the United States included eight companies and three federal laboratories. The report on the results from research performed in the United States on Subtask 7 is complete (the final report of all the international research has been published and distributed). Subtask 8 included six companies. The final report for Subtask 8 is complete. In 1996, research in two new subtasks was initiated, including Subtask 9 - Thermal Shock and Subtask 10 - Ceramic Powder Characterization, and work in these subtasks is presently ongoing.

Recent Developments

The IEA Annex II Executive Committee Meeting was held at Siemens ZT München-Perlach, Germany, October 16, 1998. A brief summary follows.

The meeting of the Executive Committee of the IEA Annex II, IEA Cooperative Programme on Ceramics for Advanced Engines and Other Conservation Applications, was held on 16 October 1998, at Siemens ZT München-Perlach, Germany. There were 15 people in attendance including the Executive Committee members listed below.

Dr. Eberhard Seitz	-	German Executive Committee Member
Dr. Hideaki Kitamura	-	Japanese Alternate Executive Committee Member
Mr. Erik Skog	-	Swedish Executive Committee Member
Robert Pompe	-	Alternate Swedish Executive Committee Member

Eberhard Seitz - Meeting Chairman and German Executive Committee Member, opened the meeting by thanking Siemens for hosting us. Dr. Seitz briefly summarized the session on International Collaboration in the conference Werkstoffwoche held the previous day and thanked Dr. Michael Landwehr and Dr. Kristin Breder for presenting our IEA work at the conference.

Dr. Seitz then introduced the German delegation.

Erik Skog - Swedish Executive Committee Member. Mr. Skog takes over for the previous NUTEK representatives. Mr. Skog is from the company Sydkraft (a utility) and is the chairman of the board of a new consortium for Material Technologies for Thermal energy Processes (KME) funded by The Swedish National Energy Administration (SEA), which is now separated from NUTEK, and by Swedish Industry.

Robert Pompe SCI is the alternate Swedish Executive Committee Member and Swedish Coordinator of Subtask 10.

Robert Gilissen - Belgian Coordinator of Subtask 10 represented Belgium at the meeting.

Hideaki Kitamura - Japanese alternate Executive Committee Member introduced the Japanese delegation.

Kristin Breder - U.S. Coordinator of Subtask 9 represented the United States at the meeting.

Michael Landwehr - IEA representative for the present Implementing Agreement. Mr. Landwehr commented on the participation and representation of the various countries and clarified that as long as a country is member of the Implementing Agreement (IA) they should be represented at the Executive Committee Meetings. This is the case even if a country is not currently participating in the active annex or subtask.

Each country distributed reports as part of the information exchange.

The status of Subtask 9 was presented by Drs. Breder, Rettig, Kirchhoff, Mizuno, and Gilissen. It was decided that testing will be completed by January 1999. Each country will submit a report to Dr. Ferber and a draft report will be compiled by the United States and distributed by the end of March and the final report will be distributed at the end of June 1999.

The status of Subtask 10 was presented by Dr. Gilissen on behalf of the group. All data should be submitted to NIST by January 1999 and they will compile a draft report. The draft report will be distributed at the end of March and the final report will be distributed at the end of June 1999.

There was discussion regarding the current Annex II, Amendment No. 3. The Executive committee voted to change the end date of Annex II, Amendment No. 3 to read July 31, 1999 in order to close the work. A revised Amendment No. 3 will be written and will become Version 6.

Under new business there was discussion regarding future collaboration under the current Annex II rather than pursue a new Implementing Agreement.

Dr. Seitz announced that Forschungszentrum Jülich would no longer be the contracting party for Germany in this IA. Dr. Wäsche, Federal Institute for Materials Research and Testing, BAM, Berlin, will become the new contracting party.

The next Executive Committee meeting will be held in Paris during the first week of October 1999.

The minutes from the Executive Committee Meeting of October 16, 1998, at Siemens ZT München-Perlach, Germany, were sent on February 23, 1999. With this mailing, copies of the August and November 1998 issues of the "Science & Technology Highlights," published by ORNL's Energy Efficiency and Renewable Energy Program were sent as part of the Subtask 1, Information Exchange.

Current Subtask 9 Technical Efforts

Received 87 more disks of Kyocera SN282 which had been prepared by Chand Associates (February 1999). On February 23, 40 disks (Kyocera SN282 silicon nitride) were sent to Dr. Lennart Carlsson for testing. He will thermal shock 20 and hold the remaining 20 for possible thermal fatigue studies.

Twenty SN282 silicon nitride disks were thermally fractured using the apparatus shown in Fig. 1. For each specimen, a series of 12 bit images (256 by 256) was collected at a rate of 10 frames per second. A standard VCR (8 bit-30 frames/second) also captured each fracture test. Figure 2 illustrates a typical series of images generated for Specimen 46 while Fig. 3 provides the associated temperature profiles. These data are being analyzed to determine the thermal fracture stress.

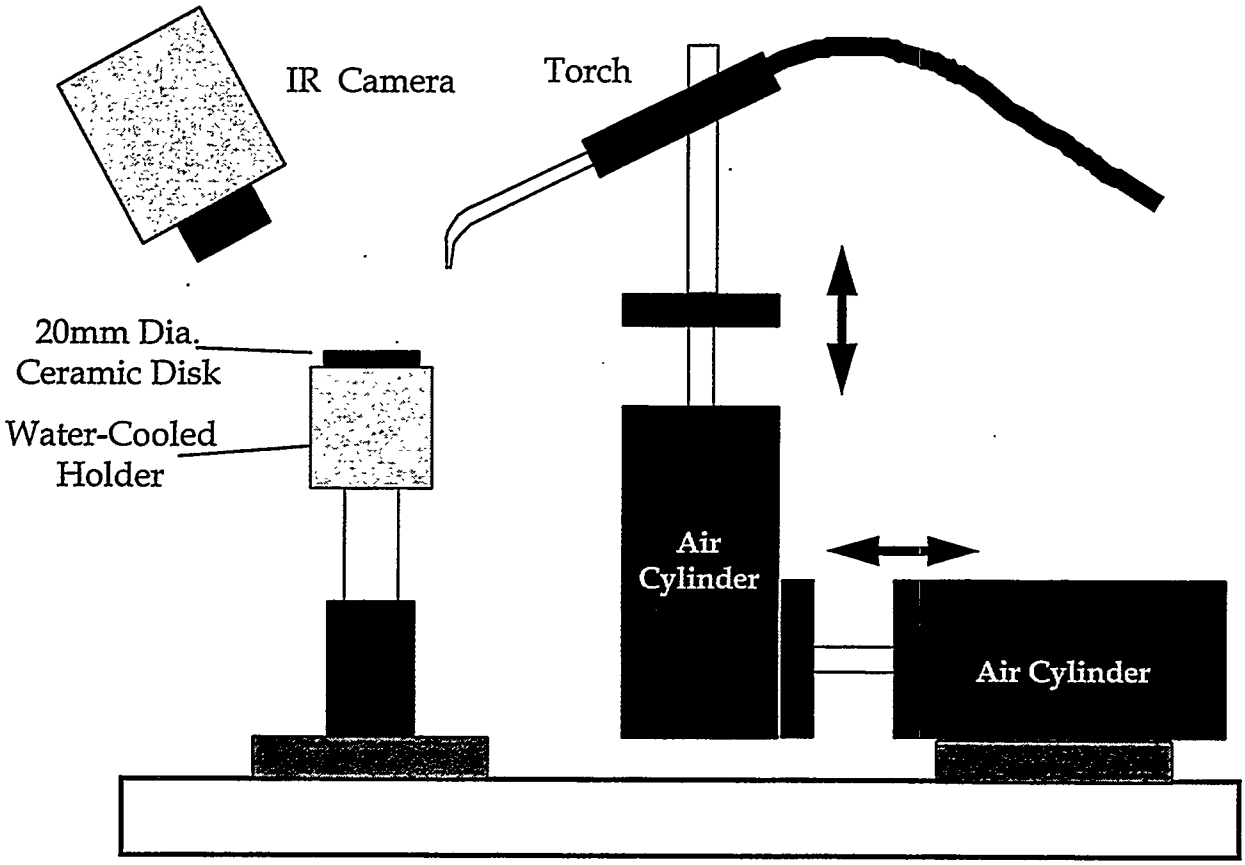

Fig. 1. Schematic representation of thermal shock setup.

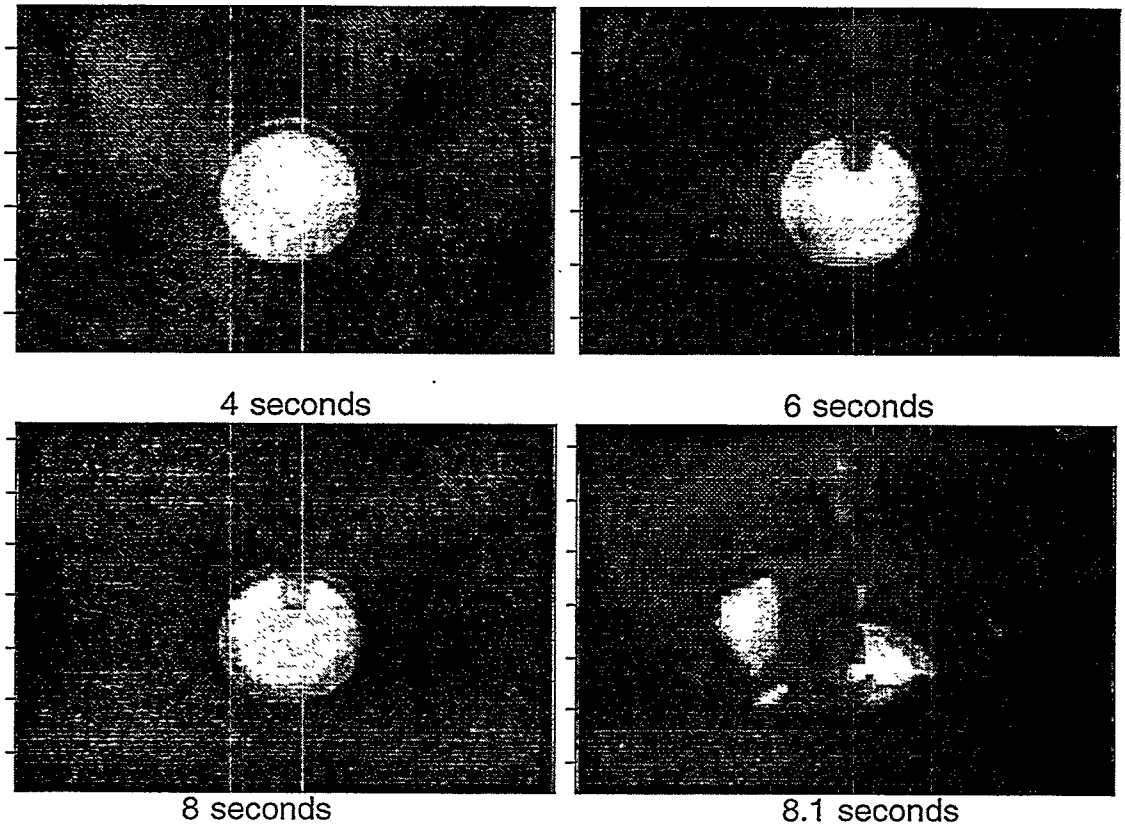

Fig. 2. IR images generated during thermal fracture of SN282 Specimen 46.

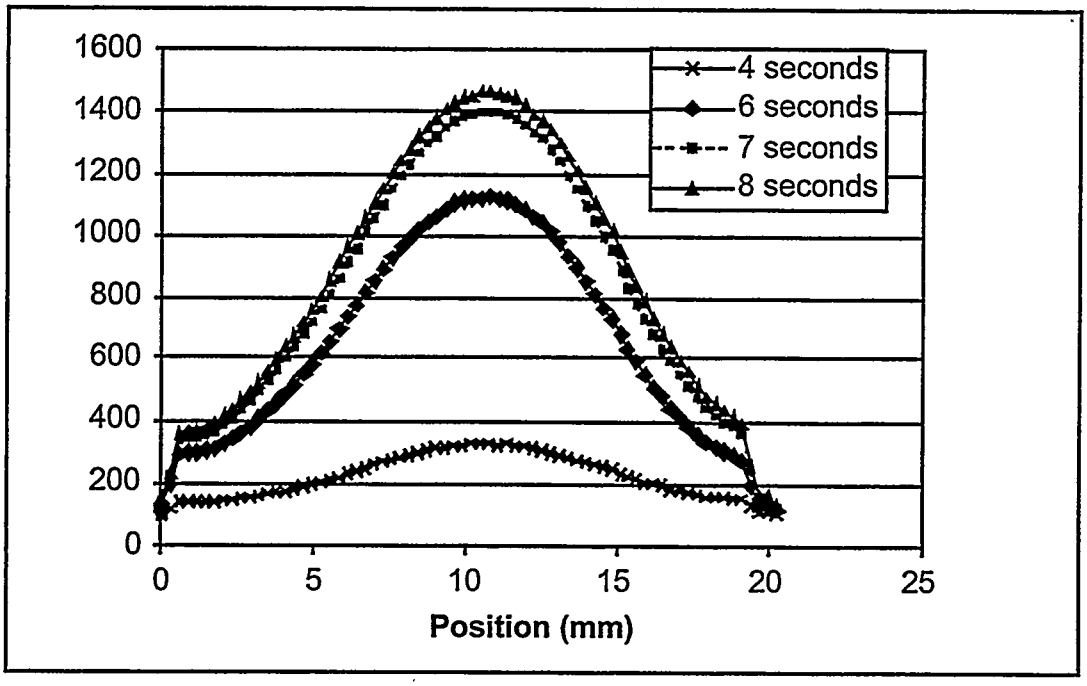

Fig. 3. Temperature profiles associated with the thermal fracture of SN282 Specimen 46.

Subtask 10, Characterizing Ceramic Powders

Major responsibility for this subtask in the United States is at NIST, and a detailed report of progress in these subtasks is provided in the section of this report submitted by NIST.

Status of Milestones - Milestones are on schedule

Communications/Visits/Travel - Kristin Breder attended the Congress Werkstoffwoche '98 held in Munich, Germany, and the IEA Annex II Executive Committee Meeting on October 16, 1998.

Publications and Presentations - Breder, Kristin and Mattison Ferber, "International Energy Agency, Cooperation on High Temperature Structural Ceramics," presented at Congress Werkstoffwoche '98, München, Germany, October 15, 1998.

NDE Standards for Advanced Ceramics

R. W. McClung

The development of standards is important for the establishment of reliability and acceptance of advanced structural materials. Committee C-28, on Advanced Ceramics, has been organized in the American Society for Testing and Materials (ASTM) to address this issue. One of the activities of the C-28 committee is nondestructive examination (NDE). The Section C-28.02.02 on NDE is reviewing existing standards on NDE (primarily developed for metals) to determine potential applicability for ceramics, as well as drafting original standards. Use of existing or modified standards, if available, is more efficient that generation of new documents and will assure the input of a large body of NDE expertise. Close liaison has been established with ASTM Committee E-7 on Nondestructive Testing, and documents are in various stages of review, recommendations for change, modification, and balloting.
R. W. McClung is a subcommittee chairman in both committees and the official liaison.

Technical Highlights

Liaison and technical support have been continued between ASTM committees C-28 and E-7. To date, 50 E-7 NDE standards identified as having potential relevance to ceramics have been reviewed in detail with recommendations made to E-7 for modifications to identified documents. Successful action is complete on 39 documents; three are being addressed by E-7; others require action by C-28. C-28 standard, C-1175, the guide to existing NDE standards, currently contains relevant information on 30 standards that were approved for incorporation; six additional standards are being balloted in C-28 for adding to C-1175 (see below).

A limited amount of data has been identified for establishing radiographic equivalence factors for advanced ceramics. Additional specimens will be sought for experimental radiography to develop additional data. A volunteer for the radiography has been recognized. The intent of this action is to provide data for a table in an E-7 standard E-94 on the radiographic method. Other work in progress includes an amplified outline for a draft standard for reference specimens containing laser-drilled holes and a possible standard on determination of porosity in ceramics using ultrasonic velocity. In addition, interest has been indicated in potential standards for reference specimens for surface flaws and high-resolution penetrant examination.

A revision to C-1175, the guide to existing NDE standards applicable to advanced ceramics, was balloted successfully at both subcommittee and committee levels. The revision incorporated relevant information from E-7 standard E-1817, Controlling Quality of Radiological Examination Using Representative Quality Indicators (RQIs). The revision was approved by ASTM on January 10, 1999.

Following an affirmative advisory ballot (opinion poll) of Committee C-28 conducted on the advisability of adding relevant information on acoustic emission (AE) standards to C-1175, an advisory ballot was conducted in Section C-28.02.02 to provide detailed review of selected

AE standards to determine applicability to advanced ceramics (or recommended modifications to the standards to make them applicable). The E-7 standards on AE included were E-569, Practice for Acoustic Emission Monitoring of Structures During Controlled Stimulation; E-650, Guide for Mounting Piezoelectric Acoustic Emission Sensors; E-750, Practice for Characterizing Acoustic Emission Instrumentation; E-976, Guide for Determining the Reproducibility of Acoustic Emission Sensor Response; E-1106, Method for Primary Calibration of Acoustic Emission Sensors; E-1781, Practice for Secondary Calibration of Acoustic Emission Sensors. The advisory ballot of Section C-28.02.02 resulted in affirmative ballots on each of the six standards with a few minor comments on each. Based on the advisory ballot, a revision to C-1175 incorporating appropriate technical information on each of the six standards was prepared. During the January 1999 meeting of C-28 (see below), approval was obtained for a concurrent subcommittee/committee ballot. The ballot was initiated in this report period for completion in April 1999. Collated comments on the six standards developed during the advisory ballot of C-28.02.02 have been sent to the chairman of the E-7 subcommittee on AE with a recommendation for modification to the standards.

A number of new or revised E-7 NDE standards with current or potential relevance to ceramics were reviewed and comments prepared on E-7 committee and subcommittee ballots. On the committee ballot were four standards on radiology: a revision to a guide for computed radiology, a revision to a practice for computed tomography (based on comments from Committee C-28), a new standard on image unsharpness in radiology, and new definitions of terms for radiology. Also on the committee ballot were revisions of five standards for liquid penetrant examination, revisions of two standards for acoustic emission (AE) sensors, new definitions for AE terms, and three standards for ultrasonics. The ultrasonic standards included a revision to a standard on detection of flaws by immersed techniques (based on recommendations from C-28), revision to a standard on ultrasonic search units, and a new standard on resonance ultrasonic spectroscopy. The revised standards are currently incorporated in C-1175 or are being considered for addition.

The subcommittee ballots included a new standard on verifying consistency of AE sensor response, and revisions to standards on ultrasonic angle-beam examination with contact techniques, and a guide for evaluating characteristics of search units. The latter two are incorporated in C-1175.

During the report period (in December 1998), a proof copy of a manuscript of a prior revision to C-1175 was received from ASTM, reviewed, corrected, and approved for publication in the next edition of Volume 15.01 of the ASTM Book of Standards to be published in March 1999. The revision which was approved by ASTM in December 1997 added technical information (scope, summary, and significance and use) about five additional standards from Committee E-7.

The five standards were:

E-94	Guide for Radiographic Testing
E-1570	Practice for Computed Tomograph (CT) Examination
E-1647	Practice for Determining Contrast Sensitivity in Radioscopy

E-1672	Guide to Computed Tomography (CT) System Selection
E-1695	Test Method for Measurement of Computed Tomography (CT) System Performance

During meetings of Committee E-7 in Fort Lauderdale, Florida, January 17-21, 1999, participation by McClung as C-28 liaison included meetings of the subcommittees on radiology and ultrasonics. Significant activity is ongoing in both subcommittees that will result in standards of interest and value for advanced ceramics. Several of the revisions and ballots are based, in part, on requests from C-28. Radiological standards in various stages of drafting, revisions or balloting include standards for image quality response of film at low (X-ray) energies, a revision to a guide for radiography, computed tomography (CT) examination (in addition, a standard on volumetric CT is planned), radioscopy (to add new detectors), procedures for transition from film radiography to real-time radioscopy, and several standards on computed radiology (a guide and a practice for examination procedures, and a practice for qualification of computed radiology systems). Several standards on radiology from E-7 are progressing as international standards as part of the international committee ISO/TC-135 on NDE.

Subcommittee E7.06 on Ultrasonic Methods has many standards in different stages of preparation or ballot including responses to requests from C-28. Among ultrasonic standards in process relevant to advanced ceramics are those for resonant ultrasonic spectroscopy (passed committee ballot) (currently used for ceramic bearings and other materials), ultrasonic examination using longitudinal waves, detection and evaluation of discontinuities with longitudinal waves (balloted in direct cooperative response to reviews and comments from C-28), time-of-flight flaw sizing techniques, characterization of examination systems, digital data transfer, and angle-beam examination by contact methods. A version of at least five E-7 standards on ultrasonics are in various stages of approval as international standards as part of the international committee ISO/TC-135.

In addition to these activities of the subcommittees on radiology and ultrasonics, several items were noted relevant to advanced ceramics in reports from other subcommittees during the plenary meeting of Committee E-7. The subcommittee on reference radiological images is working on a standard for visual acuity images to test the capability of radiographic examiners. The subcommittee on liquid penetrants is balloting revisions to five standards on liquid penetrant examination that are discussed in C-1175. The subcommittee on acoustic emission (AE) is revising several standards including that on reproducibility of sensor response that (as noted above) is being proposed for addition to C-1175.

During meetings of C-28 in Cocoa Beach, Florida, January 22-24, 1999, the action items related to revisions of C-1175 noted above were reported and discussed. Approval was obtained for the ongoing concurrent subcommittee/committee ballot on the revision incorporating technical information on six AE standards.

IEA Subtask 10 – **Ceramic Characterization and Standards for Heat Engines**

Lin-Sien Lum
National Institute of Standards and Technology
Bldg 223, Room A256, Div. 852
Gaithersburg, MD 20899

Objective/Scope

The objective of Subtask 10 is to tighten and finalize procedures for the characterization of secondary properties of powders. There are four focus areas relating to the secondary properties: dispersion of powders for slurry preparation, slurry preparation, spray dried powders and green body evaluation.

Subtask 10 involves participants from Belgium, Germany, Japan, Sweden, and the United States.

Technical Progress

The packaging and distribution of the powder samples to the round robin participants have been completed. The powders came from commercial sources to avoid problems associated with pilot size spray dryers and also to improve the quality of the samples. The pellets for the green body characterization were fabricated by VITO in Belgium from similar spray dried powders. Both the powder samples and the green body pellets have been shipped to the participants for analysis.

The data from the round robin will be compiled in a database. The entry modules for this database are in the design stages. The database is designed using Microsoft Access. Each entry module will contain the information on the powder or green body sample. Information on the procedure used and the data collected will also be included. Testing on the modules will begin soon. Round robin testing is continuing for all the participants. The entry of the data for the database will begin after the arrival of the data from the participants.

Milestones

The next Subtask 10 technical leader's meeting will be in Indianapolis, Indiana, on April 27 at the annual meeting of the American Ceramics Society.

Complete round robin testing by participants- 6/99
Data entry module completion--6/99
Data analysis and final report--9/99

Communications/Visits/Travel –
None

Publications/Presentations -
None

Reference –
None

Problems Encountered –
None

Ceramic Mechanical Property Test Method Development

George D. Quinn (National Institute of Standards and Technology)

Objective/Scope

This task is to develop mechanical test method standards in support of the Propulsion Systems Materials Program. The test methods should meet the needs of the DOE engine community but should also consider the general USA structural ceramics community as well as foreign laboratories and companies. Draft recommendations for practices or procedures shall be developed based upon the needs identified above and circulated within the DOE ceramics engine community for review and modification. Round-robins will be conducted as necessary, but shall be well-focused, limited in scope, and complementary to IEA round-robins. Procedures developed in this program will be standardized by ASTM and/or ISO.

Technical Highlights and Results

1. Summary

In this semiannual period, we:

- devised a simple procedure for testing the flexural strength of cylindrical parts. This is the segmented cylinder test. Zirconia plunger parts were tested and evaluated.
- refined the design of a new flexure fixture for cylindrical specimens.
- collected final data and completed the new fracture toughness standard reference material, SRM 2100.
- rewrote the ISO elevated temperature flexure strength standard.
- critically reviewed the new draft silicon nitride material specification standard created by the Rolling Element Bearing Group (REBG)
- participated in other ASTM and ISO standards activities.

Research investigations on the diametral compression test method are on hold pending further analysis of the fracture patterns in specimens previously tested.

We currently are working on the following formal draft standards (DIS = Draft International Standard):

1.	ISO DIS 14704	Advanced (Fine) Ceramics - Determination of Flexural Strength at Room Temperature (NIST-USA convenes)
2.	ISO DIS 14705	Fine Ceramics (Advanced Ceramics, Advanced Technical Ceramics) - Test Method for Hardness for Monolithic Ceramics at Room Temperature (Convened by Japan, NIST represents the USA)
3.	ISO draft	Advanced (Fine) Ceramics - Determination of Flexural Strength at Elevated Temperature (NIST-USA convenes)
4.	ISO DIS 15732	Fine Ceramics (Advanced Ceramics, Advanced Technical Ceramics) - Determination of Fracture Toughness at Ambient Temperature by Single Edge Precracked Beam (SEPB) Method (Convened by Japan, NIST coordinates with ASTM Task Group)
5.	ISO draft	Fine (Advanced) Ceramics - Determination of Fracture Toughness at Room Temperature by the Surface Crack in Flexure (SCF) Method (Proposed by USA-NIST)
6.	ASTM PS-070	Conversion to Full Consensus standard of "Standard Test Methods for Determination of Fracture Toughness of Advanced Ceramics

Earlier work in this project has contributed to **eleven** completed standards:

1.	ASTM C 1161-90	Standard Test Method for Flexural Strength of Advanced Ceramics at Ambient Temperature
2.	ASTM C 1198-91	Dynamic Young's Modulus, Shear Modulus, and Poisson's Ratio for Advanced Ceramics by Sonic Resonance
3.	ASTM C 1211-92	Standard Test Method for Flexural Strength of Advanced Ceramic at Elevated Temperature
4.	MIL HDBK 790	Fractography and Characterization of Fracture Origins in Advanced Structural Ceramics
5.	ASTM C 1239-94	Standard Practice for Reporting Strength Data and Estimating Weibull Distribution Parameters
6.	ASTM C 1322-96	Standard Practice for Fractography and Characterization of Fracture Origins in Advanced Ceramics
7.	ASTM C 1326-96	Standard Test Method for Knoop Indentation Hardness of Advanced Ceramics.
8.	ASTM C 1327-96	Standard Test Method for Vickers Indentation Hardness of Advanced Ceramics.
9.	ASTM PS 070-97	Standard Test Methods for the Determination of Fracture Toughness of Advanced Ceramics
10.	ASTM E-1875-98	Standard Test Method for Dynamic Young's Modulus, Shear Modulus, and Poisson's Ratio by Sonic Resonance
11.	ASTM E-1876-98	Standard Test Method for Dynamic Young's Modulus, Shear Modulus, and Poisson's Ratio by Impulse Excitation

The last two are recent additions and are standards created in ASTM Committee E-28, Mechanical Testing. Committee E-28 , in consultation with Committee C-28 Advanced Ceramics and NIST, copied two C-28 standards (C 1198 and C 1259) almost verbatim. It was felt that the C-28 standards were well written and generic and need not be confined to advanced ceramics, but are applicable to all elastic materials.

2. Fracture Toughness

2a. ASTM Standard - Refine PS 070

The ASTM standard is wending its way through the process of adoption as a full consensus standard. It was on the Fall 1998 ballot. One negative was received from Mr. F. Baratta on the issue of whether the tolerances for aligning the precrack in the SEPB test were adequate. At the January 1999 Committee meeting of C-28, the committee found the negative to be nonpersuasive on the grounds that such an error was tolerable and that tightening the tolerance for crack alignment (currently 0.5 mm) would be impractical. A note will be added to the full consensus standard to clarify this issue, subject to the approval of the ASTM editors. We note in passing that the results of a VAMAS round robin for the fracture toughness of a whisker-reinforced silicon nitride actually did show about a 3-5% error in SEPB fracture toughness results when tested on very short (16 mm) spans. The ASTM standard also received a substantive affirmative with comment ballot from Mr. S. Choi. One of the issues he raised pertained to an inconsistency in the specifications for fixture rolling pin diameter.

The ASTM standard now goes to a Society review and we are hopeful that it will be approved in early 1999. Over 110 revisions have been made to the Provisional Standard. This underscores the merit of a provisional standard in ASTM: a procedure can be put on the books and users can begin to apply it, while it is still being refined. We expect that a "revision to" the full consensus standard will be balloted in early 2000 to rectify the load pin discrepancy and any other loose ends that may remain.

2b. Standard Reference Material 2100 for Fracture Toughness

The Standard Reference material for fracture toughness was finished. As far as we know, this is the first reference material in the world for the property fracture toughness for any class material (metal, ceramic, polymer, composite).

Fifty single-edged precracked beam experiments were done to clear up some material nonuniformity issues. These experiments were successful and it is now clear that specimens from billets C, G, and D are completely satisfactory for the standard reference material. Remarkable consistency has been achieved with the SEPB, SCF, and CNB methods, which are the three in ASTM standard, PS 070-97. On any specific billet, the mean fracture toughness and the standard deviation by the three test methods converge to within one percent. A paper on the SRM was presented at the ACS meeting in Cocoa Beach in January, 1999.

SRM 2100 will be available for sale in May 1999 at a cost of $335 for a kit of 5 specimens with certified fracture toughness. 535 specimens will be used to prepare 107 kits are available for distribution in kits of 5 specimens each.

2c. Draft International Standard, ISO Technical Committee TC 206, Fine Ceramics
The draft fracture toughness by the SEPB method standard was prepared by Dr. T. Nose in Japan in October 1998. This document was reviewed and we requested changes in several critical tolerances to bring the ISO draft into closer alignment with the ASTM document. For example, we requested that the allowable precrack angle for three-point loading be reduced from 10 degrees to 5 degrees. We also requested that the allowable crack depth range be reduced from 0.3 to 0.6 alpha to 0.35 to 0.6 alpha. We were gratified that Dr. Nose implemented these and other changes.

3. Flexure Strength at Room Temperature - New Semiarticulating Fixture Design
No activity this period. All work is complete, but a report and engineering drawings must be prepared.

4. Diametral Compression
No activity this period. This work is on hold pending further intensive fractographic analysis to determine why our earlier test specimens did not fracture from volume flaws in the middle of the specimens. A German report from the Fraunhofer Institute in Freiburg must be translated and read as well since it has important new information about this test method. We remain optimistic that this method can be refined and made into a user friendly, standardized test.

5. Flexure Testing of Cylindrical Ceramic Specimens
Figure 1 shows the new fixture design developed as part of the NIST Machining of Ceramics Consortium. We realize there is interest within the DOE Heavy Duty Diesel community for such testing. Therefore we accelerated the development of these fixtures in this program. A paper is in preparation for the Journal of the American Ceramic Society which will feature the new fixtures. In response to a request from K. Breder at ORNL, a polished set of engineering drawings was prepared and sent to ORNL for review. HTML may make a set and compare results to those obtained with their in-house fixtures.

Figure 1 Flexure Fixture For Cylindrical Specimens with a Glass Specimen

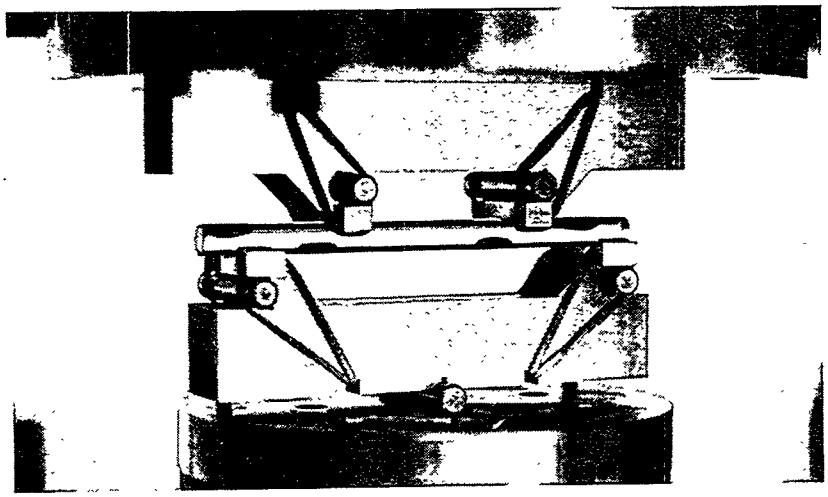

6. Flexure Testing of Segmented Cylindrical Ceramic Specimens

In the present period, we explored an approach intended for short stubby cylinders such as the 9.5 mm diameter x 47 mm long zirconia plungers manufactured by Coors for the Cummins Company. Short stubby cylinders may be difficult to test since fracture loads would be excessive and could cause damage to flexure fixtures.

A paper[1] by Ludwig Weiler of Asea Brown Boveri in 1987 showed that segmented, or cut, cylinders could be tested in flexure. Although Weiler applied the method to sections cut from thick-walled ceramic heart exchanger tubes, there was no reason the same approach could not be used on solid cylinders. Consequently, we cut six zirconia plungers in half as shown in Figure 2.

Figure 2 A full zirconia plunger and a segmented half cylinder.

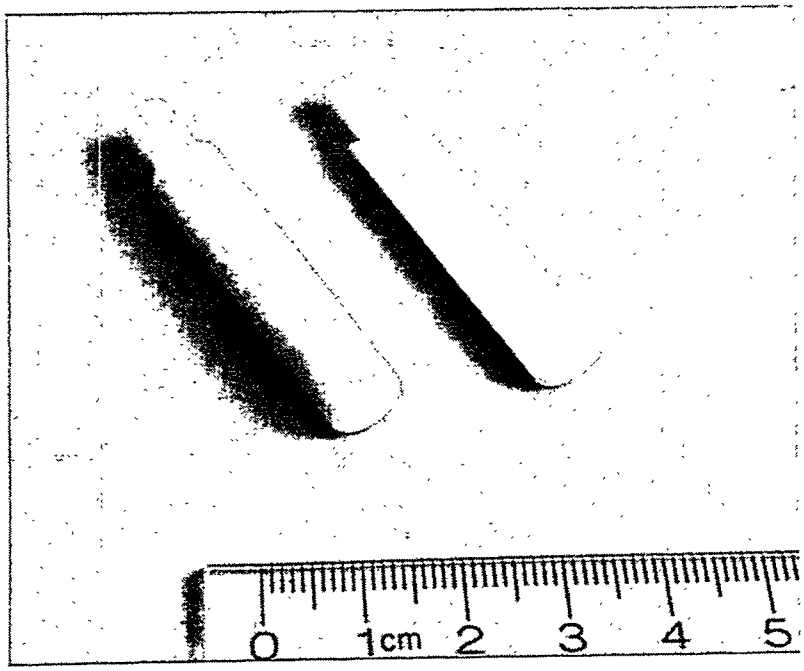

Figure 3 Schematic of the flexure fixture for segmented cylinders.

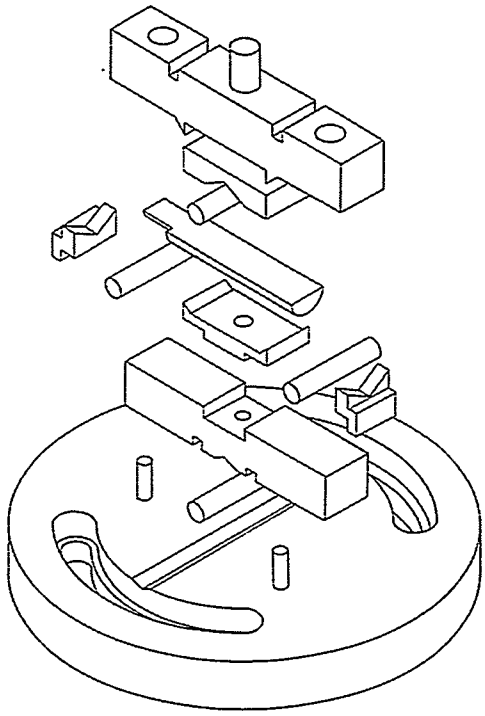

Figure 4 Photograph of the fixture with a specimen in place.

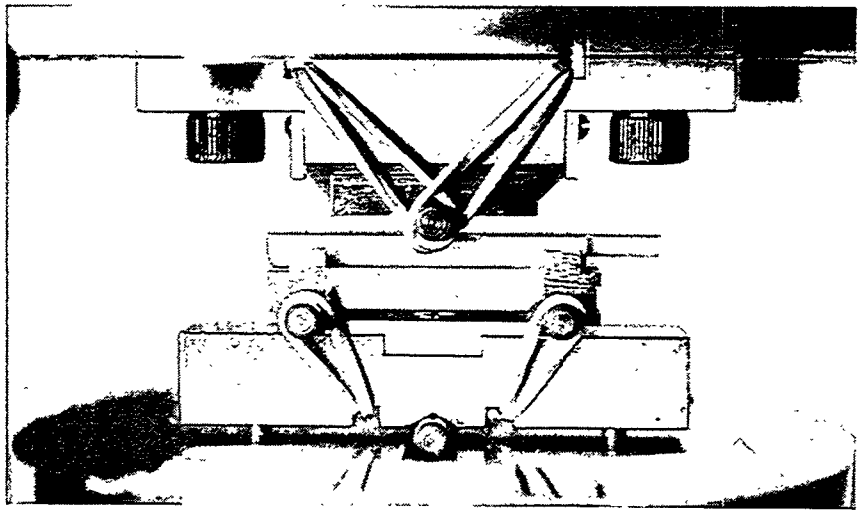

There also was a matter of how to apply the load to the specimens so that the load is evenly distributed. Further-more, the specimens must be free to expand without load point constraint that would cause friction, one of the more serious (5-15%) sources of error in flexure testing. To solve these problems, we adapted the flexure fixture "shoe concept" that we had developed at NIST for full-cylindrical specimens testing.

Figures 3 and 4 illustrate the modified flexure fixture in use at NIST with a segmented cylindrical specimen in place. Three point loading is used since the breaking load is much less than that for four-point loading. The outer span was 30 mm. The cut ceramic specimen surface is loaded in compression, whereas the as-processed plunger surface is loaded in tension. Six plungers, or more precisely, twelve halves were tested and they all broke cleanly in the vicinity of the middle roller. There was no evidence of contact roller cracking or loading problems of any sort. Testing was very fast and efficient. Specimen alignment was simple. If the segmented cylinder was a little twisted relative to the loading rollers, it rotated into perfect registry during preloading. The average strength was 545 MPa (79.1 ksi) and the standard deviation was 27.8 MPa (4.0 ksi). The Weibull plot is shown in Figure 5.

Figure 5 Strength distribution for twelve segmented cylinder specimens.

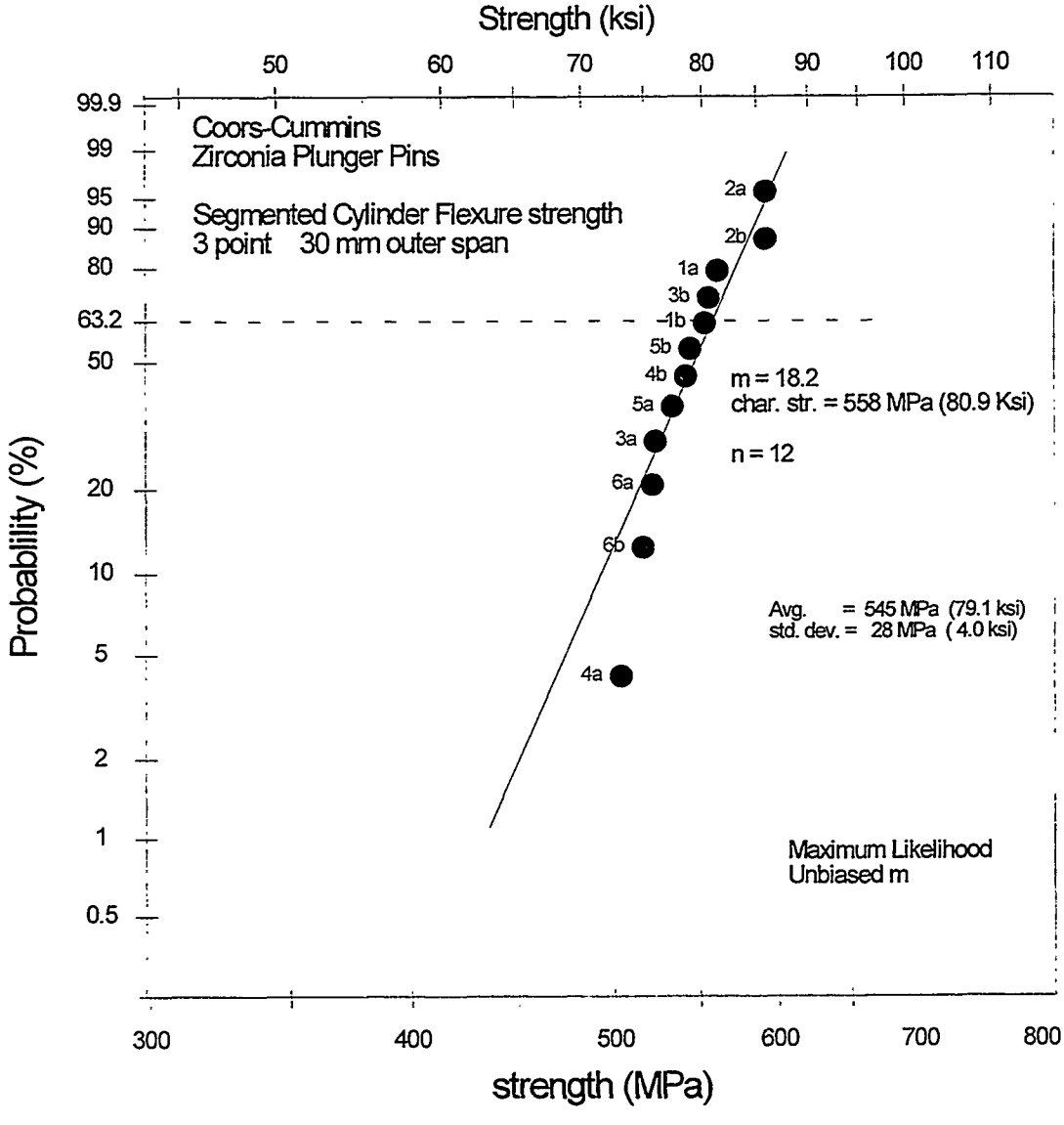

7. Rolling Element Bearing Group (REBG) Silicon Nitride Bearing Ball Specification

A draft material specification for silicon nitride is being developed by the REBG, an association of bearing manufacturers and users and the Department of Defense. The draft specification which is at an advanced stage, included a suite of materials requirements including density, color uniformity, surface finish, surface flaws, hardness, flexure strength, and fracture toughness. The specification was crafted by the REBG based upon prior internal company specifications in use at SKF and MRC. Participants in the project include Norton-Cerbec, Enceratec (Cummins-Toshiba), SKF, MRC, ESK, Hughes, and others. We are gratified that several ASTM C-28 standards (developed in this DOE program), (C 1161 flexure strength, C 1327, Vickers hardness, and C 1198, Elastic moduli by resonance are used by the specification. Unfortunately, a group of Japanese Industrial Standards and a few German DIN standards are also listed. This will cause some confusion. For example, the bearing grade, class I, II, or II depends in part upon the flexure strength level. A class I bearing material must have a 4-point strength of 700 MPa or greater. It is not specified whether this result may be obtained with the smaller 3 x 4 x 30+ mm JIS specimen or the larger 3 x 4 x 40+ mm ASTM "B" specimen, or from the ASTM mini "A" sized specimen for that matter. The specification's authors do not seem to be cognizant of the variation in ceramics strengths due to specimen size differences. This should be cleared up.

The material specification also includes a Weibull modulus requirement. A class I bearing material should have a Weibull modulus, M, of 10 or more. Nowhere is it stated how to obtain this value, however. Worse, the specification requires that only 20 specimens be tested. Using Weibull modulus in a specification is a "risky" proposition. Years of work in the DOE program by this investigator and many other DOE subcontractors (e.g. GE; Allied Signal, Ford, ORNL-HTML, etc,) have shown that estimates of Weibull modulus are "noisy" due to simple statistical sampling variability. For example, one investigator may obtain an M of 9 with his sample set of 20 specimens when the true M is 12. The low estimate is just a common outcome from using a limited sample size (n=20). The low M from the one data set would cause the material to be unfairly rejected. Different values may be obtained by different analysis techniques (linear regression with various probability estimators or maximum likelihood). We will recommend that the REBG cite and use the ASTM standard C 1239 for estimating M. This will resolve the analysis methodology issue, but it will not resolve the uncertainty or statistical sampling variability issue.

The draft specification has other weak elements and we will not dwell on them here. (The fracture toughness requirements are a case in point!) Suffice to say that the specification was crafted by well meaning individuals based upon procedures in use at several companies, but has some shortfalls that can be remedied by participation by standards experts. A 6 page critical review of the draft was sent to key individuals in the REBG. The next meeting of the REBG is in May 1999 in Jacksonville, FL and Mr. Quinn plans to attend.

8. Other Activities

8a. Fractographic Webb Site

NIST finished the installation of the new NIST web site for fractographic analysis of advanced ceramics. The web site, which is in essence a skeletal version of ASTM standard C 1322, is:

http://www.ceramics.nist.gov/webbook/fracture/fracture.htm

8b. A proof copy of the newly revised ASTM C 1211 Flexure Strength at Elevated Temperature document, incorporating revisions approved by a formal ASTM ballot in the fall of 1998, was reviewed.

8c. ISO Test Method Standards

Mr. Quinn represented the United States at the ISO TC 206, Fine Ceramics, meeting in September, 1998 in Kyongju, Korea for the following Working Groups:

WG 2	Room Temperature Flexure Strength, Overall Convener
WG 3	Hardness, USA representative
WG 6	Tension Strength, Monolithics, represented the USA on behalf of Mike Jenkins
WG 7	Fracture Toughness by SEPB, represented the USA on behalf of the ASTM Task Group
WG 8	Elevated Temperature Flexure Strength, Overall Convener
WG 9	Tensile Behavior, Composites, Led this WG on behalf of Mike Jenkins, the Overall Convener
WG 10	Elastic Modulus, Represented the USA on behalf of Steven Gonczy, the USA representative
WG 11	Weibull Analysis, Led this WG on behalf of Steven Duffy, the Overall Convener
NWI	Fracture Toughness by the SCF Method, Overall Convener

The last is a "New Work Item", which is the precursor stage to a Working Group. In each instance, wen reviewed the USA standards, coordinated with the USA representatives in ASTM Committee C-28, and represented the USA position at the meeting. Prior International Energy Agency round robin results were very helpful in supporting the USA position in WG 6, tension testing, and WG 8, elevated temperature flexure strength.

WG 2 Flexure Strength at Room Temperature
Following recommendations by Mr. Quinn, the ASTM Committee decided to vote "negative" on the current draft international standard, which was prepared by Mr. Quinn, the convener for this topic. It was agreed that the current draft did not adequately deal with the issue of test humidity and its effect on test results. This point had been raised by the Korean delegation in the last TC 206 Fine Ceramics meeting in September, 1998. The US delegation agreed that the draft needs improvement.

WG 3 Hardness
A draft prepared by the Japanese convener was found to be completely satisfactory to the USA. The draft is consistent with (and indeed, uses some figures from) ASTM standards C 1326 and C 1327 prepared by ASTM Committee C-28. The USA will vote affirmative with no comments on this Draft International Standard.

WG 7 Fracture Toughness by SEPB
The ASTM C-28 committee agreed to vote affirmative on this Japanese-convener's document, following revisions that we had requested in November 1998.

WG 8 Flexure Strength at Elevated Temperature
A draft of this test method was extensively revised and the draft was sent to the Japanese secretariat for distribution prior to the upcoming ISO TC 206 meeting in London in June. Despite strong Japanese pressure to eliminate as-fired specimens and fully-articulating fixtures as options in the draft, these elements have been retained. They are integral to the USA and European testing methods. We recognize that there have to be some limits for the bow and twist for as-fired specimens, however. We conducted new analyses to check the reasonable ranges for these distortions in as-fired specimens.

The original error analyses of Baratta (U.S. Army Technical Report TR 82-20) and it's later more refined version by Baratta, Quinn, and Matthews, (U.S. Army Technical Report TR 87-35) were revisited and expanded to cover the issue of testing warped, as-fired specimens. Details on this are in the February-March 1999 bimonthly progress report.

In response to requests from several ISO members, a new section on optical pyrometry as a means to measure temperature was included in the ISO draft. Optical pyrometry is useful at very elevated temperatures (e.g. > 1600°C) but has not been included in the ASTM standard C 1211 or any national standard. Several ASTM standards on Optical Pyrometers are available, but close reading of these showed there are many nuances and possible errors associated with their use. These include emissivity corrections, window absorption, misalignment of the apertures, and internal reflections from the furnace.

An appendix on corrections to stress for specimen chamfers has been included. This was welcomed by some member nations since they contended the ASTM sizes were too small and too strict. (The ASTM sizes and tolerances were chosen to keep the error less than 1%.) This correction appendix may be added to the ASTM standards C 1161 and C 1211 in the future if C-28 wishes.

e. Fracture toughness by SCF method

We learned that the first draft of this document, prepared by Mr. Quinn in February 1998 with his proposal for a new work item, will be sent out for a formal distribution and review by the ISO Technical Committee. This is somewhat unfortunate, since we were not informed of the deadline and thus had no opportunity to prepare a revised draft.

Status of Milestones

412139	Conduct flexure strength tests for alumina AD-99 cylindrical rods	Completed September 1998
412140	Conduct flexure strength tests for Mg zirconia half cylinders	Completed November 1998
412124	Prepare comprehensive paper on hardness testing of ceramics Delay until SRM 2831, Vickers hardness of Ceramics is complete.	Reschedule
412129	Write comprehensive report on fracture evaluation by SCF method	Delayed

The following 4 milestones should be deferred or canceled due to unexpected test methodology problems.

412132	Commence diametral compression round robin	Cancel
412133	Prepare draft diametral compression standard for ASTM	Cancel
412134	Prepare review paper on diametral compression method	Cancel
412138	Conduct new Phase II diametral compression strength tests	Defer to 2000

Problems encountered

We no longer have a visiting scientist or postdoc to assist on this project, so experimental testing will be slowed.

A new phase of diametral compression testing and analysis is needed to follow on the unsatisfactory outcomes of our work in the fall of 1997 and winter of 1997/1998.

Publications/Presentations

1. J. Salem, L. Ghosn, M. Jenkins, and G. D. Quinn, "Stress Intensity Factor Coefficients for Chevron-Notched Flexure Specimens and A Comparison of Fracture Toughness Methods," presented at Cocoa Beach ACS meeting, January 1999, to be publ. Ceram. Eng. and Sci. Proc., 1999.

2. G. D Quinn, K. Xu, and R. Gettings, Standard Reference Material 2100: Fracture Toughness of Ceramics," presented at Cocoa Beach ACS meeting, January 1999, to be publ. Ceram. Eng. and Sci. Proc. 1999
3. G. D. Quinn, J. A. Salem, I. Bar-On, and M. G. Jenkins, "The New ASTM Fracture Toughness of Ceramics Standard: PS 070-97," Ceram. Eng. and Sci. Proc., Vol. 19 [3] (1998) pp. 565-579.

Communications/Visits

1. Several calls, emails and faxes were exchanged in the ASTM task group on the topic of the ASTM fracture toughness standard and also the ISO draft SEPB standard test method.
2. Several NC 132 SEPB specimens were tested and results compared with experiments done by Jon Salem at NASA-Lewis who had tried chevron notch experiments in air, water, and oil. The specimens were all from candidate billet H of the reference material. This billet had shown a tendency to be sensitive to slow crack growth even at room temperature in lab ambient conditions.
3. The segmented cylinder data was discussed with T. Yonushonis at Cummins.
4. The design of the cylindrical flexure specimen test fixture was sent to K. Breder at ORNL.
5. Norton-Cerbec, SKF, Enceratec, and U.S. Army engineers were contacted regarding the REBG material specification.
6. We received a number of specimens of several materials from Jon Salem of NASA-Lewis who wished for us to test them for fracture toughness by the SCF method. This would enable us to complete the "triad" of test methods (SCF, CNB, SEPB) in the ASTM standard. Unfortunately, we were unable to start this SCF work before the Cocoa Beach meeting in January.
7. Information regarding biaxial strength testing (ring on ring, etc) was sent to Jon Salem at NASA-Lewis and to Dale McCullum, recently retired from Univ. Dayton Research Institute, so that they could begin the process of formulating an ASTM standard.

References

[1] Weiler, "Cylinder-Segment Bend Test, A New Strength Measuring Technique for Ceramic Tubes and Cylinders," pp 621 - 625 in Science of Ceramics 14, Ed. D. Taylor, Institute of Ceramics, Stoke on Trent, 1989.

ORNL/TM-199/95

INTERNAL DISTRIBUTION

L. F. Allard, Jr.
P. F. Becher
T. M. Besmann
P. J. Blau
R. A. Bradley
K. Breder
C. R. Brinkman
T. D. Burchell
A. Choudhury
D. D. Conger
S. A. David
M. K. Ferber
R. L. Graves
H. W. Hayden, Jr.
C. R. Hubbard
M. A. Janney
D. R. Johnson (5)
R. R. Judkins
M. A. Karnitz
R. J. Lauf
K. C. Liu
W. D. Manly
S. B. McSpadden
T. A. Nolan
A. E. Pasto
M. H. Rawlins
A. C. Schaffhauser
D. P. Stinton
T. N. Tiegs
S. G. Winslow
R. E. Ziegler
Laboratory Records - RC

EXTERNAL DISTRIBUTION

Jeffrey Abboud
U.S. Advanced Ceramics Assoc.
1600 Wilson Blvd., Suite 1008
Arlington VA 22209

B. P. Bandyopadhyay
University of North Dakota
Box 8359 University Station
Grand Forks ND 58202-8359

Donald F. Baxter, Jr.
Advanced Materials & Processes
ASM International
9639 Kinsman Road
Materials Park OH 44073-0002

M. Brad Beardsley
Caterpillar Inc.
Technical Center Bldg. E
P.O. Box 1875
Peoria IL 61656-1875

Ramakrishna T. Bhatt
NASA Lewis Research Center
MS-106-1
21000 Brookpark Road
Cleveland, OH 44135

Bruce Boardman
Deere & Company, Technical Ctr.
3300 River Drive
Moline IL 61265-1792

Michael C. Brands
Cummins Engine Company, Inc.
P.O. Box 3005, Mail Code 50179
Columbus IN 47201

Donald J. Bray
Advanced Refractory Technologies
699 Hertel Avenue
Buffalo NY 14207

Walter Bryzik
U.S. Army Tank Automotive
Command
R&D Center, Propulsion Systems
Warren MI 48397-5000

David Carruthers
Kyocera Industrial Ceramics
5713 East Fourth Plain
Vancouver WA 98661

Ronald H. Chand
Chand Kare Technical Ceramics
2 Coppage Drive
Worcester MA 01603-1252

William J. Chmura
Torrington Company
59 Field Street, P.O. Box 1008
Torrington CT 06790-1008

William S. Coblenz
Defense Adv. Research Projects Agency
3701 N. Fairfax Drive
Arlington VA 22203-1714

Gloria M. Collins
ASTM
100 Barr Harbor Drive
West Conshohocken PA 19428-2959

Shawn Cooper
FEV Engine Technology
4554 Glenmeade Lane
Auburn Hills MI 48326-1766

Douglas Corey
AlliedSignal, Inc.
2525 West 190th Street, MS:T52
Torrance CA 90504-6099

Keith P. Costello
Chand/Kare Technical Ceramics
2 Coppage Drive
Worcester MA 01603-1252

Gary M. Crosbie
Ford Motor Company
P.O. Box 2053, 20000 Rotunda Drive
MD-3182, SRL Building
Dearborn MI 48121-2053

Pamela Cunningham
WETO Technical Library
MSE, Inc.
Industrial Park, P. O. Box 4078
Butte MT 59702

Sidney Diamond
U.S. Department of Energy
Office of Transportation Technologies
EE-33, Forrestal Building
Washington DC 28505

Ernest J. Duwell
3M Abrasive Systems Division
3M Center, Bldg. 251-01-34
St. Paul MN 55144

Michael Easley
AlliedSignal Engines
P. O. Box 52181
MS 551-11
Phoenix AZ 85072-2181

J. J. Eberhardt
U.S. Department of Energy
Office of Transportation Technologies
EE-33, Forrestal Building
Washington DC 20585

Jim Edler
Eaton Corporation
26201 Northwestern Highway
P.O. Box 766
Southfield MI 48037

William A. Ellingson
Argonne National Laboratory
Energy Technology Division, Bldg. 212
9700 S. Cass Avenue
Argonne IL 60439-3848

John W. Fairbanks
U.S. Department of Energy
Office of Transportation Technologies
EE-33, Forrestal Building
Washington DC 20585

Ho Fang
Applied Materials
2695 Augustine Drive, MS-0962
Santa Clara CA 95054

Dan Foley
AlliedSignal Ceramic Components
MS:1/5-1, 26000
2525 West 190th Street
Torrance CA 90504

Douglas Freitag
DuPont Lanxide Composites
21150 New Hampshire Avenue
Brookeville MD 20833

Richard Gates
NIST
Bldg. 223, Rm. A-256
Rt. 270 & Quince Orchard Road
Gaithersburg MD 20899

Ludwig J. Gauckler
ETH Zurich
Nonmetallic Materials
Sonneggstr. 5
CH-8092 Zurich, SWITZERLAND

Allan E. Goldman
U.S. Graphite, Inc.
907 W. Outer Drive
Oak Ridge TN 37830

Robert J. Gottschall
U.S. Department of Energy
Metal & Ceramic Sciences, ER-131
19901 Germantown Road
Germantown MD 20874-1290

Thomas J. Gross
U.S. Department of Energy
Office of Transportation Technologies
EE-30, Forrestal Building
Washington DC 20585

Changsheng Guo
Chand Kare Technical Ceramics
2 Coppage Drive
Worcester MA 01603

Nabil S. Hakim
Detroit Diesel Corporation
13400 Outer Drive West, A08
Detroit MI 48239-4001

Alan M. Hart
Dow Chemical Company
1776 Building
Midland MI 48674

Michael H. Haselkorn
Caterpillar Inc.
Technical Center, Building E
P.O. Box 1875
Peoria IL 61656-1875

Deborah A. Haught
U.S. Department of Energy
Ofc. of Industrial Crosscut Technologies
EE-23, Forrestal Bldg.
Washington DC 20585

Daniel Hauser
Edison Welding Institute
Microjoinint & Plastics Tech. Team
1250 Arthur E. Adams Drive
Columbus OH 43221-3585

John Haygarth
Wah Chang
P.O. Box 460
Albany OR 97321-0460

Gene Huber
Precision Ferrites & Ceramics
5432 Production Drive
Huntington Beach CA 92649-1525

Thomas A. Johnson
Lanxide Corporation
1300 Marrows Road
P.O. Box 6077
Newark DE 19714-6077

Adam Jostsons
ANSTO
PMB1
Menai, NSW, Australia 2234

Yury Kalish
Detroit Diesel Corporation
Mechanical Systems
13400 Outer Drive West
Detroit MI 48239-4001

Roy Kamo
Adiabatics, Inc.
3385 Commerce Park Drive
Columbus IN 47201

W. C. King
Mack Truck, Z-41
1999 Pennsylvania Avenue
Hagerstown MD 21740

Tony Kirn
Caterpillar Inc.
Defense Products Dept., JB7
Peoria IL 61629

Joseph A. Kovach
Parker Hannifin Corporation
6035 Parkland Boulevard
Cleveland OH 44124-4141

Edwin H. Kraft
Kyocera Industrial Ceramics
5713 E. Fourth Plain Boulevard
Vancouver WA 98661

Arthur Kranish
Trends Publishing Inc.
1079 National Press Building
Washington DC 20045

Oh-Hun Kwon
Norton Company
Saint Gobain Industrial Ceramics
1 Goddard Road
Northboro MA 01532-1545

S. K. Lau
B. F. Goodrich Aerospace R&D
9921 Brecksville Road
Brecksville OH 44141

Elaine Lentini
Saint-Gobain Industrial Ceramics
Goddard Road
Northboro MA 01532

Stan Levine
NASA Lewis Research Center
21000 Brookpark Road, MS:106/5
Cleveland OH 44135

Robert H. Licht
Norton Company
Saint Gobain Industrial Ceramics
1 Goddard Road
Northboro MA 01532-1545

E. Lilley
Norton Company
Saint Gobain Industrial Ceramics
1 Goddard Road
Northboro MA 01532-1545

B. J. McEntire
Applied Materials Corporation
3050 Bowers Avenue
Santa Clara, CA 95054

James McLaughlin
Sundstrand Power Systems
4400 Ruffin Road
P.O. Box 85757
San Diego CA 92186-5757

Biljana Mikijelj
Ceradyne, Inc.
3169 Red Hill Avenue
Costa Mesa CA 92626

Carl E. Miller
Delphi Energy & Engine Mgmt. Systems
4800 S. Saginaw Street, MC 485-301-150
P. O. Box 1360
Flint MI 48501-1360

Curtis V. Nakaishi
U.S. Department of Energy
Federal Energy Tech. Center
3610 Collins Ferry Rd.
P.O. Box 880
Morgantown WV 26507-0880

Malcolm Naylor
Cummins Engine Company, Inc.
P.O. Box 3005, Mail Code 50183
Columbus IN 47202-3005

Dale E. Niesz
Ceramic & Materials Engineering
607 Taylor Road, Rm. 204
Piscataway, NJ 08854-8065

Thomas J. Paglia
Coors/ACI
3315 Boone Road
Benton AR 72015

Richard Palicka
CERCOM, Inc.
1960 Watson Way
Vista CA 92083

Vijay M. Parthasarathy
Solar Turbines
2200 Pacific Highway, M.Z. R-1
San Diego CA 92186

Magan Patel
Cummins Engine Company, Inc.
Mail Code 50183
Box 3005
Columbus IN 47202-3005

James W. Patten
Cummins Engine Company, Inc.
P.O. Box 3005, Mail Code 50183
Columbus IN 47202-3005

Stephen C. Pred
Pred Materials International, Inc.
60 East 42nd Street, Suite 1456
New York NY 10165

Vimal K. Pujari
Norton Company
Saint Gobain Industrial Ceramics
1 Goddard Road
Northboro MA 01532-1545

Fred Quan
Corning Inc.
Sullivan Park, FR-2-8
Corning NY 14831

George Quinn
NIST
I-270 & Clopper Road
Ceramics Division, Bldg. 223
Gaithersburg MD 20899

Harold Rechter
Chicago Fire Brick Company
7531 S. Ashland Avenue
Chicago IL 60620-4246

Jack A. Rubin
CERCOM, Inc.
1960 Watson Way
Vista CA 92083

Robert J. Russell
Riverdale Consulting, Inc.
24 Micah Hamlin Road
Centerville MA 02632-2107

J. Sankar
North Carolina A&T State Univ.
Dept. of Mechanical Engineering
Greensboro NC 27406

Maxine L. Savitz
AlliedSignal, Inc.
Ceramic Components
2525 West 190th Street
P.O. Box 2960, MS:1/5-1, 26000
Torrance CA 90509-2960

Jim Schienle
AlliedSignal Aerospace
1130 West Warner Road
M/S 1231-K
Tempe AZ 85284

Gary Schnittgrund
Transfer Technology
16401 Knollwood Drive
Granada Hills CA 91344

Robert S. Shane
Shane Associates
1904 NW 22nd Street
Stuart FL 34994-9270

Subu Shanmugham
MicroCoating Technologies
3901 Green Industrial Way
Chamblee GA 30341-1913

Charles Spuckler
NASA Lewis Research Center
21000 Brookpark Road, MS: 5-11
Cleveland OH 44135-3127

Gordon L. Starr
Cummins Engine Company, Inc.
P.O. Box 3005, Mail Code:50182
Columbus IN 47202-3005

Marian Swirsky
Cambridge Scientific Abstract
Commerce Park, Bldg. 4, Suite 804
23200 Chagrin Blvd.
Beachwood OH 44122

Victor J. Tennery
113 Newell Lane
Oak Ridge TN 37830

Malcolm Thomas
Allison Engine Company
P. O. Box 420 (W06)
Indianapolis IN 46206

Marc Tricard
Norton Company
Superabrasives Division
1 New Bond Street, MS-412-301
P. O. Box 15008
Worcester MA 01615-0008

Marcel H. Van De Voorde
Commission of the European Union
Eeuwigelaan 33
1861 CL Bergen
THE NETHERLANDS

V. Venkateswaran
Materials Solutions International, Inc.
P.O. Box 663
Grand Island, NY 14072-0663

Robert M. Washburn
ASMT
11203 Colima Road
Whittier CA 90604

R. W. Weeks
Argonne National Laboratory
Bldg. 362, E313
9700 S. Cass Avenue
Argonne IL 60439

Sheldon M. Wiederhorn
NIST
Building 223, Room B309
Gaithersburg MD 20899

Matthew F. Winkler
Seaworthy Systems, Inc.
P.O. Box 965
Essex CT 06426

Thomas J. Wissing
Eaton Corporation
26201 Northwestern Highway
P.O. Box 766
Southfield MI 48037

James C. Withers
MER Corporation
7960 S. Kolb Road
Tucson AZ 85706

Dale E. Wittmer
Southern Illinois University
Mechanical Engineering Dept.
Carbondale IL 62901

Egon E. Wolff
Caterpillar Inc.
Technical Center
P.O. Box 1875
Peoria IL 61656-1875

Roy Yamamoto
Ethyl Petroleum Additives, Inc.
500 Spring Street
P. O. Box 2158
Richmond VA 23218-2158

Thomas M. Yonushonis
Cummins Engine Company, Inc.
1900 McKinley Avenue
P.O. Box 3005, Mail Code 50183
Columbus IN 47202-3005

Jong Yung
Sundstrand Aerospace
Dept. 789-6
4747 Harrison Avenue
Rockford IL 61125

A. L. Zadoks
Caterpillar Inc.
Technical Center, Building L
P.O. Box 1875
Peoria IL 61656-1875

Zhenqi Zhu
Stevens Institute of Technology
Department of Mechanical Engineering
Castle Point on Hudson
Hoboken NJ 07030

Department of Energy
Oak Ridge Operations Office
Assistant Manager for Energy
Research and Development
P. O. Box 2001
Oak Ridge TN 37831-8600

For distribution by microfiche
as shown in DOE/OSTI-4500,
Distribution Category UC-332
(Ceramics/Advanced Materials).